INTERACTION NOTES

Note 234

July 1974

SPACE TIME INTEGRAL EQUATION APPROACH FOR TARGETS WITH EDGES

C. L. Bennett
K. S. Menger
R. Hieronymus
J. DeLorenzo
D. Anderson

Sperry Rand Research Center

ABSTRACT

The space-time integral equation approach is extended to the solution of the large body problem for bodies with edges. An improved technique is developed for computing the smoothed impulse response of targets with edges which allows a variable patch size and provides greater economy and efficiency of solution than previously possible. The impulse response augmentation technique is then used to produce the total impulse response and the frequency response over the entire spectrum. Results are obtained for a sphere-cap flat-end cylinder and a right-circular cylinder.

The space-time integral equation approach is extended to the problem of scattering from open, thin surfaces. The E-field boundary condition is used to develop the space-time integral equation, which in turn is solved numerically by marching on in time. Smoothed impulse responses are obtained using this technique for a square plate, a circular disc, and a parabolic cylinder section. These computed results compare well with measurements taken on the time domain scattering range. Smoothed impulse response measurements are also included for a selection of other open, thin surface target geometries.

A solution technique is developed for the inverse scattering problem using a space-time integral equation approach. This technique, which uses an iterative solution scheme, is demonstrated on the sphere, sphere-capped cylinder, and flat-end sphere-cap cylinder. The solution converges closely to the actual target geometry in these cases.

TABLE OF CONTENTS

TABLE OF CONTENTS (CONT.)

LIST OF ILLUSTRATIONS

LIST OF ILLUSTRATIONS (CONT.)

LIST OF ILLUSTRATIONS (CONT.)

LIST OF ILLUSTRATIONS (CONT.)

SECTION 1
INTRODUCTION

This document is submitted as the final report in response to the requirements set forth in Contract No. F30602-73-C-0124 between the Sperry Research Center, Sudbury, Massachusetts, and the Air Force Systems Command, Rome Air Development Center, Griffiss Air Force Base, New York. The primary objective of this program, performed during the period 17 January 1973 through 16 January 1974, was to extend the technique for computing the impulse response of smooth convex bodies to bodies which have edges and to open, thin surfaces.

In Sec. 2 the case of scattering from targets with edges is considered. Improved numerical solution techniques are developed, described and applied for computation of the smoothed impulse response for these targets using the space-time integral equation. The resulting numerical techniques provide more accurate, more efficient solutions for targets with edges. Smoothed impulse response computations are presented for the case of the flat-end sphere-cap cylinder and the case of the right-circular cylinder for numerous aspect angles and for both TE and TM polarizations. The impulse response augmentation technique was applied to these two target geometries for axial incidence. It was found that only slight modifications were required in the procedures that had been developed for smooth convex targets in order to handle the case of targets with edges. Both the total impulse response and the frequency response over the entire spectrum were computed for the flat-end sphere-cap cylinder and the right-circular cylinder for axial incidence. The results are in good agreement with what had been expected.

In Sec. 3 the results of additional time domain scattering range measurements are presented. Measurements were taken to obtain the smoothed impulse response of seven open, thin surfaces which include a square plate, a rectangular plate, a circular plate, a corner reflector, a circular cylinder section, a parabolic cylinder section, and a parabolic dish. An additional processing step has been applied to the measured results presented in this report in order to further reduce their noise content and to also facilitate comparison with smoothed impulse response computations.

Section 4 presents a detailed development of the numerical solution of the space-time integrodifferential equation for the case of open, thin surfaces. The basic integrodifferential equation is of the $\vec{E}$-field type, and its form provides some insight into the scattering mechanism itself. Solution procedures are presented for flat rectangular plates, flat circular plates, and convex rectangular plates. Smoothed impulse response computations are presented for a flat square plate, a flat circular plate, and a parabolic cylinder section. The results are compared with direct time domain measurements and found to be in good agreement.

The inverse scattering problem is addressed in Sec. 5 from a direct time domain viewpoint. A space-time integral equation is developed which in principle yields the solution to the inverse scattering problem. An iterative numerical technique for the solution of this inversion equation is developed, described, and applied to four targets. The sphere, sphere-capped cylinder, sphere-cap flat-end cylinder, and flat-end sphere-cap cylinder target geometries are used to test the technique. Conclusions are presented in Sec. 6.

SECTION 2

EXTENSION OF IMPULSE RESPONSE AUGMENTATION TECHNIQUE TO BODIES WITH EDGES

(C. L. Bennett and D. Peterson)

2.1 SPACE-TIME INTEGRAL EQUATION FOR BODIES WITH EDGES

The space-time integral equation for bodies with edges is the same as that used for smooth convex bodies without edges. However, the numerical treatment is modified to accommodate a more accurate and efficient solution procedure. Section 2.1.1 reviews the space-time integral equation approach and the numerical implementation for smooth convex bodies without edges. Section 2.1.2 describes the numerical solution procedure that has been developed during this contract for bodies with edges.

2.1.1 Review of Space-Time Integral Equation Approach

The space-time integral equation approach to the electromagnetic scattering problem was first developed in 1968.[1] This approach to the solution of transient electromagnetic scattering and radiation problems consists of formulating a time domain integral equation for the surface currents on the scatterer in such a way that the integral equation can be reduced to a recurrence relation in time. This equation is then solved numerically for the surface currents, which in turn can be used to compute the field at any point in space, in particular the far field.

Reviewing this technique, the general scattering problem is shown in Fig. 1. In this problem there is a magnetic field $\vec{H}^i$ incident on a conducting body whose surface is S. This incident field sets up currents on the surface $\vec{J}$ such that the $\vec{H}$-field boundary condition is satisfied. These currents, in turn, produce the scattered field $\vec{H}^s$. Once the surface currents have been determined, the field at any point in space may be computed (in particular the far field) and the problem is solved. The space-time integral equation used here for these surface currents[1] is derived by applying the $\vec{H}$-field boundary condition, and is thus sometimes referred to as an $\vec{H}$-field integral equation. $\vec{H}$-field integral equations are also sometimes referred to as Maue integral equations in recognition of A. W. Maue, who derived the first $\vec{H}$-field integral equation in the frequency domain.[2]

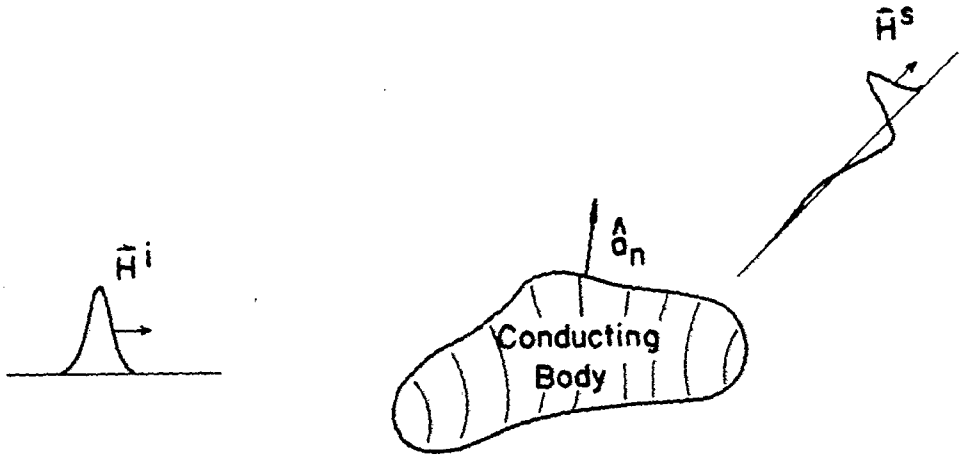

FIG. 1 General scattering problem.

The derivation of the space-time integral equation which is used here appears elsewhere.[1,3,4] This equation gives the currents on the surface $\vec{J}$ as a function of the incident field $\vec{H}^i$ and the surface currents at other points in space earlier in time:

$$\vec{J}(\vec{r}, t) = 2\hat{a}_n \times \vec{H}^i(\vec{r}, t) + \frac{1}{2\pi} \int_S \hat{a}_n \times \left\{ \left[\frac{1}{R^2} + \frac{1}{R} \frac{\partial}{\partial \tau} \right] \vec{J}(\vec{r}', \tau) \times \hat{a}_R \right\} dS' \qquad (1)$$

$$\tau = t - R$$

where

$\vec{r}$ = position vector to the observation point

$\vec{r}'$ = position vector to the integration point

$R = |\vec{r} - \vec{r}'|$

$\hat{a}_R = \dfrac{\vec{r} - \vec{r}'}{R}$

t = time in light meters

$\hat{a}_n$ = unit normal to surface at $\vec{r}$.

In many applications, the quantity of interest is the far-scattered field. The expression for the far-scattered magnetic field $\vec{H}^s$ is given by

$$r_o \vec{H}^s(\vec{r}, t) = \frac{1}{4\pi} \int_S \left\{ \frac{\partial \vec{J}(\vec{r}', \tau)}{\partial \tau} \right\} \times \hat{a}_r \, dS' \qquad (2)$$

$$\tau = t - R$$

where

r_o = the distance of the far-field observer from the target

$\hat{a}_r$ = the unit vector that points from the target to the far-field observer.

For numerical solution of Eq. (1), the target surface is divided up into curvilinear square patches and the current is computed at the center of each of the patches by marching on in time. The solution is carried out on the Cartesian components of the currents by using a numerical representation of Eq. (1). The integration over space and the differentiation over time are both carried out numerically.

For an explicit numerical solution which requires no matrix inversion, the scattering surface is divided into curvilinear patches of approximately equal area, with the space sample point at the center of each patch. The spacing of these sample points (and thus, the size of the patches) on the surface is chosen small enough to give both a good representation of the scatterer and also a good representation of the currents that exist on the scatterer. Next, the time increment Δt between the points in time at which the current is computed must be less than the time it takes a wave to travel between the closest space points. This condition is necessary for stability in an explicit solution procedure and also insures that the numerical procedure can be carried out by simply marching on in time without resorting to matrix inversion. The numerical solution may be represented with

$$\vec{J}(t) = \vec{J}_{po}(t) + \frac{1}{2\pi}\left[\sum_{\ell} \overrightarrow{FEQ}_{\ell}\, W_{\ell}\, \Delta S_{\ell}\right] \tag{3}$$

where

$$\vec{J}(t) = \begin{bmatrix} \vec{J}_1(t) \\ \vec{J}_2(t) \\ \vdots \\ \vec{J}_N(t) \end{bmatrix}$$

$$\vec{J}_{po}(t) = \begin{bmatrix} \left(2\hat{a}_n \times \vec{H}^i(t)\right)_1 \\ \left(2\hat{a}_n \times \vec{H}^i(t)\right)_2 \\ \vdots \\ \left(2\hat{a}_n \times \vec{H}^i(t)\right)_N \end{bmatrix}$$

$$\left[\sum \overrightarrow{FEQ}_\ell \; W_\ell \; \Delta S_\ell\right] = \begin{bmatrix} \left(\sum_\ell \overrightarrow{FEQ}_\ell \; W_\ell \; \Delta S_\ell\right)_1 \\ \left(\sum_\ell \overrightarrow{FEQ}_\ell \; W_\ell \; \Delta S_\ell\right)_2 \\ \vdots \\ \left(\sum_\ell \overrightarrow{FEQ}_\ell \; W_\ell \; \Delta S_\ell\right)_N \end{bmatrix}$$

$$\overrightarrow{FEQ}_\ell = \left(\frac{1}{R} + \frac{\partial}{\partial \tau}\right) \vec{J}_\ell(\tau)$$

$\tau < t - \Delta t$

W_ℓ = the appropriate weighting vector

ΔS_ℓ = the area of patch ℓ

N = the total number of patches.

Since $\tau < t - \Delta t$, then the right-hand side of Eq. (3) is completely known if the solution is started initially and then marched on in time. Thus, Eq. (3) represents the recurrence relation that gives the numerical solution of Eq. (1). However, for this solution to be obtained, the minimum spacing between space sample points must be greater than the time increment. This implies that for efficient operation, the space sample points should be approximately equally spaced. This condition is easily satisfied for smooth convex targets without edges. But for targets with edges, satisfying this condition would require larger patch size in the vicinity of the edge, which is inconsistent with the requirement that the current be adequately sampled near the edge. What is really needed is a technique which allows smaller patch size in the edge region and at the same time permits a time increment determined by the typical patch spacing. The next section presents a technique for accomplishing this goal.

2.1.2 Numerical Solution Technique for Bodies with Edges

This section presents a numerical technique which allows variable patch size on the target and does not sacrifice efficiency, accuracy, or stability in its implementation. If the spacing between patches becomes less than the time increment Δt , then the numerical solution of Eq. (1) may be written as

$$\vec{J}(t) = \vec{J}_{po}(t) + \frac{1}{2\pi}\left[\sum_{\ell} \overrightarrow{FEQ}_{\ell}\, W_{\ell}\, \Delta S_{\ell}\right] + \frac{1}{2\pi}\left[\sum F_{\ell}\, W_{\ell}\, \Delta S_{\ell}\right] \vec{J}(t) \quad (4)$$

where

F_{ℓ} = the portion of the numerical representation of $\left(\frac{1}{R} + \frac{\partial}{\partial \tau}\right)$ that operates on $\vec{J}(t)$.

Equation (4) may be written in the form

$$\vec{J}(t) = \vec{G}(t) + f\, \vec{J}(t) \quad (5)$$

where

$$\vec{G}(t) = \vec{J}_{po}(t) + \frac{1}{2\pi}\left[\sum_{\ell} FEQ_{\ell}\, W_{\ell}\, \Delta S_{\ell}\right]$$

$$f = \frac{1}{2\pi}\left[\sum F_{\ell}\, W_{\ell}\, \Delta S_{\ell}\right] \quad .$$

Of course Eq. (5) reduces to the earlier expression given in Eq. (3) if f is zero. The solution of this problem is termed explicit if f is zero and implicit if f is nonzero. The solution to the explicit problem is a recurrence relation in time and is obtained by a simple time stepping procedure. The solution to the implicit problem is also a recurrence relation in time, but in addition requires a solution of simultaneous equations at each time step.

The value of f is a function of the numerical representation used for interpolation to obtain $\vec{J}(\tau)$ and $\partial\vec{J}(\tau)/\partial\tau$ together with the relative value of the minimum space distance and the time increment Δt . In the past the numerical solution has been explicit, which for stability requires that Δt must be less than the minimum space distance. However, for bodies with edges it is desirable to use relatively small patches in the vicinity of the edge where the surface currents interact most strongly and have potential large amplitudes; over the remainder of the body the standard patch size is used. With this geometry, efficient solution of the problem demands that the time increment be larger than the minimum spacing of surface sample points. This requires an implicit solution of Eq. (5) for stability, since f is nonzero. The brute force approach for solving Eq. (5) is by means of matrix inversion and is given by

$$\vec{J}(t) = (1 - f)^{-1}\, \vec{G}(t) \quad . \tag{6}$$

However, this would have to be performed at every time point and would require a large block of computer memory for its implementation. For these reasons the matrix inversion approach is impractical for the solution of Eq. (5).

The approach chosen for the solution of Eq. (5) is that of iteration. As a first estimate the current is taken to be

$$\vec{J}^{1} = \vec{G} \quad . \tag{7}$$

It is interesting to note that this gives the contribution to $\vec{J}$ due to the incident field and the currents on all other patches whose spacing is greater than Δt , and thus this first estimate gives a very good approximation to the exact result. Next, Eq. (5) is used as a basis of the iteration formula, where the value of $\vec{J}$ on the i^{th} iteration is given in terms of $\vec{J}$ on the $(i-1)^{th}$ iteration by

$$\vec{J}^{i} = \vec{G} + f\,\vec{J}^{i-1} \quad . \tag{8}$$

For the numerical solution in this work, the simplest form of interpolation was used to evaluate $\vec{J}(\tau)$ and $\partial\vec{J}(\tau)/\partial\tau$. Over the interval $t - \Delta t < \tau < t$, the function $\vec{J}(\tau)$ was assumed to be linear. The function

$$\overrightarrow{FEQ} = \frac{\overrightarrow{J(\tau)}}{R} + \frac{\partial\vec{J}(\tau)}{\partial\tau} \tag{9}$$

where

$$\tau = t - R \quad ,$$

which appears in Eq. (1) must be represented numerically. A linear interpolation of $J(\tau)$ yields

$$\frac{\partial\vec{J}(\tau)}{\partial\tau} = \overrightarrow{const}$$

$$\vec{J} = \vec{J}(t) - R\,\frac{\partial\vec{J}(\tau)}{\partial\tau} \quad .$$

So that

$$\overrightarrow{FEQ} = \vec{J}(t)/R \quad . \tag{10}$$

Note that with this simple interpolation formula there is no contribution to the $\vec{G}$ term in Eq. (5). Thus,

$$F_{\ell} = \left[\frac{1}{R} \right]$$

in Eq. (4).

At this point, it is useful to relate the iterative solution given in Eq. (8) to the matrix inversion solution given in Eq. (6). The solution by matrix inversion in Eq. (6) is written as

$$\vec{J} = (1 - f)^{-1} \vec{G} \quad .$$

Formally the solution to this equation may be written in terms of the expression

$$\vec{J} = (1 + f + f^2 + f^3 + \ldots) \vec{G} \tag{11}$$

which is valid and converges, provided $|f| < 1$.

Consider now the iterative solution given in Eqs. (7) and (8) as

$$\vec{J}^1 = (1) \vec{G}$$

$$\vec{J}^2 = (1 + f) \vec{G}$$

$$\vec{J}^3 = (1 + f + f^2) \vec{G} \quad , \text{etc.} \tag{12}$$

Thus, it can be seen that the iterative solution in the i^{th} iteration gives the first i terms in a series representation of the matrix solution. This

should converge if f is less than unity, and the smaller f is, the faster the convergence will be.

In the solution of targets with edges, the patch size (linear dimension) in the edge neighborhood was taken to be one-half the patch size over the smooth parts of the targets. This yielded a value of f that ranged between 0.1 and 0.3 and provided very rapid convergence. Thus, for this work only three iterations were necessary to converge to the solution.

In addition, in the numerical solution process the value of f is zero for all patches for which the minimum spacing to other patches is greater than Δt . For these cases, the first estimate is exact and no iterations are required. In the numerical process, this fact is exploited and the increase in computer time required to apply this technique is minimal.

In summary, this technique for treating bodies with edges allows a variable patch size over the target and provides a solution procedure which yields accurate solutions efficiently and economically.

2.2 SMOOTHED IMPULSE RESPONSE COMPUTATIONS FOR BODIES WITH EDGES

The numerical solution of the space-time integral equation for bodies with edges was carried out using the technique described in Sec. 2.1.2. In addition, the self-term correction was also used in this solution to account for the non-zero curvature in the patch on which the observer is located. The following section presents results for a flat-end sphere-cap cylinder and for a right-circular cylinder. The incident pulse used for these computations was a Gaussian regularization of an impulse given by

$$e(t/a) = \frac{n}{\sqrt{\pi}} \exp\left[(na)^2(t/a)^2\right] . \qquad (13)$$

For these computations, the width parameter was taken to be

$$na = 1$$

so that the base width of the incident pulse was approximately $4a$.

2.2.1 Flat-End Sphere-Cap Cylinder

The geometry representation of the flat-end sphere-cap cylinder used for the computations presented in this section is displayed in Fig. 2. This target possessed a radius of a and an overall length of $5a$. On the cylinder body, there were 8 bands of width $0.475a$ with each band containing 7 patches in the $x > 0$ space region. On the sphere cap, there were 3 bands of arc width 30° with the bands containing 2, 6, and 7 patches, respectively. On the flat end there were two major bands as can be seen in Fig. 2. In the edge region, the patch size was chosen to be approximately one-half of the average patch size. On both the cylinder body and the flat end a bandwidth of $0.2a$ was chosen for the edge region. The average standard patch size was approximately $0.2a^2$ and the average edge patch size was approximately $0.05a^2$. The minimum spacing between sample points (which occurred on edge patches) was approximately $0.14a$ and a time increment of $0.3a$ was chosen for the computations.

The smoothed impulse response that results for the case of TE polarization is displayed in Figs. 3 and 4 for angles of incidence that range from 0° to 180° in 30° increments. For 0° incidence, the initial part of the return very closely approximates the derivative of the incident pulse or a smoothed doublet. The return from the sides of the cylinder is negligible. The second negative pulse which appears is due to the return from the far sphere-cap join region. Finally, the second positive pulse can be attributed to a wave which travels around the rear of the structure. As the angle of incidence increases from 0° to 90° the smoothed doublet becomes very smeared out and the creeping wave return appears earlier in time after the first positive pulse, as expected. On increasing the angle of incidence still further from 90° to 180°, the stability of size and shape of the initial pulse, particularly at 120°, 150°, and 180° should be noted. This initial pulse is the specular return from the spherical end-cap, which doesn't change over this range of angles and in fact is simply a smoothed impulse followed by a negative smoothed step. At 180° incidence it is interesting to compare the result to

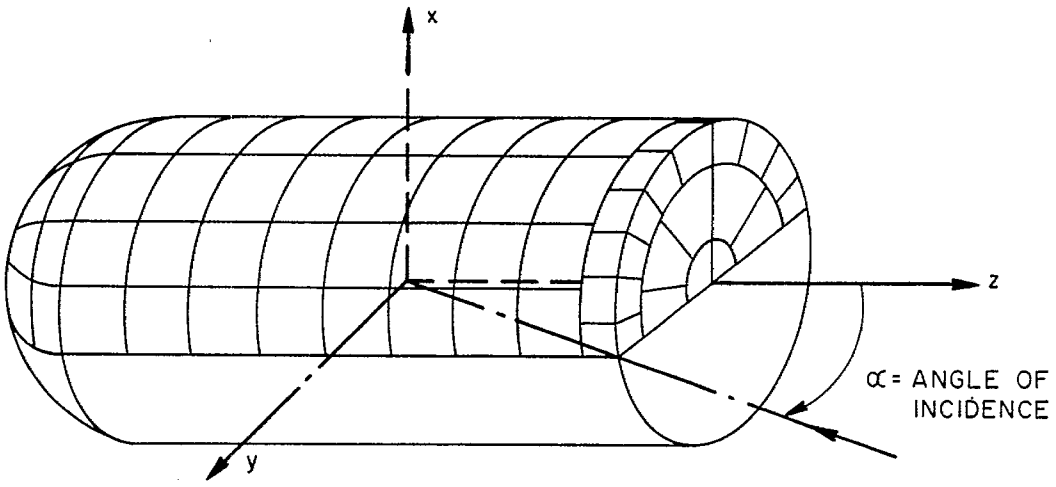

FIG. 2 Numerical representation of a flat-end sphere-cap cylinder with radius a and length 5a.

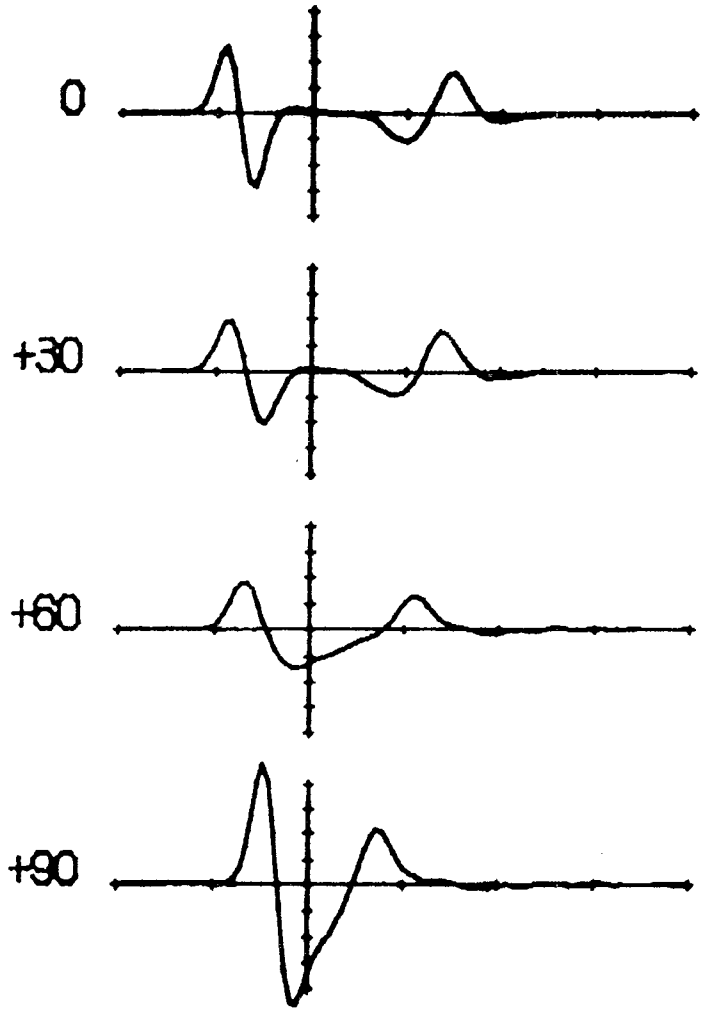

FIG. 3 Smoothed impulse response of flat-end sphere-cap cylinder with radius a and overall length 5a for TE polarization (horizontal scale: $t/a = 5/\text{div.}$; vertical scale: $r_o H^s(t/a) = 0.1/\text{div.}$).

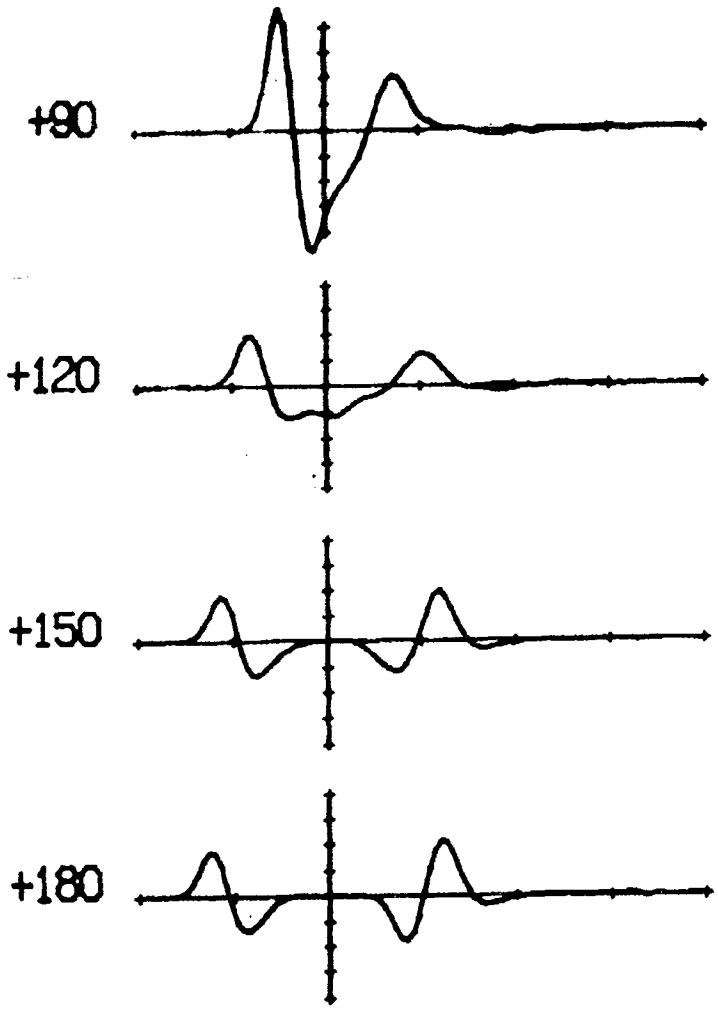

FIG. 4 Smoothed impulse response of flat-end sphere-cap cylinder with radius a and overall length 5a for TE polarization (horizontal scale: $t/a = 5/\text{div.}$; vertical scale: $r_o H^s(t/a) = 0.1/\text{div.}$).

that which was obtained for 0° incidence. At 180° incidence, the initial return is a smoothed impulse followed by a negative step, whereas at 0° incidence the initial return is a smoothed doublet. The return from the far end and the creeping wave is larger for the case of 180° incidence than it is for 0° incidence.

The smoothed impulse response that results for the case of TM polarization is displayed in Figs. 5 and 6 for angles of incidence that range from 0° to 180° in 30° increments. The response for both 0° incidence and for 180° incidence is identical to that obtained for the case of TE polarization due the rotational symmetry of the scattering problem for these two angles of incidence. Moving off from axial incidence, the effects of polarization become very apparent. The time of the creeping wave arrival after the incident pulse varies only slightly for TM polarization because the path of the creeping wave transversal is along the cylinder length for all aspect angles. Also note that the amplitude of the initial return at broadside (90°) incidence is larger in the TM case than in the TE case. In addition, at 90° incidence at $t/a \approx 2$ a small negative pulse is observed which can be attributed to the far edge of the flat end. Finally, the effect of waves traveling the length of the cylinder can be seen for the TM case, especially at 60°, 90°, and 120°.

2.2.2 Right-Circular Cylinder

The geometry of the right-circular cylinder used for computing the results presented in this section is displayed in Fig. 7. The radius of this cylinder was taken to be a and the length to be $4a$. This yielded a target with a length-to-diameter ratio of 2 to 1. For the numerical computation, the surface of the target was divided into patches and the current was computed at the center of each patch using the numerical technique described in Secs. 2.1.1 and 2.1.2. These computations were carried out only in the upper half x space and use was made of the planar symmetry in the problem. The patch distribution used for these computations is displayed in Fig. 7. The bandwidth of the standard patches on the ends was taken to be $0.4a$ and on the cylinder body was taken to be $0.5a$. The bandwidth of the patches adjacent to the edge was taken on the end to be $0.2a$ and on the cylinder to be $0.25a$. The average standard patch size was approximately $0.20a^2$ and the average edge patch size was approximately

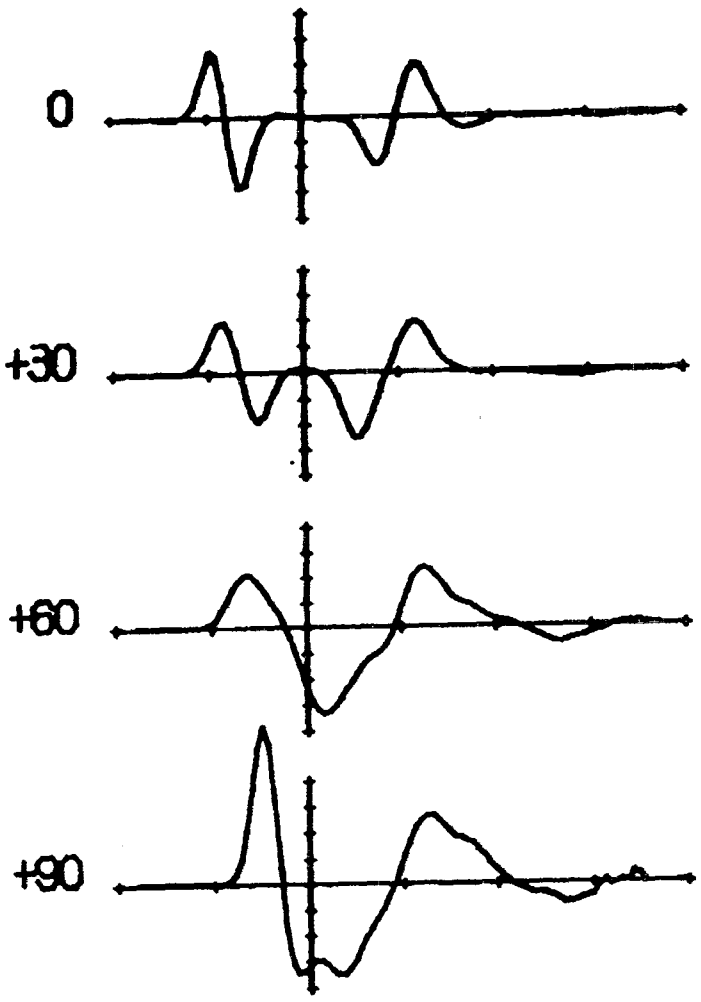

FIG. 5 Smoothed impulse response of flat-end, sphere-cap cylinder with radius a and overall length 5a for TM polarization (horizontal scale: $t/a = 5/\text{div.}$; vertical scale: $r_o H^s(t/a) = 0.1/\text{div.}$).

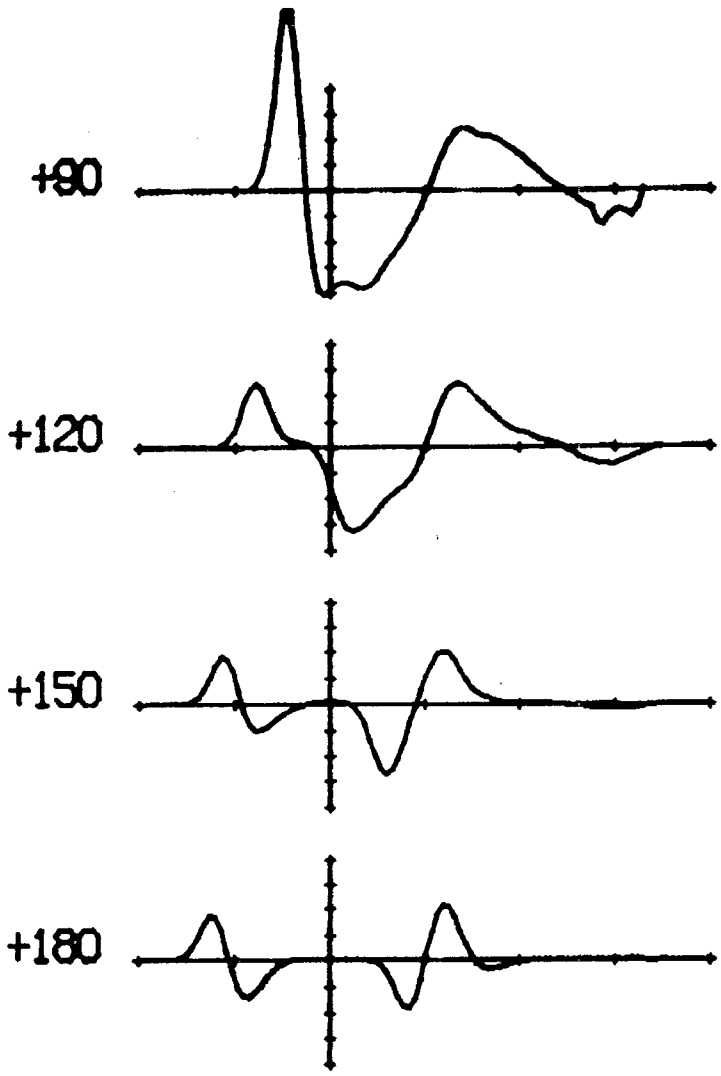

FIG. 6 Smoothed impulse response of flat-end, sphere-cap cylinder with radius a and overall length 5a for TM polarization (horizontal scale: $t/a = 5$/div.; vertical scale: $r_o H^s(t/a) = 0.1$/div.).

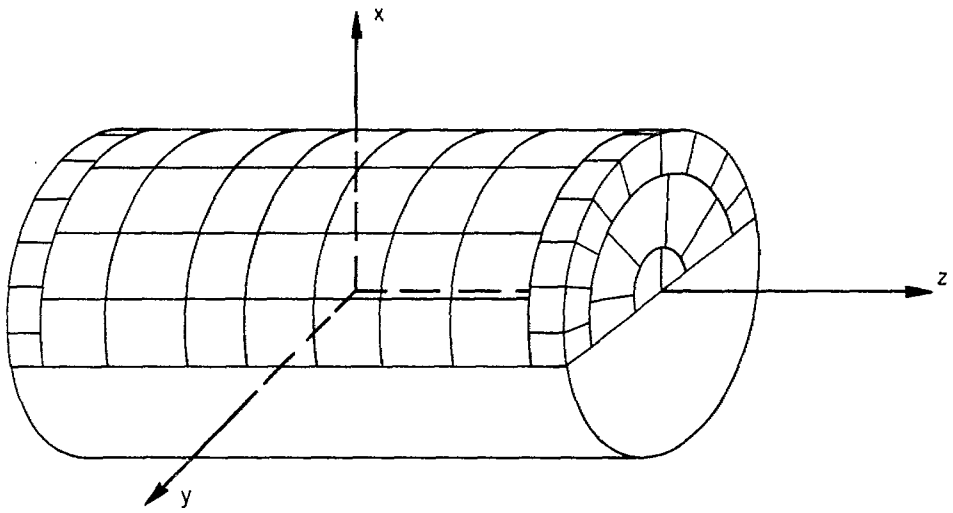

FIG. 7 Numerical representation of right-circular cylinder geometry with radius a and length 4a.

$0.05a^2$. The minimum spacing between edge patches was approximately 0.16a and the time increment chosen for the computations was 0.3a.

The smoothed impulse response of the right-circular cylinder that results for the case of TE polarization is displayed in Fig. 8 for angles of incidence that range from 0° to 90°. At 0° incidence, the initial return is identical to that obtained in Fig. 3 for the flat-end sphere-cap cylinder until the effect of the far end has had time to travel to the observer. Again the return from the far end of the cylinder is a second negative pulse which gradually disappears as the angle of incidence becomes larger. Also, the second positive pulse, which is due to the creeping wave, moves closer to the specular return as the distance it must travel decreases from the length of the cylinder at 0° incidence to the circumference of the cylinder at 90°.

The smoothed impulse response of the right-circular cylinder that results for the case of TM polarization is displayed in Fig. 9 for angles of incidence that range from 0° to 90° in 30° increments. The response at 0° incidence is identical to that obtained for the case of TE polarization due to the rotational symmetry of the problem for this angle of incidence. As the angle of incidence increases from 0°, it is interesting to note that the time of the creeping wave return remains relatively constant for TM polarization. This is due to the fact that the creeping wave travels along the length of the cylinder for all angles of incidence. As the angle of incidence increases from 30° to 90° the effect of traveling waves is more apparent than it was for the TE case, as evidenced by the second negative swing at $t/a > 10$. Finally, it is also interesting to note that the return from the far edge of the flat end can be seen at $t/a \approx 2$ for 90° incidence.

2.3 IMPULSE RESPONSE AUGMENTATION TECHNIQUE FOR BODIES WITH EDGES

The space-time integral equation approach solves the scattering problem directly in the time domain. This approach is valid for any excitation; however, the most useful excitation has been found to be the regularized (or smoothed) impulse given in Eq. (13). The response due to this excitation, $r_o H^s(t_f/a)$, is the regularized (or smoothed) impulse response of the target and is computed exactly with the space-time integral equation using the tech-

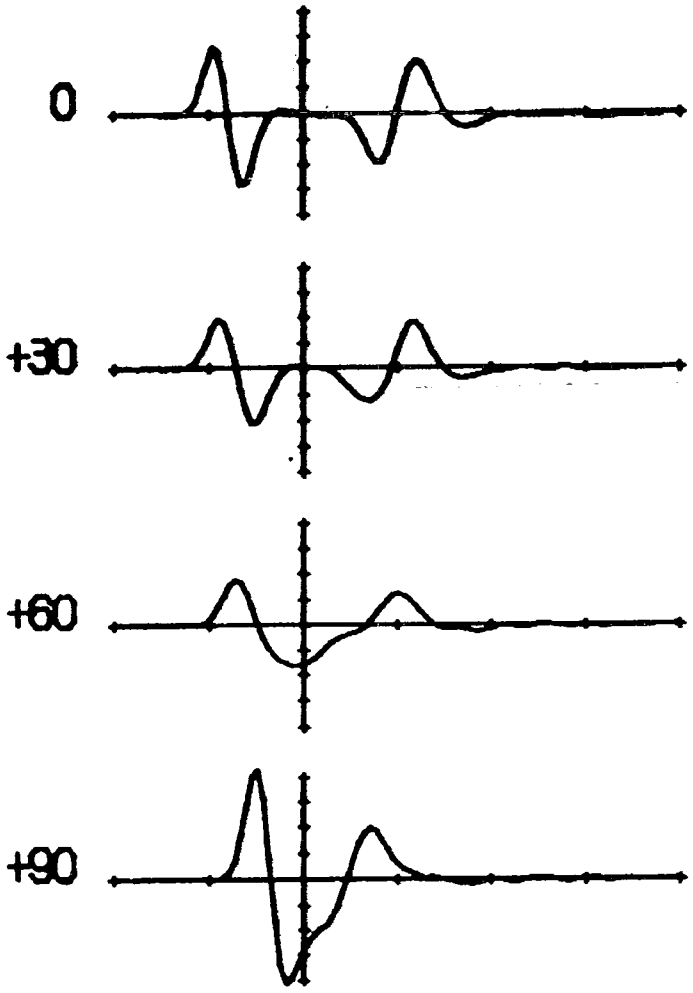

FIG. 8 Smoothed impulse response of right-circular cylinder with radius a and length 4a for TE polarization (horizontal scale: t/a=5/div.; vertical scale: $r_o H^s(t/a)$=0.1/div.).

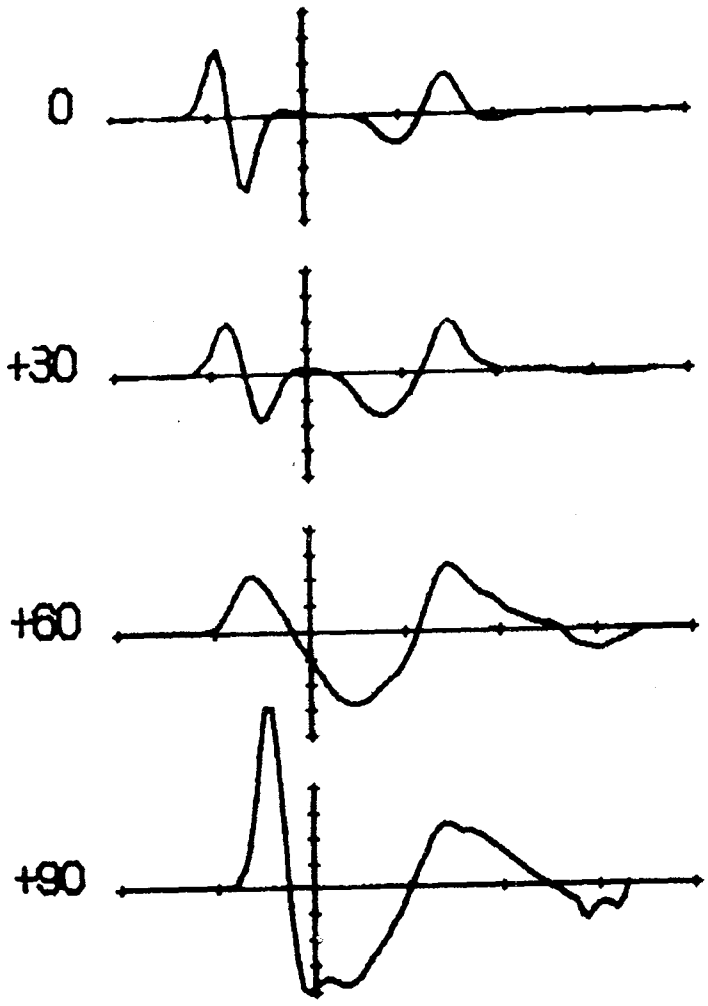

FIG. 9 Smoothed impulse response of right-circular cylinder with radius a and length 4a for TM polarization (horizontal scale: t/a=5/div.; vertical scale: $r_o H^s(t/a)$=0.1/div.).

niques described in Sec. 2.1. This approach yields results for targets with sizes up to several pulse widths or, equivalently in the frequency domain, several wavelengths.[5]

A technique has been developed recently which uses the space-time integral equation approach as the basis and extends the results to obtain the impulse response and frequency response of an arbitrary target over the entire spectrum.[3] This technique has been demonstrated for several smooth convex targets including the sphere, the prolate spheroid, and the sphere-capped cylinder. The purpose of the sections which follow is to describe the extension of the impulse response augmentation technique to targets with edges. Section 2.3.1 provides a review of the impulse response augmentation technique. Section 2.3.2 presents the results obtained by applying it to the flat-end sphere-cap cylinder for both 0^{o} and 180^{o} incidence. Finally, Sec. 2.3.3 describes the application of the technique to the right-circular cylinder and presents the results which were obtained.

2.3.1 Review of the Impulse Response Augmentation Technique

In order to simplify the notation in these sections the electromagnetic field variables are equated to their linear system counterparts as described below:

$$H^{i}(t/a) \rightarrow e(t) = \text{incident pulse}$$

$$r_{o}H^{s}(t_{f}/a) \rightarrow r(t) = \text{smoothed impulse response}$$

$$h(t) = \text{impulse response}$$

$$t/a \rightarrow t = \text{time}$$

$$H^{i}(ka)/a \rightarrow E(\omega) = \text{transform of } e(t)$$

$$r_{o}H^{s}(ka)/a \rightarrow R(\omega) = \text{transform of } r(t)$$

$$H(\omega) = \text{frequency response}$$

$$ka \rightarrow \omega = \text{frequency}$$

where

H^i = incident magnetic field intensity

H^s = far scattered magnetic field intensity

r_o = distance of far field observer from origin

t/a = normalized time

ka = normalized frequency

a = characteristic linear dimension of target.

The scaling and normalization that is indicated above yields curves which are independent of target size.

The impulse response augmentation technique, first suggested in 1968[1] and first demonstrated for smooth convex targets in 1973,[3] deals directly with the smoothed impulse response of the target in the far field. The smoothed impulse response is computed using a space-time integral equation approach and has yielded good results up to body sizes of several pulse widths or, equivalently, up to body sizes of several wavelengths. The regions of slow variation in the smoothed impulse response remain the same in the exact impulse response; thus it is only necessary to determine the structure of the singular regions and any other regions of fast variation. But the singular portions of the exact impulse response that result from scattering by specular points on smooth convex targets can be computed exactly and hence do not need to be computed by solving the space-time integral equation. The impulse response augmentation technique combines the smoothed impulse response, the known singular contribution to the impulse response, and the theory of Fourier transforms to produce the total impulse response and the frequency response (system function) of the target at all frequencies.

The impulse response augmentation technique is most easily understood by considering the most basic approach to the deconvolution (or system identification) problem. Figure 10 shows the functional diagram of a linear

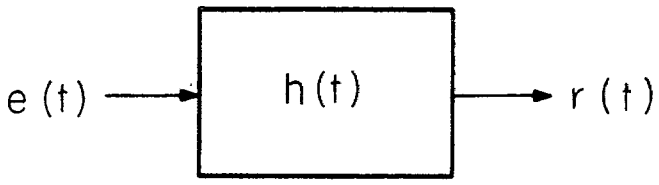

FIG. 10 Linear system.

system (in this case electromagnetic scattering by a target) that is characterized by its impulse response $h(t)$ or, equivalently, its system function (or frequency response) $H(\omega)$. Of course,

$$h(t) \Leftrightarrow H(\omega)$$

where $\Leftrightarrow$ denotes Fourier transform. The excitation $e(t)$ of the linear system in this case is the regularized (or smoothed) impulse

$$e(t) = \frac{n}{\sqrt{\pi}} e^{-(nt)^2} \tag{14}$$

which produces the regularized (or smoothed) impulse response $r(t)$ of the system. This response is given by

$$r(t) = e(t) * h(t) \tag{15}$$

where $*$ represents a convolution. In the problem being considered here, $e(t)$ is specified analytically and $r(t)$ is computed by solving the space-time integral equation. It is desired to find $h(t)$ and/or $H(\omega)$. This is the system identification or deconvolution problem.

One way to solve this problem, at least in principle, is to transform Eq. (15) and rearrange to obtain

$$H(\omega) = \frac{R(\omega)}{E(\omega)}$$

$$h(t) = F^{-1}\{H(\omega)\} \tag{16}$$

where

$E(\omega) \Leftrightarrow e(t)$

$R(\omega) \Leftrightarrow r(t)$

$F^{-1}\ \{\ \}$ is the inverse Fourier transform.

However, the estimate of the system response $\hat{r}(t)$ that is computed contains some uncertainty or noise, and thus, the transform of the computed smoothed impulse response $\hat{R}(\omega)$ also contains some noise. In using Eq. (16) to compute the estimate of the system function, it can be shown that this noise grows exponentially,[3] and therefore this brute force technique will not yield valid large body results.

The impulse response augmentation technique is displayed in block diagram form in Fig. 11. This technique first augments the smoothed impulse response to remove the contribution from singular portions of the impulse response that are known exactly. This produces the augmented smoothed impulse response $r_a(t)$ that is given by

$$r_a(t) = r(t) - e(t) * f_a(t) \tag{17}$$

where $f_a(t)$ is a suitable augmentation function that contains the known singular portions of the impulse response.

Next, the transform of the augmented smoothed impulse response, $R_a(\omega)$, is computed and divided by the transform of the incident pulse to yield the augmented frequency response, $H_a'(\omega)$. This function contains noise which increases exponentially at frequencies above some value. However, it is known that the augmented frequency response must go to zero with increasing frequency. Thus, an estimate of the high frequency behavior of the augmented frequency response, $\hat{H}_a(\omega)$, is of the form

$$\hat{H}_a(\omega) = \begin{cases} H_a'(\omega) \; ; \; \omega \leq \omega_c \\ \\ F(\omega) \; ; \; \omega \geq \omega_c \end{cases} \tag{18}$$

where ω_c is the boundary point and $F(\omega)$ is the high frequency estimate of $H_a(\omega)$. The inverse Fourier transform of $\hat{H}_a(\omega)$ then yields the estimate of the augmented impulse response, $\hat{h}_a(t)$.

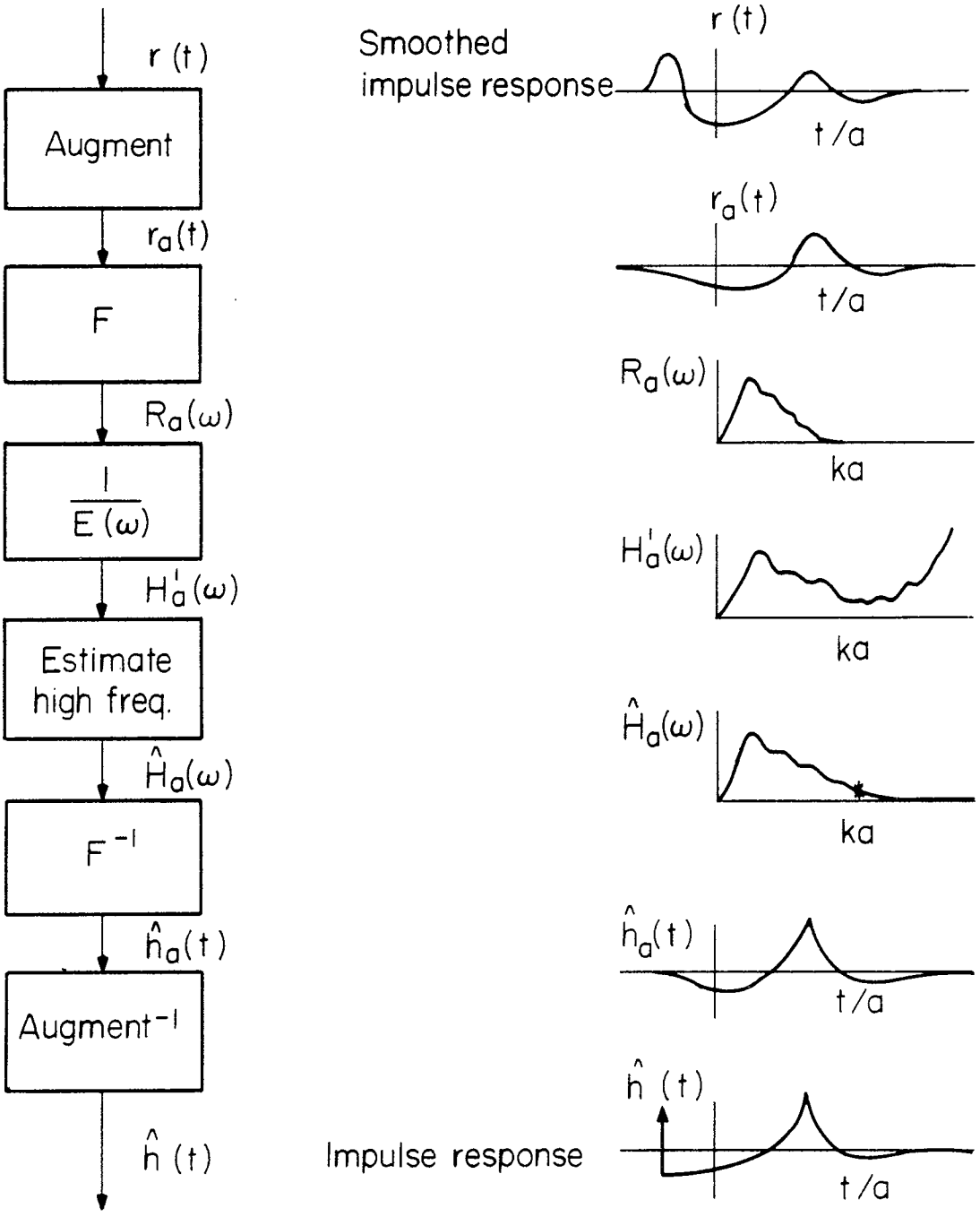

FIG. 11 Impulse response augmentation technique.

Finally, the inverse of the augmentation procedure is performed on $\hat{h}_a(t)$, which yields the estimate of the impulse response, $\hat{h}(t)$. Moreover, an estimate of the system function, $\hat{H}(\omega)$, is obtained by applying the inverse of the augmentation procedure in the frequency domain to $\hat{H}_a(\omega)$.

The augmentation function represents the contributions of the singular portions of the impulse response which are known exactly from optics considerations. These singular portions may contribute to not only the high frequency behavior but also to the low frequency behavior of the response, as in the case of an impulse. These contributions are removed by subtracting the effect of the augmentation function $f_a(t)$ from the response to yield the augmented response as given in Eq. (17), which is repeated here for convenience:

$$r_a(t) = r(t) - e(t) * f_a(t) \tag{17}$$

or

$$h_a(t) = h(t) - f_a(t) \quad .$$

Since the effect of the optics or high frequency contributions has been removed, then it remains to estimate the manner in which the lower frequency components approach zero with increasing frequency.

It has been found in previous work[3] that the augmentation functions should be chosen such that they account for the singular contributions to the impulse response but at the same time possess a transform that contains only linear phase variations. The functions which satisfy this simple criterion are singularity functionals and psuedo-functions that contain only a single discontinuity. Some functionals which possess this characteristic are the doublet, the impulse, the step, and Hadamard's psuedo-functions.[6] It has also been found that the singular portion of the impulse response at the leading edge region would be given by the physical optics approximation for aspect angles where the response was polarization independent, such as axial incidence on rotationally symmetric targets.

2.3.2 Flat-End Sphere-Cap Cylinder

This section describes the application of the impulse response augmentation technique to the flat-end sphere-cap cylinder for axial incidence at the two viewing angles. This target provides the logical extension of the previous work[3] which considered the circular cylinder with sphere caps on both ends. The target geometry of this target is shown in Fig. 2 with its axis coinciding with the z axis. Flat-end incidence corresponds to the 0° aspect angle and sphere-cap incidence corresponds to the 180° aspect angle. This target is illuminated by an incident plane wave given by

$$e(z,t) = \frac{n}{\sqrt{\pi}} e^{-(na)^2 (t/a + z/a)^2} \tag{19}$$

where

$$na = 1$$

$$a = \text{radius of cylinder} \quad .$$

This yielded an incident pulse width equal to the length of the cylinder body.

The smoothed impulse response that was computed by the space-time integral equation as described in Sec. 2.1 is displayed in Fig. 12 for 180° incidence. This represents the response of a sphere-cap flat-end cylinder. The initial portion of the smoothed response and the impulse response is identical to that obtained from the cylinder with two sphere caps due to the identical nature of the problem over the initial time window. However, the response from the far end of this target does differ from the far-end response of the cylinder with two sphere caps.

Figure 13 shows the frequency response for this target at 180° incidence that was computed by dividing the transform of the smoothed impulse response in Fig. 12 by the transform of the incident pulse. This frequency response is valid up to a ka of approximately 3.5, after which the numerical noise increases very rapidly. The ripples that appear in this response prior

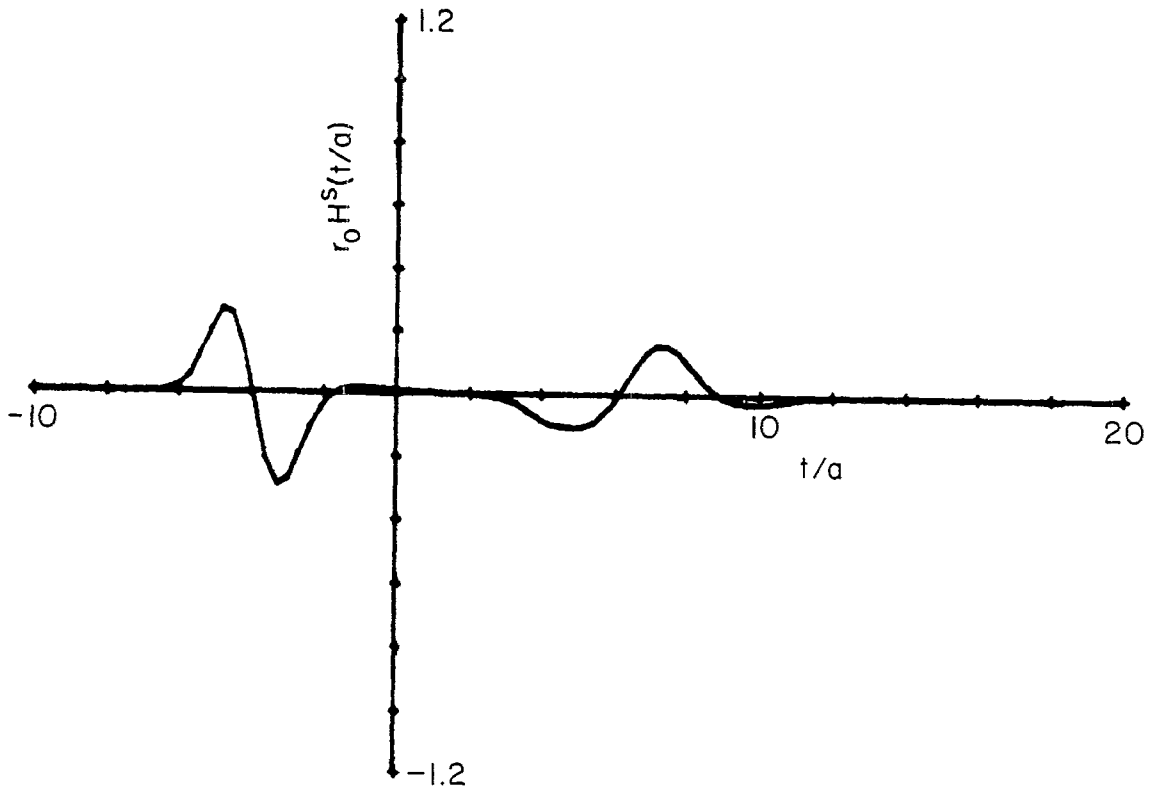

FIG. 12 Smoothed impulse response of a flat-end sphere-cap cylinder with radius a and overall length 5a at 180^0 incidence.

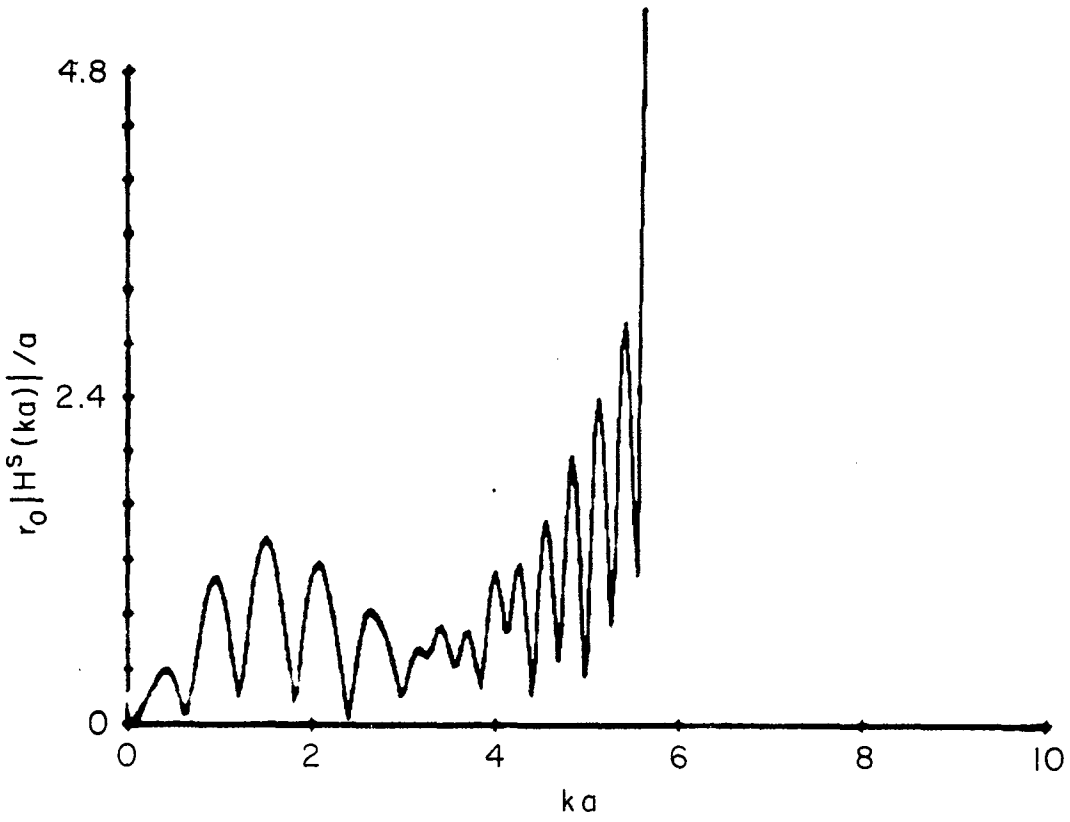

FIG. 13 Frequency response of a flat-end sphere-cap cylinder with radius a and overall length 5a at 180^0 incidence.

to ka of 3.5 are due to the interference between the return from the near end of the target and the return from the far end of the target.

In previous work[3] it was found to be convenient to divide the axial response of a cylinder with two sphere caps into two parts and consider each section separately. It is also convenient to use the same procedure for the cases presented in this and the following section. For the case of this target, the results for the front section are identical to those obtained from the cylinder with two sphere caps[3] and so only the results are presented here.

The smoothed impulse response of the front section was defined to be that part of the response in Fig. 12 that occurs before $t/a = 1.8$. The augmented frequency response that results using the augmentation function

$$f_{a1}(t) = \frac{1}{2}\,\delta(t/a+2) - \frac{1}{4}\,u(t/a+2) \tag{20}$$

is displayed in Fig. 14.

The high frequency portion of the augmented frequency response was given by

$$\hat{H}_{a1}(\omega) = \frac{A_o}{\omega^{3/2}}\,\exp(j\,b_o)\;;\quad \omega > \omega_c \tag{21}$$

where

$$\omega_c = 2.000$$

$$b_o = 1.619$$

$$A_o = 0.213$$

and the resulting high frequency estimate is shown in Fig. 14.

The impulse response $\hat{h}_1(t)$ due to this portion of the return is displayed in Fig. 15. Note that the impulse response is time limited and that it has a negligible precursor.

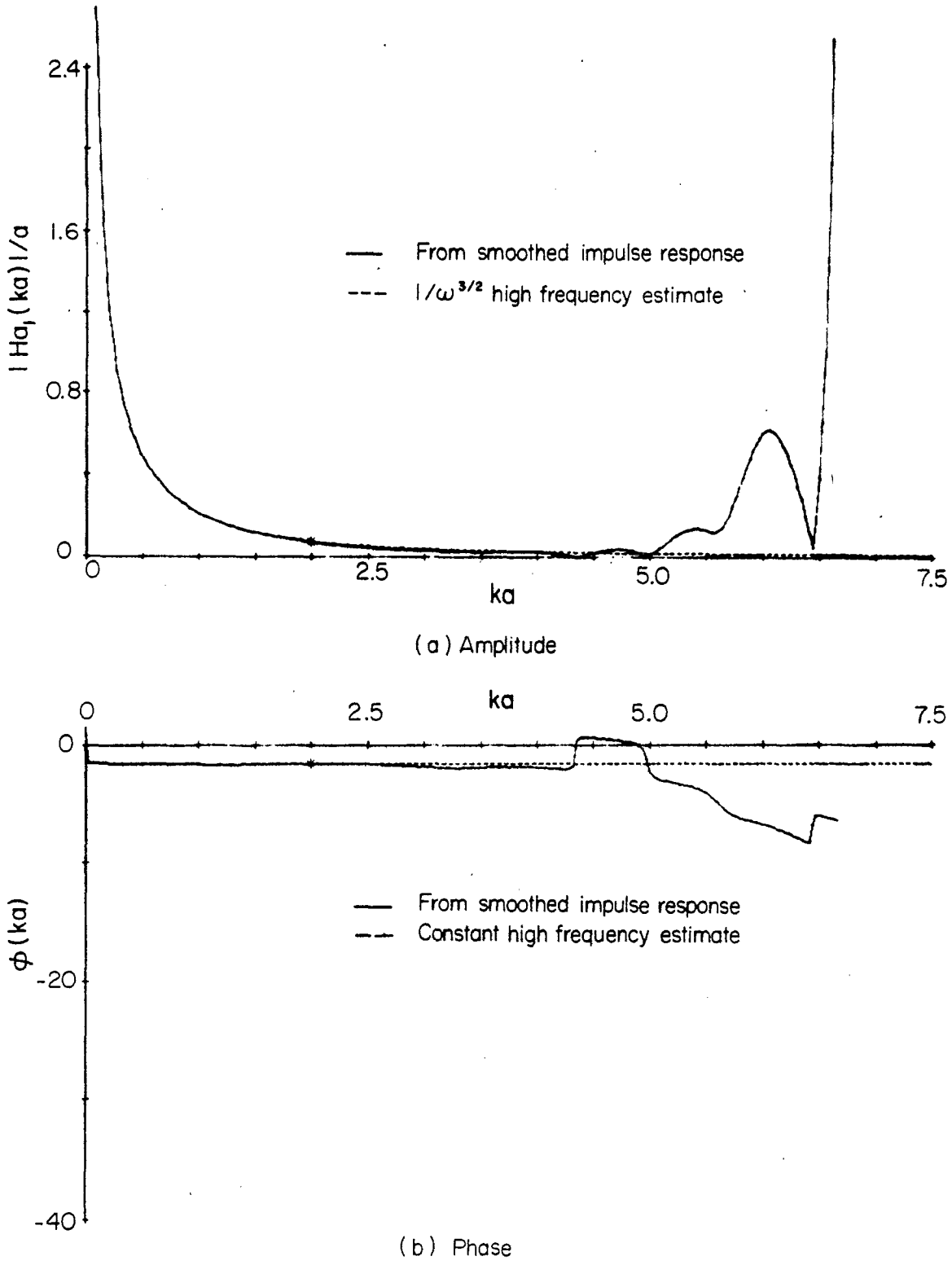

FIG. 14 Augmented frequency response of the return due to the front part of the flat-end sphere-cap cylinder at 180° incidence.

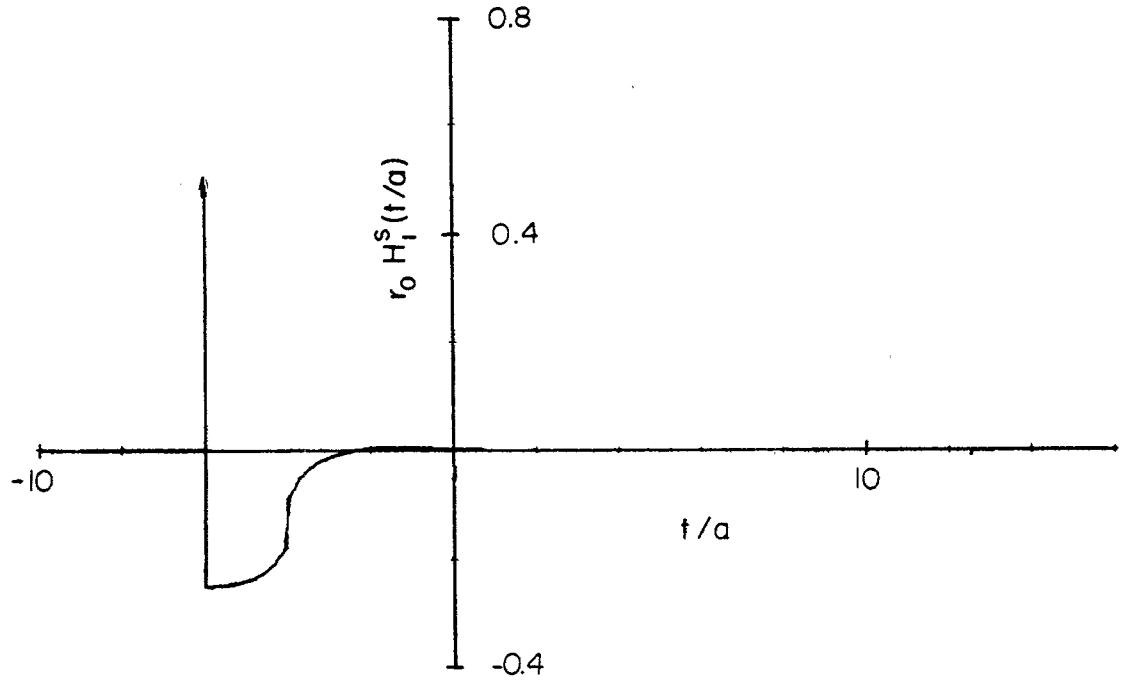

(a) IMPULSE RESPONSE

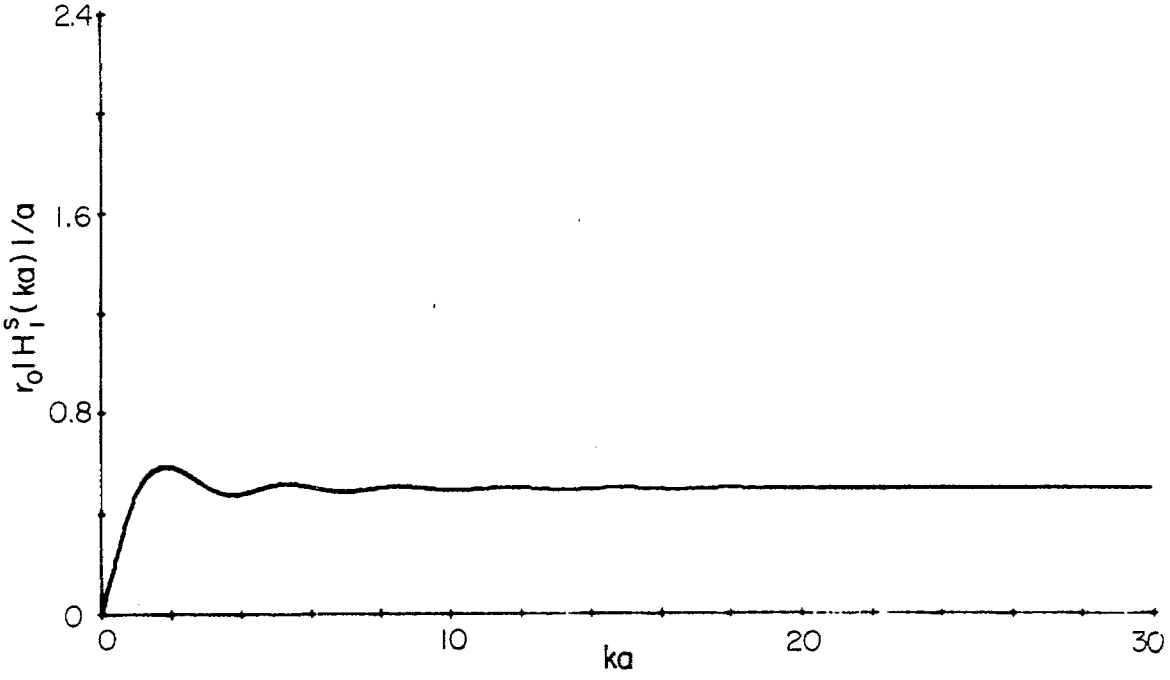

(b) FREQUENCY RESPONSE

FIG. 15 Response of the return due to the front part of the flat-end sphere-cap cylinder at 180^o incidence.

The smoothed impulse response of the far section was defined to be that portion of the response in Fig. 12 that occurs on or after $t/a = 1.8$. The augmentation function for this return is zero, since no specular points contribute to this portion of the response. Both the amplitude and phase of the augmented frequency response is displayed in Fig. 16. It is assumed that this response is due to both a return from the rear edge of the target and also a return due to a wave traveling around the rear of the target. The amplitude of the contribution due to the wave traveling around the rear was taken to be the exponential form of a creeping wave.[3] The amplitude of the return from the rear edge was taken to be $1/\omega^{\frac{1}{2}}$. The phase in both cases was assumed to be linear. Thus, the form of the high frequency estimate for the augmented frequency response is

$$\hat{H}_{a2}(\omega) = A_1 \exp(-B_1 \omega^{1/3}) \exp(j\omega m_1 + b_1) + \frac{A_2}{\omega^{1/2}} \exp(j\omega m_2 + j\, b_2); \quad \omega > \omega_c \quad . \quad (22)$$

The parameters in Eq. (22) were chosen in the following manner:

ω_1 = approximate value of frequency at which the first minimum in amplitude occurs

m_1 = the time at which a wave traveling around the rear of the cylinder would appear in the response

B_1 = the coefficient for the creeping wave of a sphere

b_2 chosen such that the time response is causal

$m_2 = \left(\varphi(\omega_1) - b_2\right)/\omega_1$

$b_1 = \varphi(\omega_1) - \omega_1 m_1 - \pi$

$\omega_2 = \omega_1 + \pi/(m_2 - m_1)$

A_1 & A_2 chosen such that

$$\hat{H}_{a2}(\omega_1) = H_{a2}(\omega_1)$$

$$\hat{H}_{a2}(\omega_2) = 0.3 \quad .$$

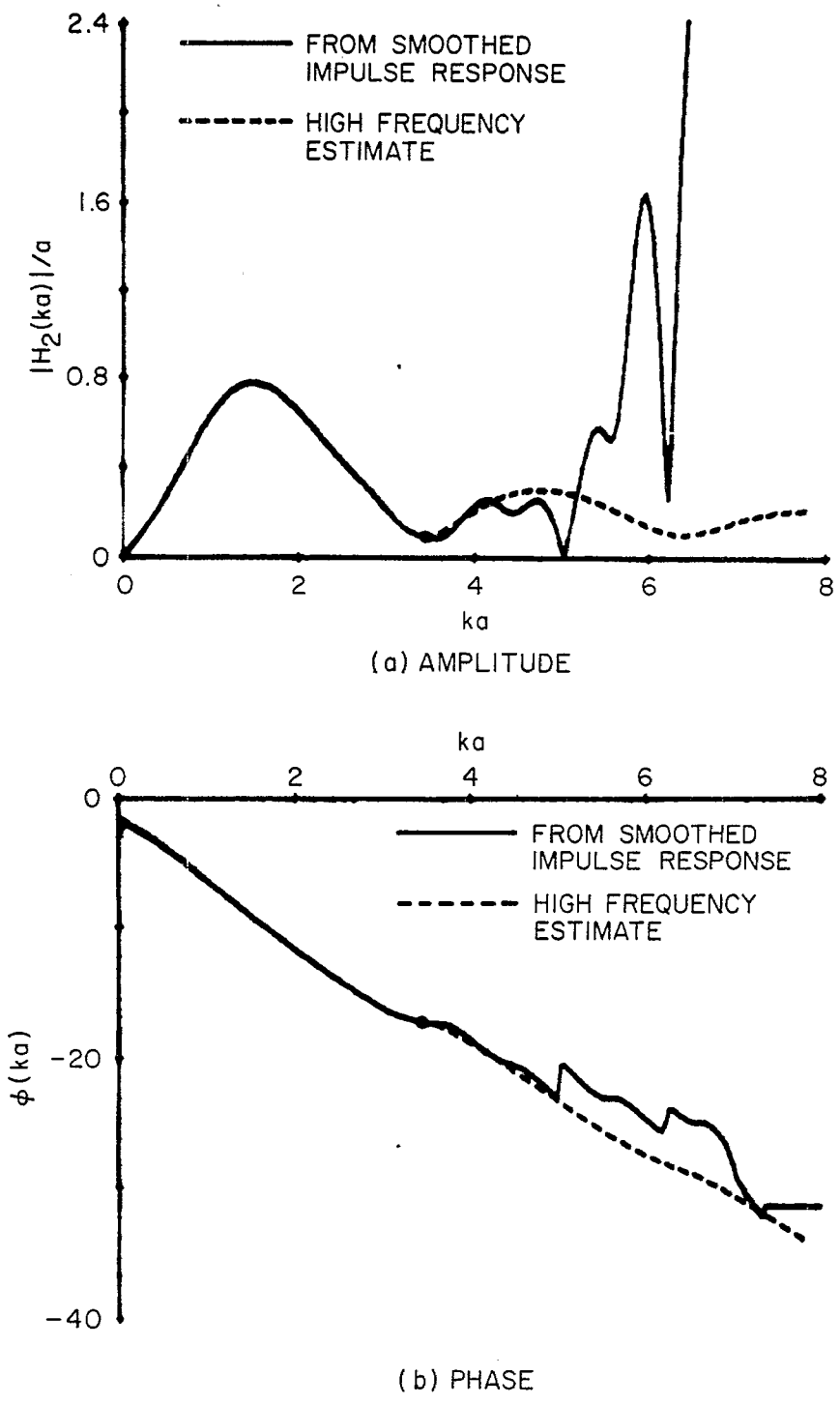

FIG. 16 Augmented frequency response of the second part of the flat-end sphere-cap cylinder response at 180^{o} incidence.

Carrying out the above procedures yields the following values for these parameters:

$$\omega_1 = 3.436$$
$$m_1 = -6.000$$
$$b_1 = 0.241$$
$$\omega_2 = 4.912$$
$$m_2 = -3.872$$
$$b_2 = -5\pi/4$$
$$|H_{a2}(\omega_1)| = 0.095$$
$$|H_{a2}(\omega_2)| = 0.300$$
$$A_1 = 3.220$$
$$B_1 = 2.051$$
$$A_2 = 0.446 \ .$$

Substituting these values into Eq. (22) yields the estimate of the high frequency portion of the augmented frequency response shown by the broken line in Fig. 16.

The impulse response of the second part of the return from the sphere-cap flat-end cylinder is displayed in Fig. 17. Note the creeping wave peak at $t/a - 6$. The return due to the far end appears as a sharp negative swing at $t/a = 3.9$, which is slightly sooner than would be expected. The form of this portion of the return is $1/(t - t_o)^{1/2}$, where t_o is the time of the singularity.

Finally, the two portions of the impulse response are combined and the resulting total impulse response is displayed in Fig. 18(a). The total frequency response is shown in Fig. 18(b). The fast variation in the response is due to the interference between the specular return and the return from the far end. The interference between the join return and the creeping wave return is also evident in the form of an amplitude modulation of the fast ripples.

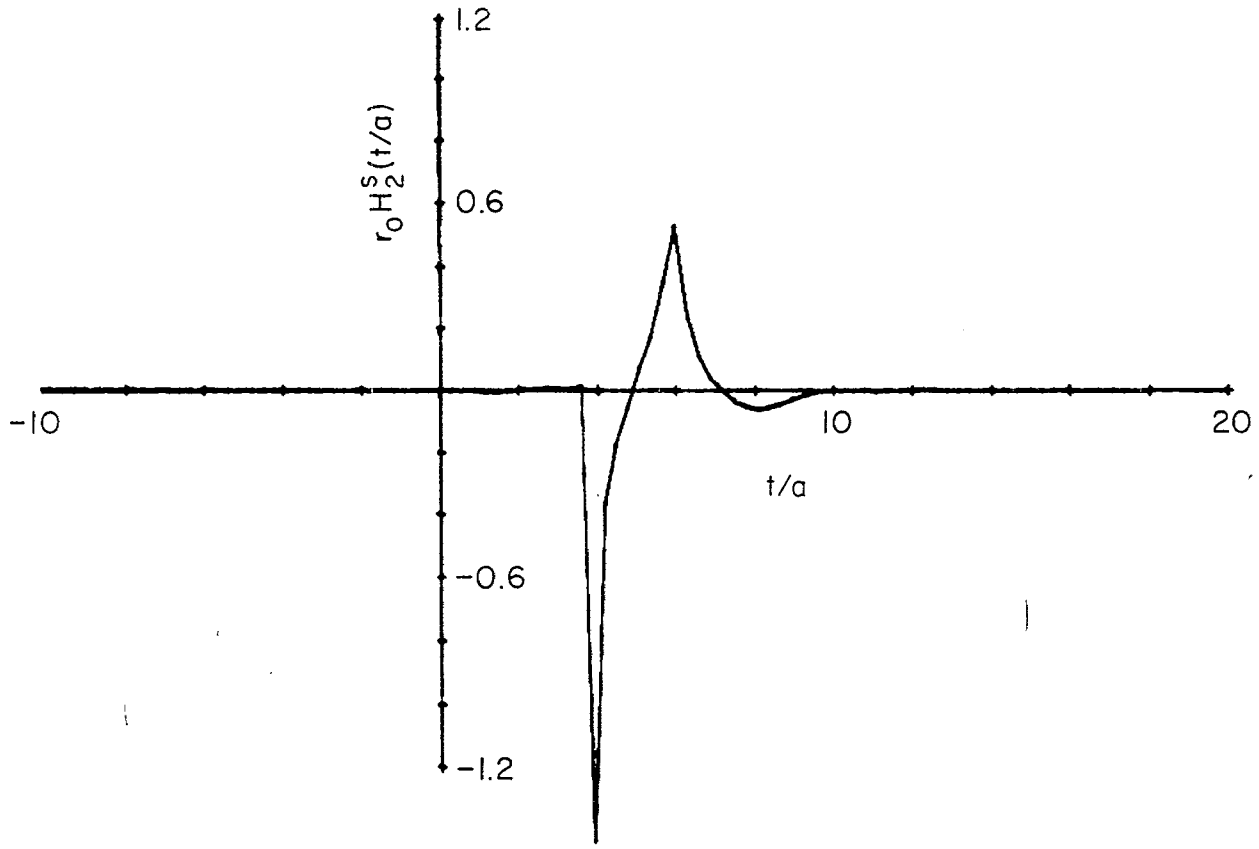

FIG. 17 Impulse response of the far end of the flat-end sphere-cap cylinder at 180° incidence as computed with the impulse response augmentation technique.

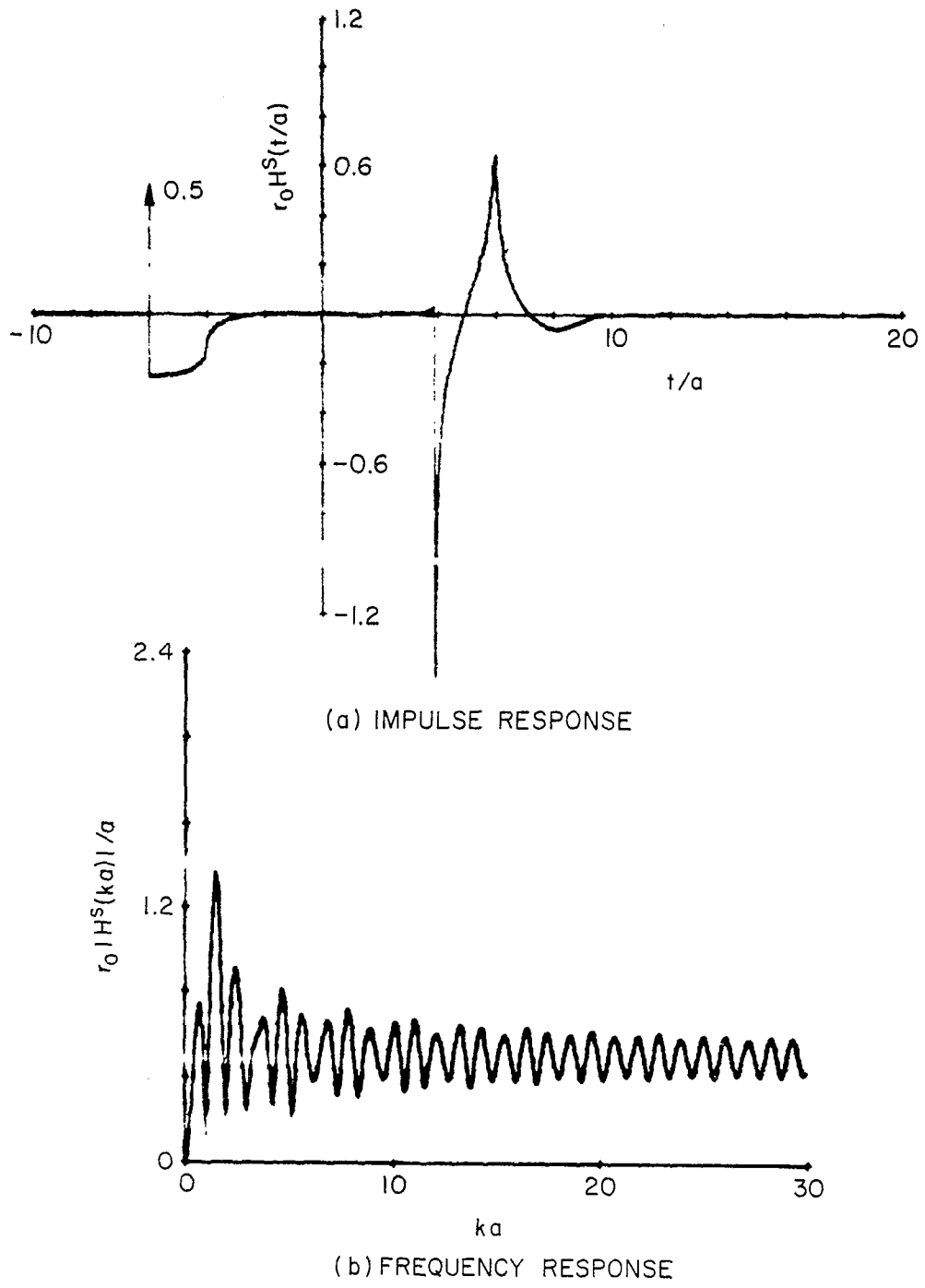

FIG. 18 Response of the flat-end sphere-cap cylinder at 180° incidence as computed with the impulse response augmentation technique.

The smoothed impulse response that was computed by the space-time integral equation as described in Sec. 2.1 is displayed in Fig. 19 for 0° incidence. This represents the response of a flat-end sphere-cap cylinder. The initial portion of this response approximates the derivative of the incident pulse, as predicted by the physical optics approximation. There is negligible return from the sides of the cylinder. Next there is a negative pulse from the join region of the far sphere-cap, which is followed by the creeping wave return at $t/a \approx 11.2$.

The frequency response of this target computed by dividing the transform of the smoothed impulse response by the transform of the excitation is shown in Fig. 20. This frequency response is valid up to approximately $ka = 3.5$, after which the numerical noise increases very rapidly. The ripple which appears before this point can be attributed to the interference between the specular return and the return from the far end. The effect of the doublet in an impulse response can also be seen in this figure as a linear function increasing with ka .

Again it is convenient to divide the response into two parts; the return from the near end of the cylinder and the return from the far end. The smoothed impulse response of the front section was defined to be the part of the response in Fig. 19 that occurred before $t/a = 1.8$. This point in time was chosen to be the point where the response possessed a zero crossing. The augmentation function used for this response is given by

$$f_{a1}(t) = D_z \delta^1(t/a - T_z) + P_z \delta(t/a - T_z) + V_z v(t/a - T_z) \qquad (23)$$

where

$$v(t - T_z) = (t/a - T_z)^{-1/2} \, u(t/a - T_z)$$

$$T_z = -4.000$$

$$D_z = 1/2$$

$$P_z = 0.141$$

$$V_z = -0.035 \ .$$

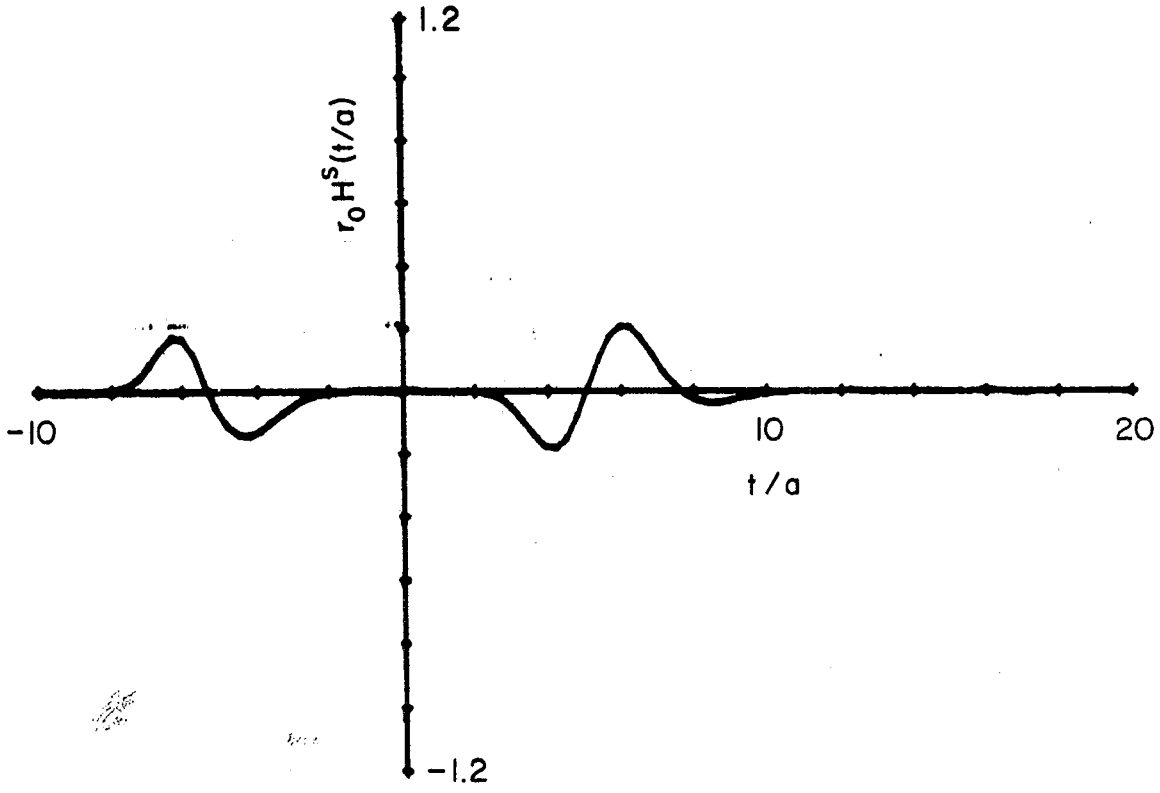

FIG. 19 Smoothed impulse response of a flat-end sphere-cap cylinder with radius a and overall length 5a at 0^o incidence.

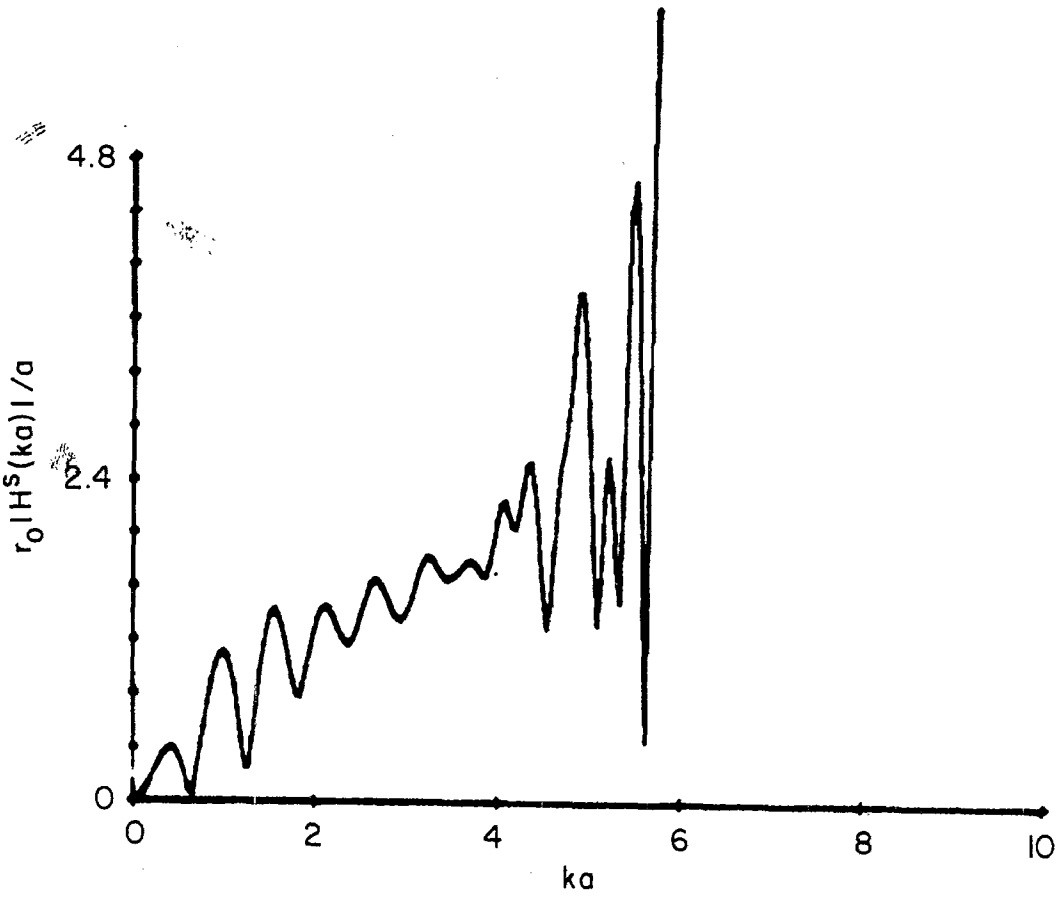

FIG. 20 Frequency response of a flat-end sphere-cap cylinder with radius a and overall length 5a at 0^0 incidence.

The coefficients for the impulse and the v function were computed using the augmented smoothed impulse response in the vicinity of $t/a = -4$. The impulse and the v function were included as part of the augmentation function as a result of a study on the far fields produced by currents in the vicinity of edges. Using the theoretical currents in the neighborhood of a 90^{o} wedge yields both an impulse and a v function in the leading edge of the far-field impulse response. The amplitude and phase of the augmented frequency response are displayed in Fig. 21.

The high frequency portion of the augmented frequency response was given by

$$\hat{H}_{a1}(\omega) = U_z \frac{\sqrt{\pi}}{\omega^{3/2}} \exp(j\omega m_o + j b_o) \; ; \; \omega > \omega_c \tag{24}$$

where

$$\omega_c = 4.173$$
$$b_o = -3\pi/4$$
$$m_o = 2.753$$
$$U_z = 0.379 \; .$$

The value of b_o was specified to give a causal time function and ω_c was chosen such that the phase was still in the linear region. Next, m_o and U_z were computed such that both the amplitude and phase of $\hat{H}_{a1}(\omega)$ and $H_{a1}(\omega)$ are equal at ω_c. The resulting augmented frequency response is shown in Fig. 21.

The impulse response $\hat{h}_1(t)$ due to this portion of the response is displayed in Fig. 22. The doublet and impulse appear initially in the response at $t/a = -4$, as expected. Subsequently, there is a negative peak at approximately $t/a = 02.75$ which could be due to a wave traveling across the front face of the cylinder, although the timing indicates it does not travel across the middle of the front face. Again note that the impulse response is time

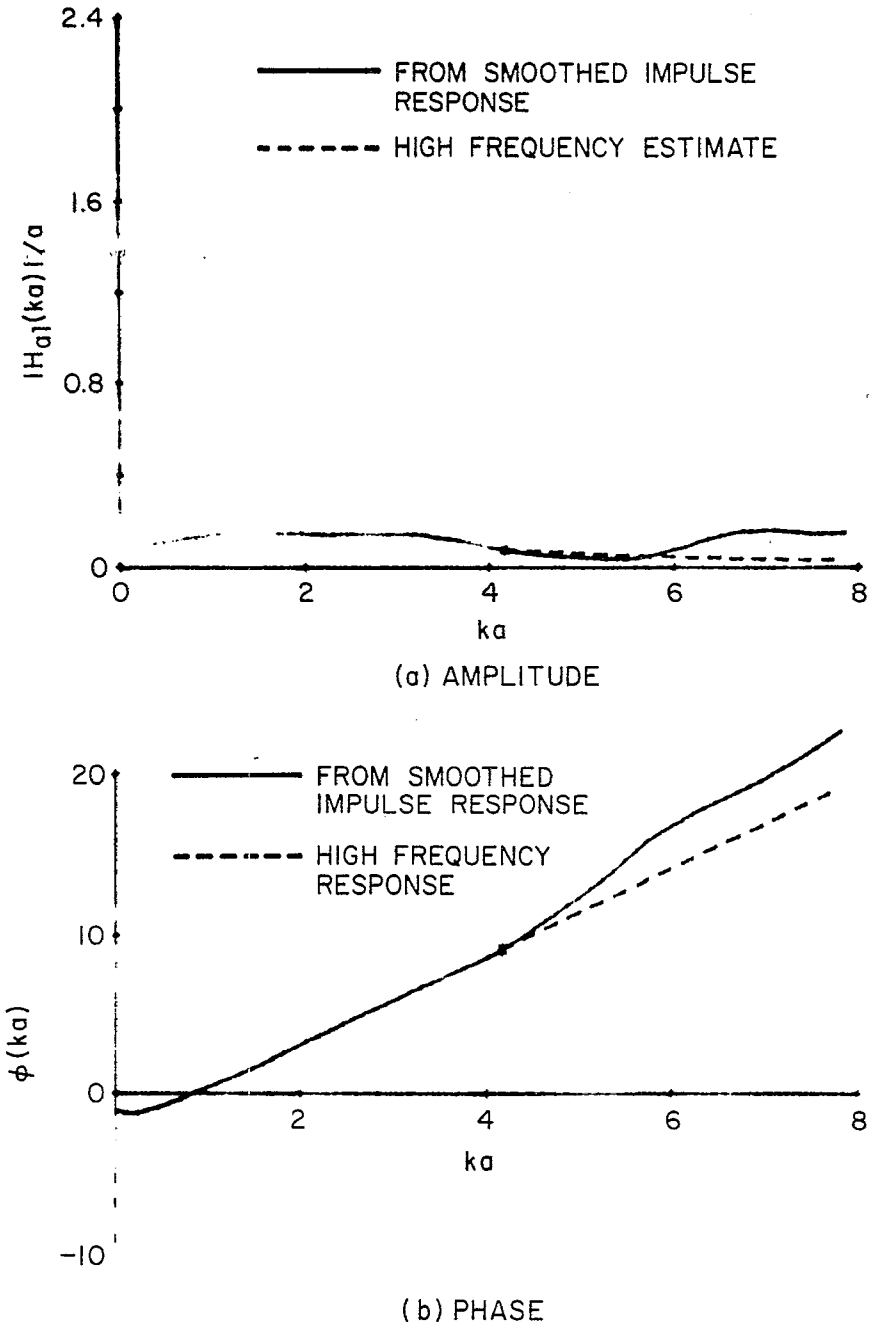

FIG. 21 Augmented frequency response due to the front part of the flat-end sphere-cap cylinder at 0^{o} incidence.

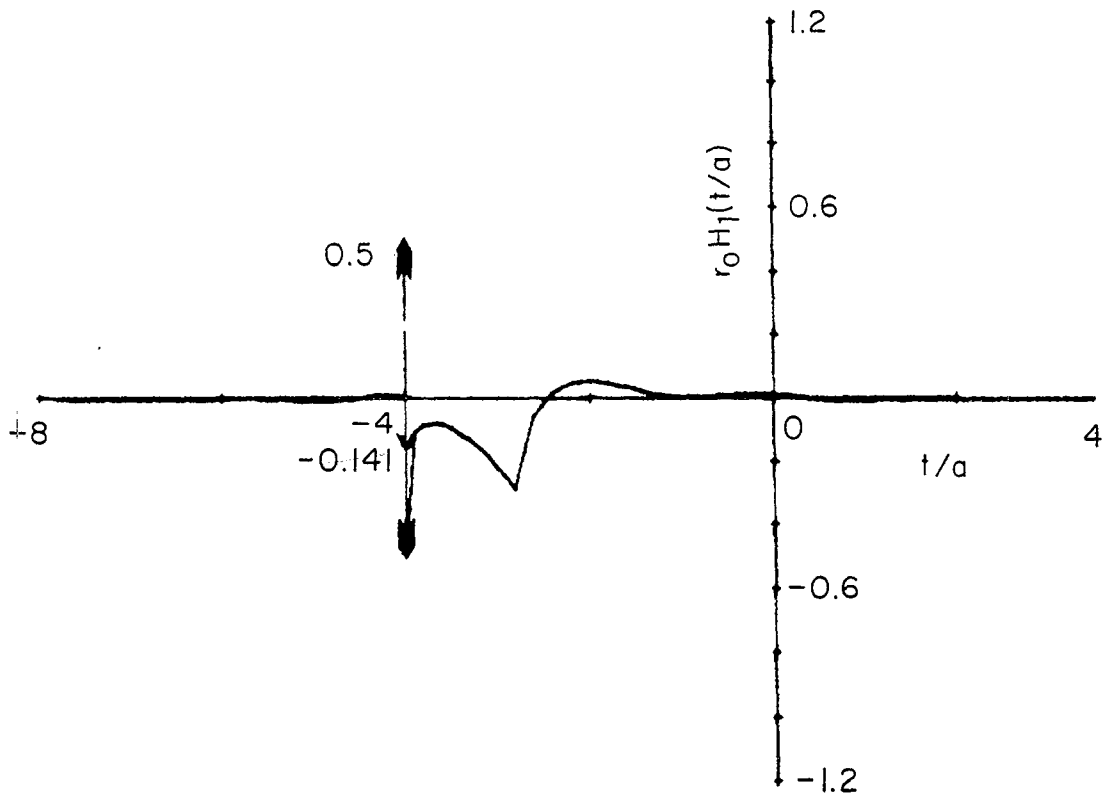

FIG. 22 Impulse response of the return due to the front part of the flat-end sphere-cap cylinder at 0^o incidence.

limited and possesses a negligible precursor.

The smoothed impulse response of the far section was defined to be that portion of the response in Fig. 19 that occurs on or after $t/a = 1.8$. The smoothed impulse response that results is nearly the same as that obtained for the far section of the cylinder with two sphere caps. This is somewhat surprising, since it indicates that the effect of the front-end currents on the response due to the far end is negligible. Thus, the technique and results used in the previous work[3] for the far end of the sphere-capped cylinder apply here for the far end of this target.

The augmentation function for this return is zero, since no specular points contribute to this portion of the response. Both the amplitude and phase of the augmented frequency response are displayed in Fig. 23. The form of the high frequency estimate for the augmented frequency response is the same as that used in previous work[3] for the far end of a sphere-capped cylinder and is given by

$$\hat{H}_{a2}(\omega) = A_1 \exp(-B_1\omega^{1/3}) \exp(j\omega m_1 + j b_1) + \frac{A_2}{\omega^{3/2}} \exp(j\omega m_2 + j\, b_2)\,;\ \omega > \omega_c\,. \qquad (25)$$

The parameters in Eq. (25) were chosen in the following manner:

ω_2 = the approximate value of frequency at which the first minimum in the amplitude response occurs; this was chosen

φ_2 = the phase at ω_2

$m_1 = \varphi_2/\omega_2$

$b_1 = 0$

t_{j2} = the time at which the second join return would first appear; this was specified

$m_2 = -t_{j2}$

$\omega_3 = \omega_2 + \pi/(m_2 - m_1)$

$b_2 = \pi - (m_2 - m_1)\,\omega_2$

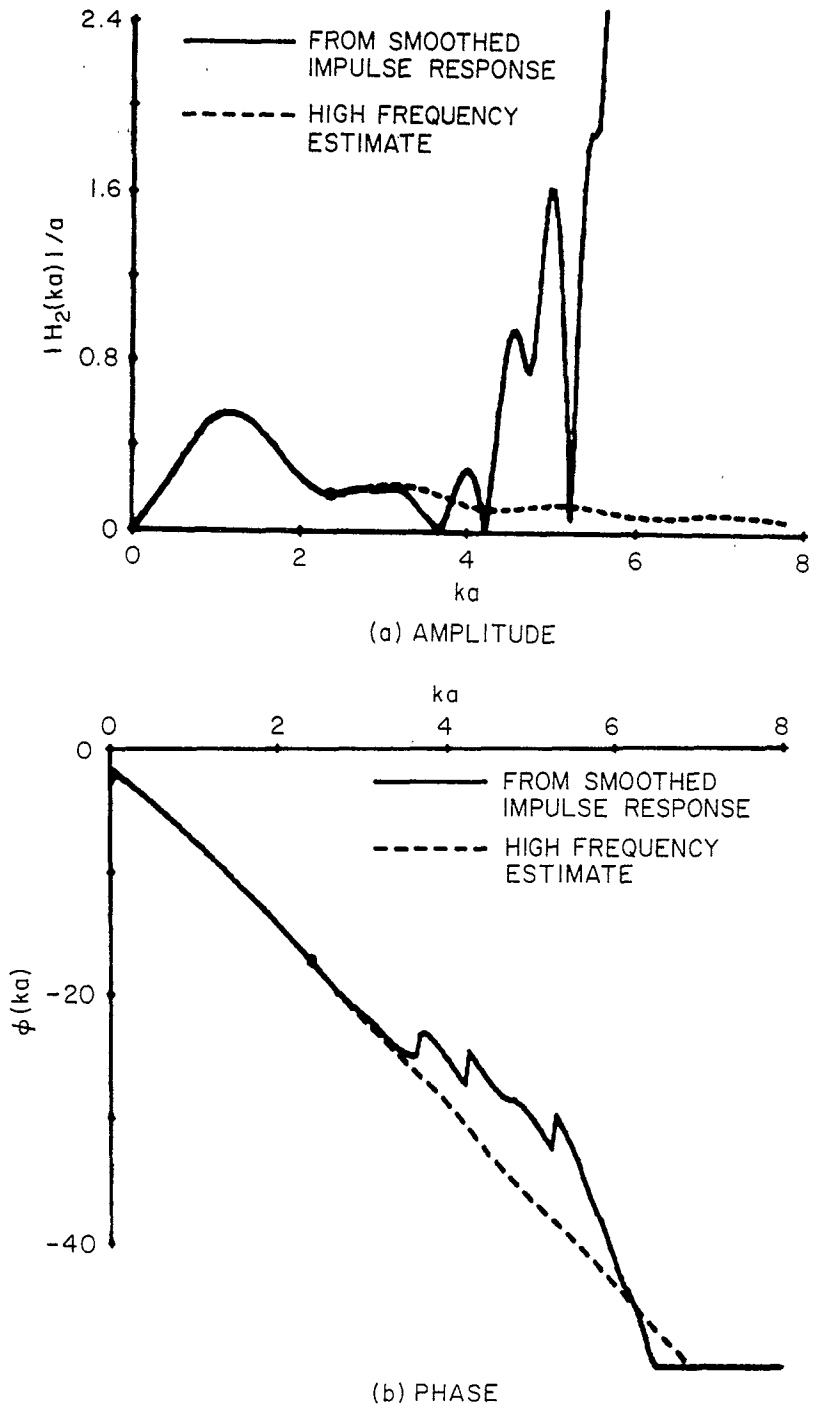

FIG. 23 Augmented frequency response of the second part of the flat-end sphere-cap cylinder at 0^{o} incidence.

b_1 = the coefficient for the creeping wave of the sphere

A_1 & A_2 chosen such that

$$\hat{H}_{a2}(\omega_2) = H_{a2}(\omega_2)$$

$$\hat{H}_{a2}(\omega_3) = 0.210 \quad .$$

Carrying out the above procedures yields the following values for these parameters:

$$\omega_2 = 2.372$$

$$m_1 = -7.289$$

$$b_1 = 0$$

$$\omega_3 = 3.328$$

$$m_2 = -4.000$$

$$b_2 = -4.661$$

$$|H_{a2}(\omega_2)| = 0.173$$

$$|H_{a2}(\omega_3)| = 0.210$$

$$A_1 = 3.656$$

$$B_1 = 2.051$$

$$A_2 = 0.233 \quad .$$

Substituting these values into Eq. (25) yields the estimate of the high frequency portion of the augmented frequency response shown by the broken line in Fig. 23.

The impulse response of the second part of the return from the flat-end sphere-cap cylinder at 0^o incidence is shown in Fig. 24. Note the creeping wave peak at $t/a \approx 7.3$. The return due to the far end appears as a negative swing at $t/a = 4$, as expected. The form of this portion of the return would be expected to be $(t - t_o)^{1/2}$, where t_o is the initial time of the return.

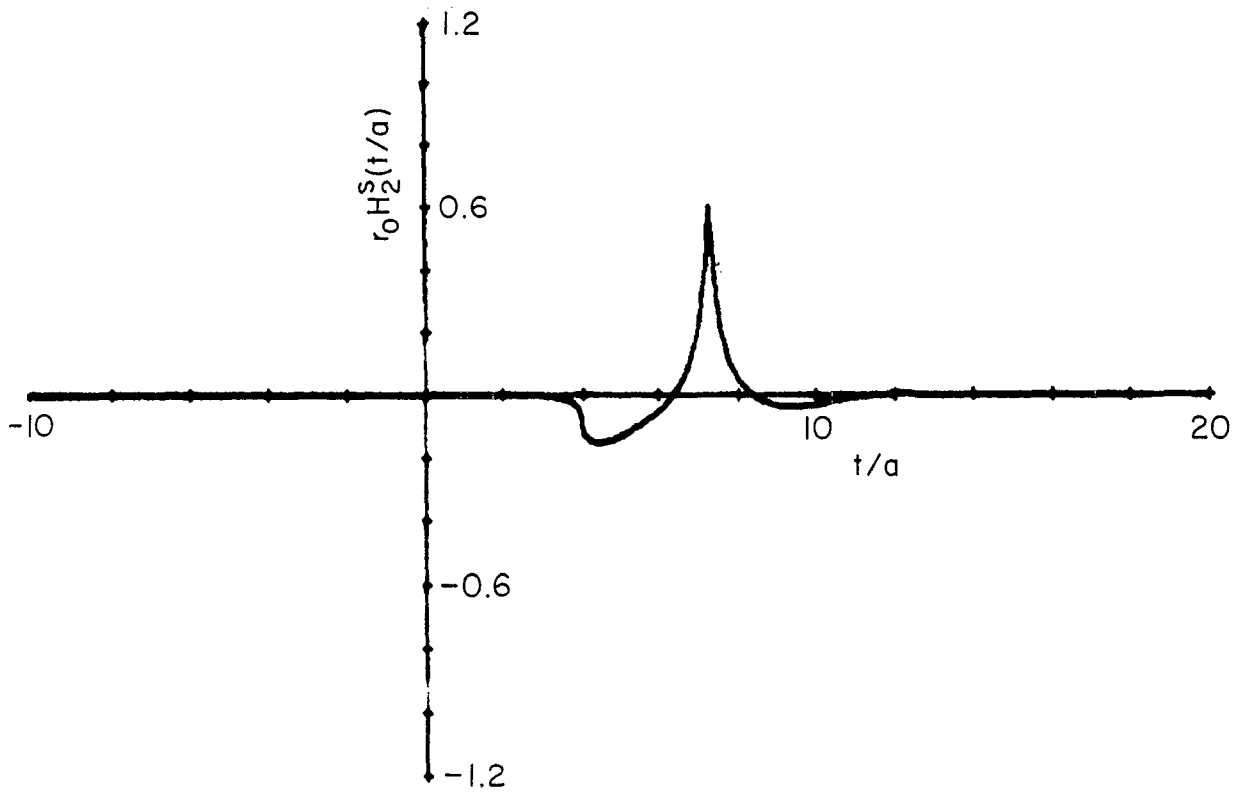

FIG. 24 Impulse response from the second part of the flat-end, sphere-cap cylinder at 0^o incidence.

Finally, the two portions of the impulse response are combined and the resulting total impulse response is displayed in Fig. 25(a). The total frequency response is shown in Fig. 25(b). The fast variation in the frequency response is due to the interference between the return from the front end and the return from the far end. The slight modulation can be attributed to the interference between the creeping wave return and the far edge return. Finally, the presence of the doublet in the impulse response is apparent as a linearly increasing frequency response such that at higher frequencies this effect dominates the response.

2.3.3 Right-Circular Cylinder

This section describes the application of the impulse response augmentation technique to the right-circular cylinder for axial incidence. The target geometry is shown in Fig. 7 with its axis coinciding with the z-axis. This target is centered at the origin and has a length-to-diameter ratio of 2:1. For the smoothed impulse response computation the target was illuminated by the incident plane wave given in Eq. (19) with a width equal to the length of the target.

The smoothed impulse response that was computed by the space-time integral equation as described in Sec. 2.1 is displayed in Fig. 26 for axial incidence. The initial portion of the return approximates a smoothed doublet and is identical to the initial response of the flat-end sphere-cap cylinder at 0° incidence. Again there is negligible return from the sides of the cylinder due to its symmetric nature. The return from the far end of this target can be attributed to both the far edge and to the wave traveling around the backside. It is interesting to note that the portion of the return from the far end is nearly identical to that obtained from the far end of the flat-end sphere-cap cylinder at 180° incidence. This indicates that the currents which are set up on the front end of the target have little effect on the far field response of the return from the far end of the target. Because of the above considerations, it should be obvious that the response from the front end of the cylinder is identical to that already computed for the flat-end sphere-cap cylinder at 0° incidence. The response from the far end is very similar to that already computed for the far end of the flat-end sphere-cap cylinder at 180° incidence.

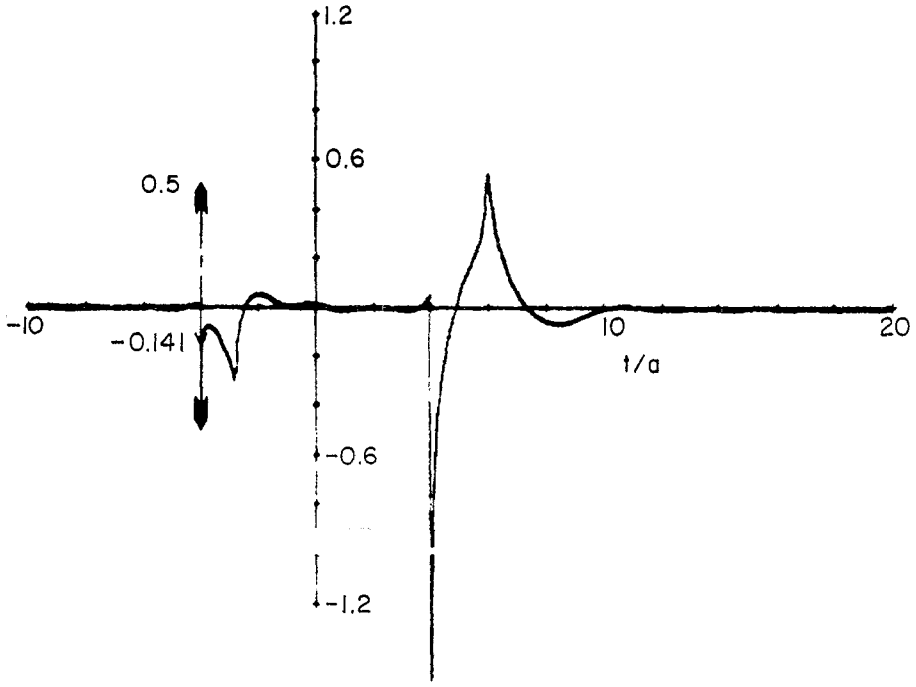

(a) IMPULSE RESPONSE

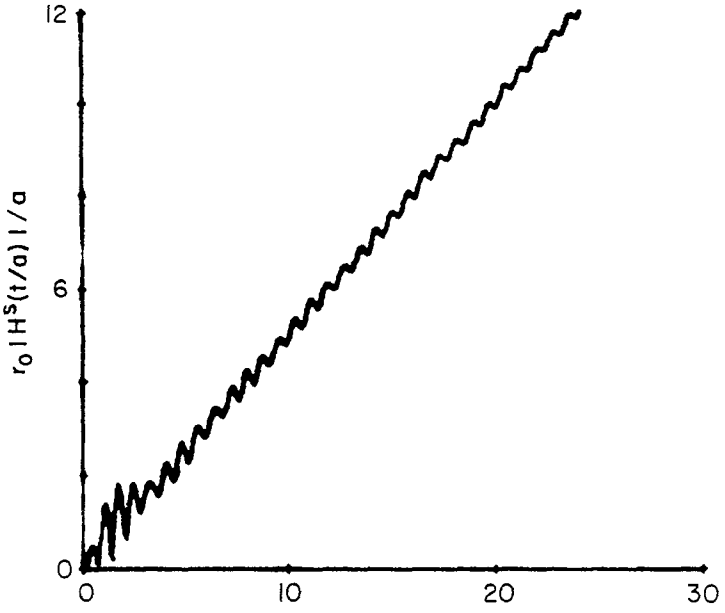

(b) FREQUENCY RESPONSE

FIG. 25 Response of the flat-end sphere-cap cylinder at 0^0 incidence as computed with the impulse response augmentation technique.

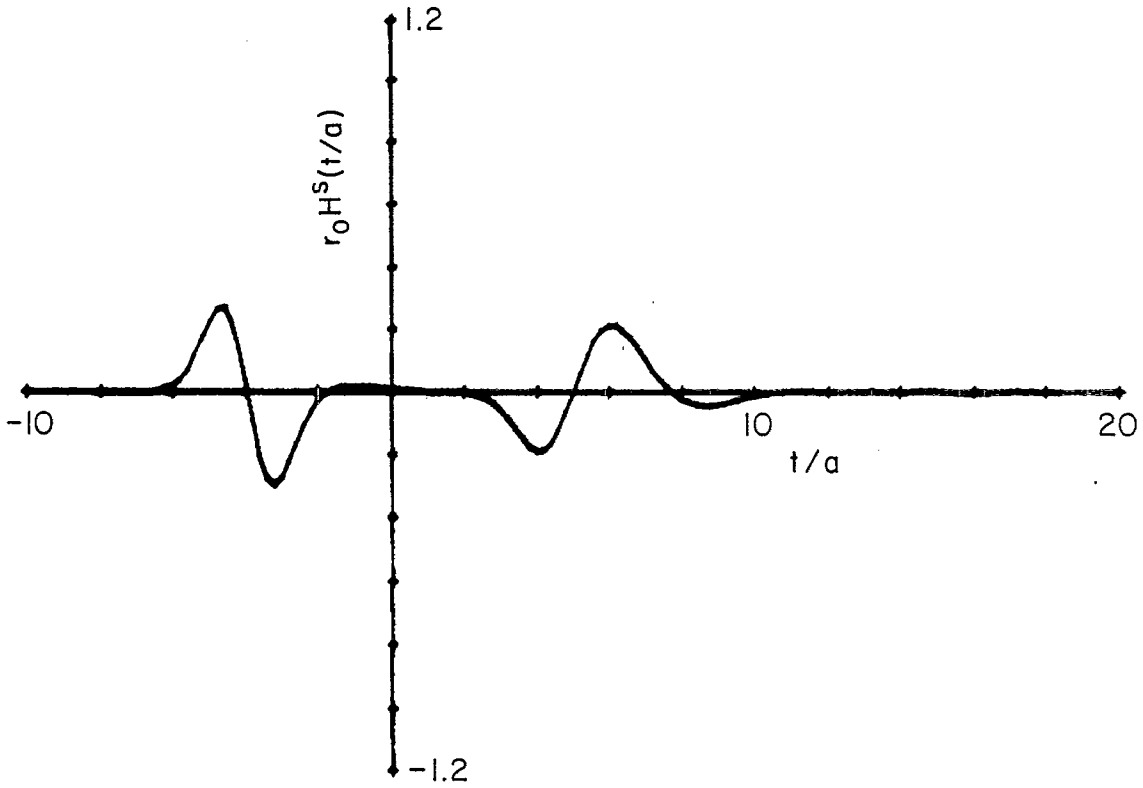

FIG. 26 Smoothed impulse response of a right-circular cylinder with radius a and length 4a at axial incidence.

Shown in Fig. 27 is the frequency response of this target, which was computed by dividing the transform of the smoothed impulse response by the transform of the incident pulse. The frequency response shown here is valid up to approximately $ka = 4$, beyond which the numerical noise increases very rapidly. The ripples that appear in the response before this point are due to interference between the return from the near end and the return from the far end of the cylinder. The linear increase in this response is attributed to the doublet that appears in the leading edge of the impulse response.

For application of the augmentation technique, the response in Fig. 26 was divided into two parts at $t/a = 1.8$. The response for the first part is identical to that given in Sec. 2.3.3 for the front part of the flat-end sphere-cap cylinder at 0^{o} incidence. The results are summarized here for convenience. The augmentation function was given by

$$f_{a1}(t) = D_z \delta^1(t/a - T_z) + P_z \delta(t/a - T_z) + V_z \, v(t/a - T_z) \tag{23}$$

where

$$v(t - T_z) = (t/a - T_z)^{-1/2} \, U(t/a - T_z)$$

$$T_z = -4.000$$

$$D_z = 1/2$$

$$P_z = 0.141$$

$$V_z = -0.035 \quad .$$

The high frequency portion of the augmented frequency response was given by

$$\hat{H}_{a1}(\omega) = U_z \frac{\sqrt{\pi}}{\omega^{3/2}} \exp(j\omega m_o + j b_o) \; ; \quad j\omega > \omega_c \tag{24}$$

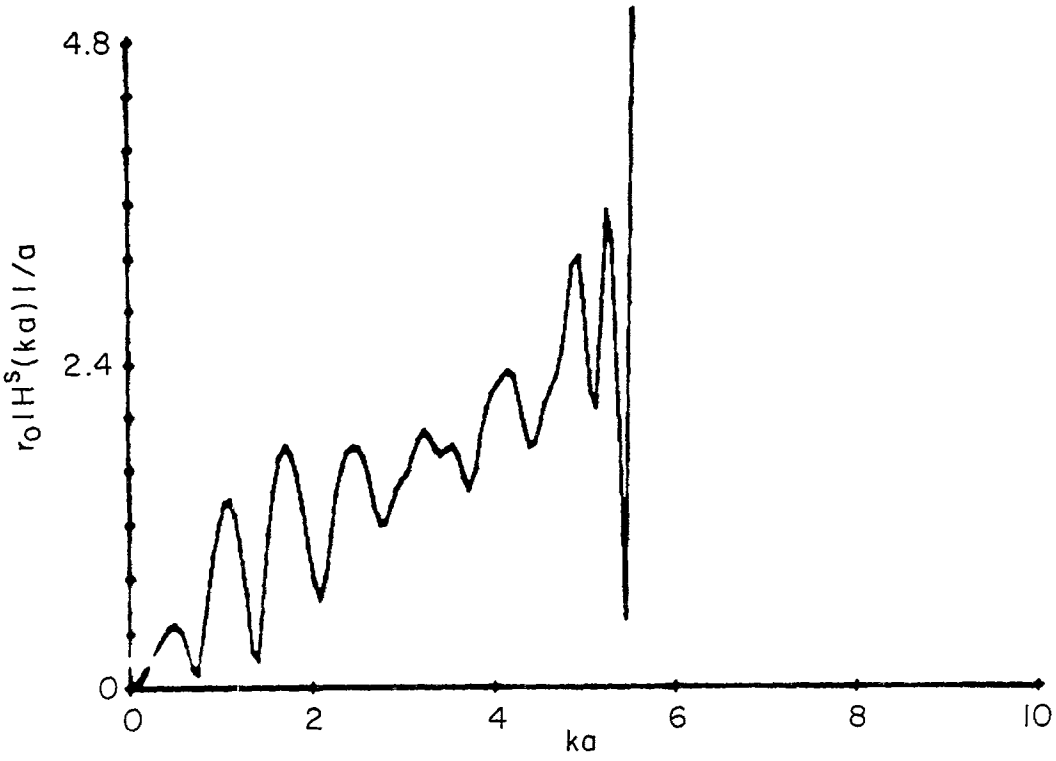

FIG. 27 Frequency response of right-circular cylinder with radius a and length 4a at axial incidence.

where

$$\omega_c = 4.173$$

$$b_o = -3\pi/4$$

$$m_o = 2.753$$

$$U_z = 0.379 \quad .$$

Figure 21 shows the augmented frequency response and Fig. 22 displays the impulse response due to the front part of this target.

The application of the augmentation technique to the second portion of this response is identical to that used for the far end of the flat-end sphere-cap cylinder at 180° incidence, which was described in Sec. 2.3.2. Hence, only the results are summarized here. The augmentation for the far end of this target was taken to be zero. The high frequency estimate of the augmented frequency response is given by

$$\hat{H}_{a2}(\omega) = A_1 \exp(-B_1 \omega^{1/3}) \exp(j\omega m_1 + jb_1) + \frac{A_2}{\omega^{1/2}} \exp(j\omega m_2 + jb_2); \quad \omega > \omega_c \qquad (22)$$

where

$$\omega_1 = 3.313$$

$$m_1 = -6.000$$

$$b_1 = -0.357$$

$$\omega_2 = 4.864$$

$$m_2 = -3.975$$

$$b_2 = -5\pi/4$$

$$|H_{a2}(\omega_1)| = 0.169$$

$$|H_{a2}(\omega_2)| = 0.300$$

$$A_1 = 2.305$$

$$B_1 = 2.051$$

$$A_2 = 0.504 \quad .$$

On comparing these values with those obtained for the flat-end sphere-cap cylinder at 180° incidence, most parameters are nearly the same. However, the amplitude of the creeping wave return seems to be approximately 45 percent larger for the cylinder with the sphere cap.

Finally, the two portions of the impulse response are combined and the resulting total impulse response for the right-circular cylinder is displayed in Fig. 28(a). The total frequency response is shown in Fig. 28(b).

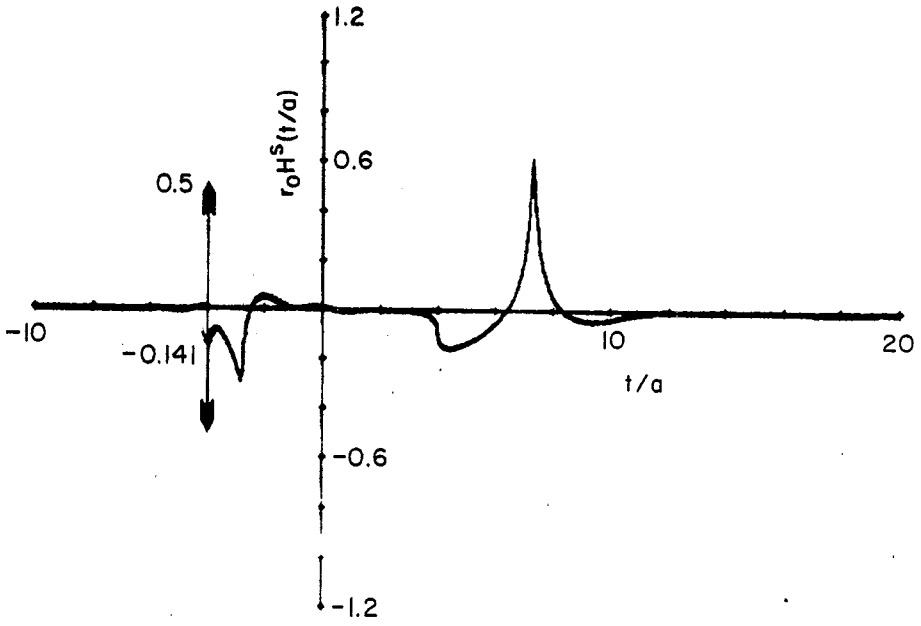

(a) IMPULSE RESPONSE

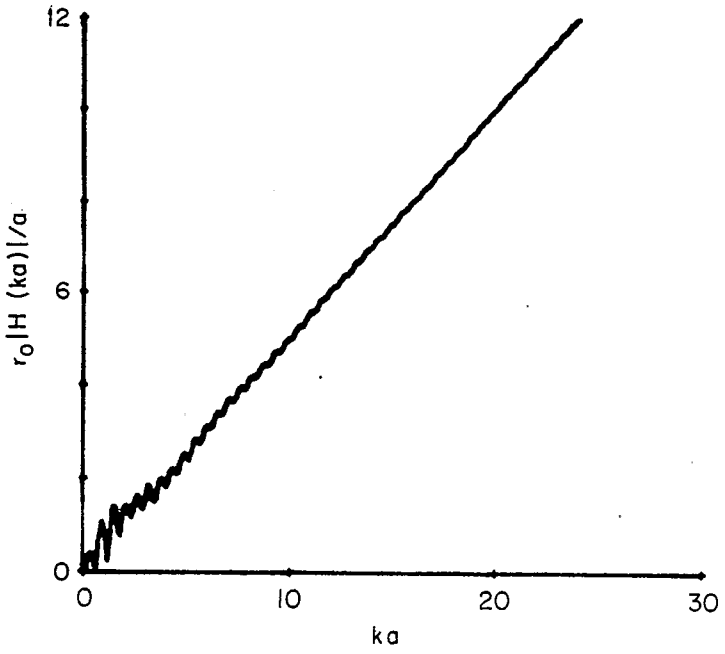

(b) FREQUENCY RESPONSE

FIG. 28 Response of the right-circular cylinder for axial incidence as computed with the impulse response augmentation technique.

SECTION 3
TIME DOMAIN SCATTERING MEASUREMENTS ON OPEN, THIN SURFACES
(C. L. Bennett and D. Peterson)

3.1 DESCRIPTION OF MEASUREMENTS

The functional block diagram of the scattering range is shown in Fig. 29. The system signal source is a high-voltage switch which generates a 300 V step function with a risetime less than 100 ps. The signal is radiated, virtually undistorted, from a wire transmitting antenna protruding through a circular ground plane 20 feet in diameter. This wave illuminates the target and the resulting scattered waveform is received on a coaxial horn antenna, which essentially smoothes and differentiates the signal and thus provides the smoothed impulse response of the target. The received waveform is sampled by a 12 GHz oscilloscope that has been triggered by the initial pulse and whose sampling gate deflection is under the control of a small instrumentation computer. Unprocessed data are displayed on the oscilloscope CRT while the sampled-and-held waveform is passed through a low-pass filter, digitized, read into the computer, and stored on magnetic tape automatically. This system has been designed to correct for long-term timing drift and/or amplifier drift. In addition, the waveforms are stored in such a way that they are ready for the subsequent operations of averaging (to remove short-term noise) and baseline processing. The effects of a time varying baseline are subtracted from measured waveforms to improve system accuracy.

The salient characteristics of the range are the speed and simplicity with which multi-octave frequency-domain data can be obtained. These advantages accrue because the time-domain scattering range yields an "uncontaminated" interval of time between the arrival of the direct wave and the arrival of unwanted reflections. This is most easily explained by considering the sketch in Fig. 30, which shows the relative location of the elements on the ground plane. The transmitted signal travels outward from the base of the wire antenna and is received at R at time $t_o = d/c$ (where c is the speed of light). The outgoing wave reaches the target at $t = r/c$, is reflected, and arrives at the receiver at $t_1 = (2r+d)/c = t_0 + (2r/c)$.

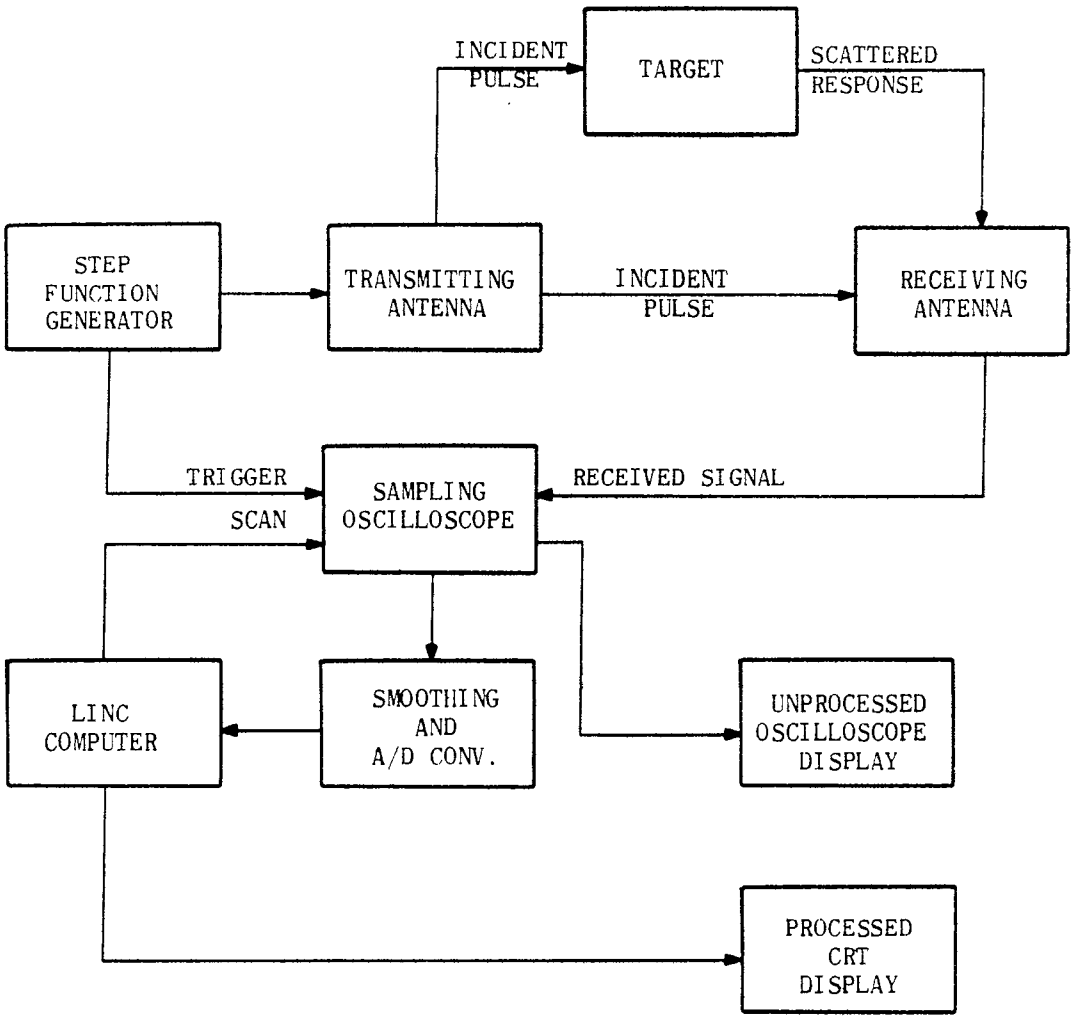

FIG. 29 Functional block diagram of video time domain scattering range.

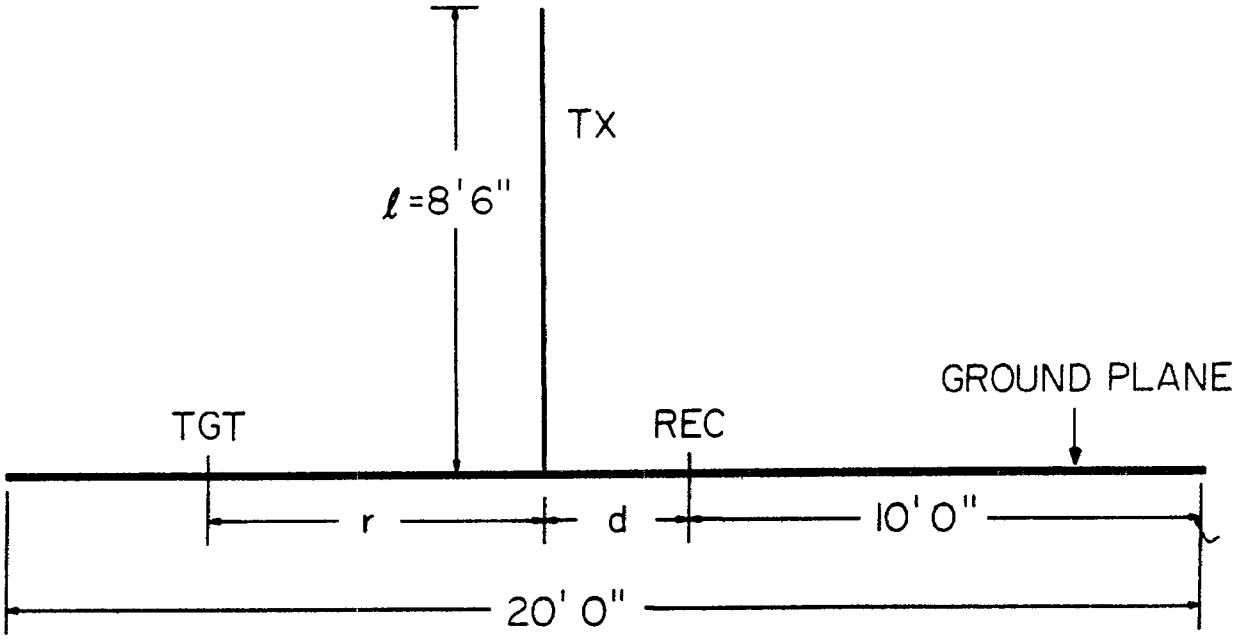

FIG. 30 Geometrical configuration of video time domain scattering range (d=18", r=36").

The targets are usually located anywhere from 2 to 5 feet from the transmitting antenna; therefore, target returns lie in the region that extends from 4 ns to 10 ns after the incident pulse. The response due to reflection from the tip of the antenna and the edge of the ground plane occurs approximately 15 ns after the incident pulse. The "clear window" which exists between 10 ns and 15 ns is required because many of the targets are highly dispersive and their response will extend far beyond the specular reflection. The entire region between the direct transmission and the table edge response forms a convenient time "window" to view the target response and allows one to "gate out" (in time) unwanted reflections. Thus, undistorted transient target responses can be viewed without resorting to elaborate and expensive anechoic chambers. In addition, a single time-domain measurement obviates the requirement for tedious measurement of the amplitude and phase responses at many frequencies.

The accuracy of the measurement system has been estimated for the results presented in this section. The peak of the incident pulse as measured on the sampling oscilloscope is approximately 400 mV, and a typical target response has a peak value in the vicinity of 10 mV. When using the 10 mV scale on the sampling oscilloscope, the standard deviation of the sample mean is estimated to be

$$\sigma_{\bar{v}} = 0.5 \text{ mV}$$

if 16 scans are averaged. Thus, the estimated standard deviation of the sample mean $\bar{v}$ is in the vicinity of 5% of the peak value of the target response.

In addition, the measured responses were further processed by means of a convolution procedure to obtain the response due to a Gaussian shaped incident pulse rather than the approximate smoothed impulse used in the actual measurements. Figure 31 displays the actual measured incident pulse along with the smoothed Gaussian pulse that was used in the convolution process. The frequency spectrum of these two pulses is displayed in Fig. 32. The time domain expression for the Gaussian pulse is given by

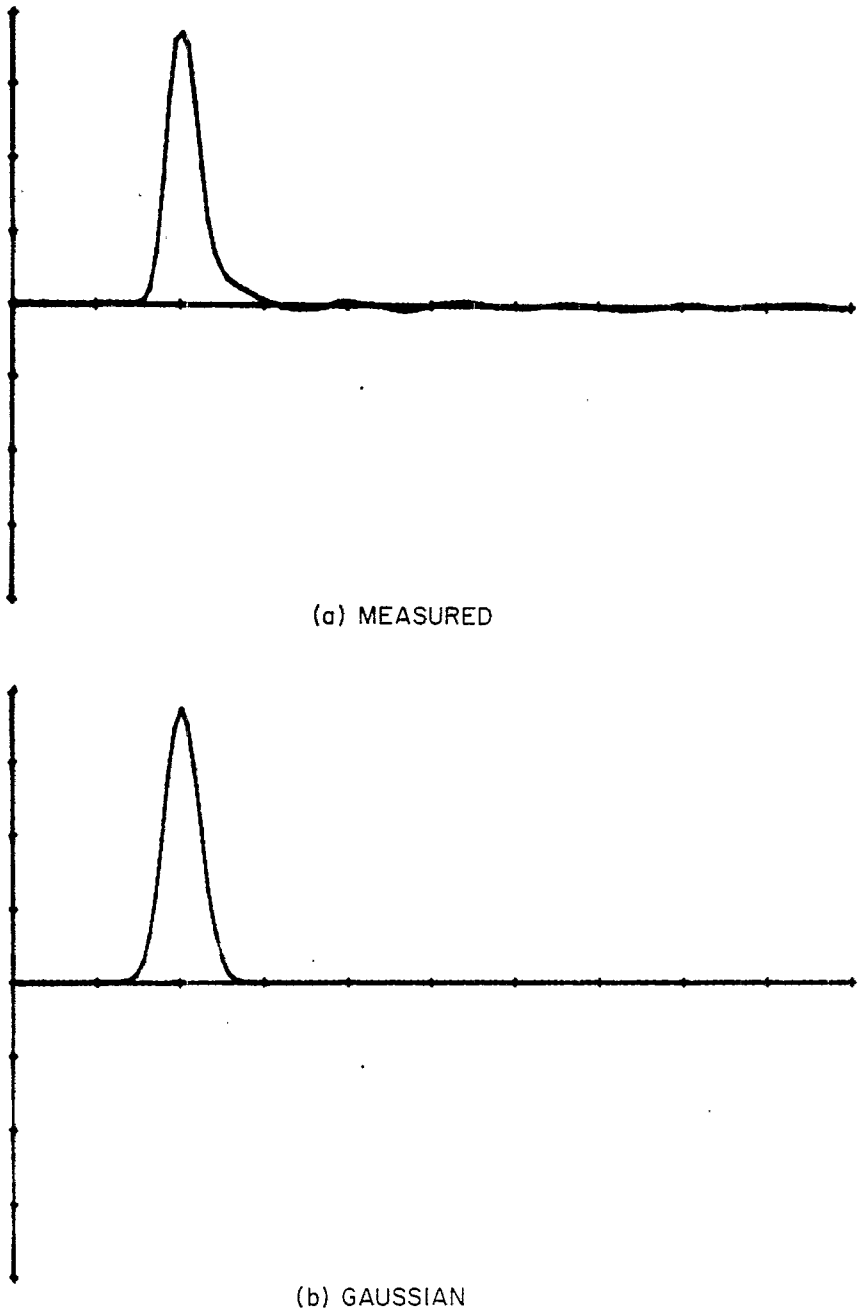

FIG. 31 Incident pulse (horizontal scale: 0.5 ns/div.; vertical scale: 100 mV/div.).

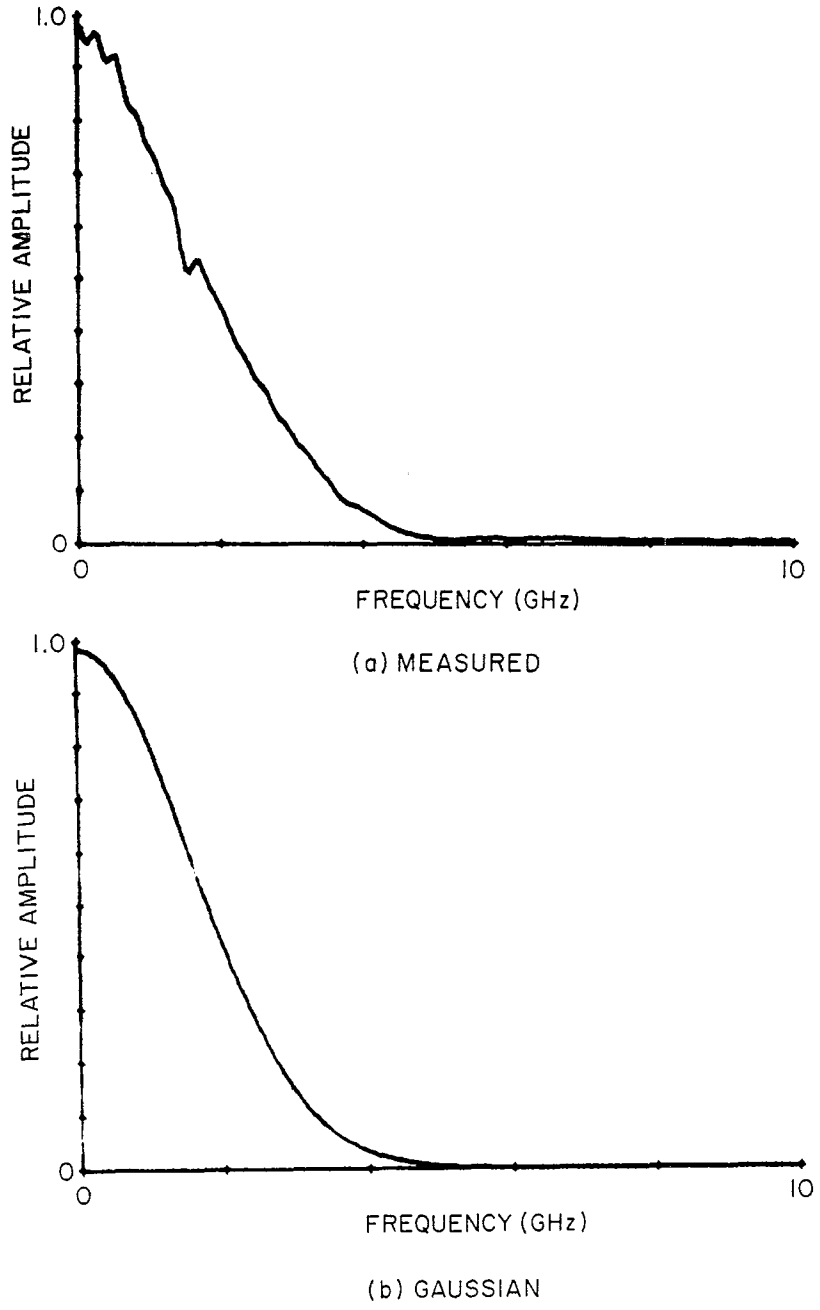

FIG. 32 Spectrum of incident pulse.

$$e(t) = E_o \frac{a_n}{\sqrt{\pi}} \exp\left[-a_n^2 (t - t_o)^2\right]$$

and the frequency domain expression is

$$E(\omega) = E_o \exp\left[-\omega^2/(2a_n)^2\right] \exp(-j\omega t_o) \quad .$$

The amplitude coefficient E_o was set equal to the dc value of the measured incident pulse. The width coefficient a_n was obtained by requiring that the 50% value of $|E(\omega)|$ occur at the same point in frequency as the 50% value of the magnitude of the transformed measured incident pulse. The width of the resulting Gaussian pulse becomes 0.59 ns or approximately 7 inches. An added benefit of this process is the reduction of high frequency noise in the response where no signal is present anyway.

3.2 RESULTS

In previous studies,[3,7] the smoothed impulse response was computed for target geometries that included the sphere, right-circular cylinder, right-square cylinder, sphere-capped cylinder, cube, sphere-cone sphere, UES satellite model and SSS satellite model. Under the present contract, responses were measured for a number of open, thin surfaces. The results of these measurements on seven different targets are summarized in Table 1. The square plate, rectangular plate, circular disc and corner reflector target geometries are displayed in Fig. 33. The circular cylinder section, the parabolic cylinder section, and the parabolic dish target geometries are shown in Fig. 34. The smoothed impulse responses which are displayed in this section are due to the incident smoothed impulse shown in Fig. 31(b), which has a width of 0.59 ns.

In Fig. 35, the smoothed impulse response (in a backscatter direction) over an 8 inch square plate is shown for four angles of incidence. In this case, the image plane is normal to the face and to the edges of this flat plate. For 0^o incidence, the initial return appears as a differentiation of the incident

TABLE 1

Summary of Measured Waveforms

Object Shape Class	Image Plane	Polarization	Aspect Angles	No. of Waveforms
8" × 8" Square Plate	Normal to face & edge	TM	$0^\circ, 30^\circ, 60^\circ, 90^\circ$	4
4" × 8" Rectangular Plate	Normal to 8" face	TM	$0^\circ, 30^\circ, 60^\circ, 90^\circ$	4
	Normal to 4" face	TM	$0^\circ, 30^\circ, 60^\circ, 90^\circ$	4
8" Diameter Circular Disc	Normal to face	TM	$0^\circ, 30^\circ, 60^\circ, 90^\circ$	4
4" × 8" Corner Reflector	Normal to apex	TM	$0^\circ, 30^\circ, 60^\circ, 90^\circ$ $120^\circ, 150^\circ, 180^\circ$	7
	Coincident with apex	TE	$0^\circ, 30^\circ, 60^\circ, 90^\circ$ $120^\circ, 150^\circ, 180^\circ$	7
8" × 8" Circular Cylinder Section $y = \pm \sqrt{2rx - x^2}$, $z = 8"$ $r = 5"$	Normal to axis	TM	$0^\circ, 30^\circ, 60^\circ, 90^\circ$ $120^\circ, 150^\circ, 180^\circ$	7
8" × 8" Parabolic Cylinder Section $y = \sqrt{8x}$ $z = 8"$	Normal to axis	TM	$0^\circ, 30^\circ, 60^\circ, 90^\circ$ $120^\circ, 150^\circ, 180^\circ$	7
8" Parabolic Dish $\sqrt{y^2 + z^2} = \sqrt{8x}$	Normal to face	TM	$0^\circ, 30^\circ, 60^\circ, 90^\circ$ $120^\circ, 150^\circ, 180^\circ$	7

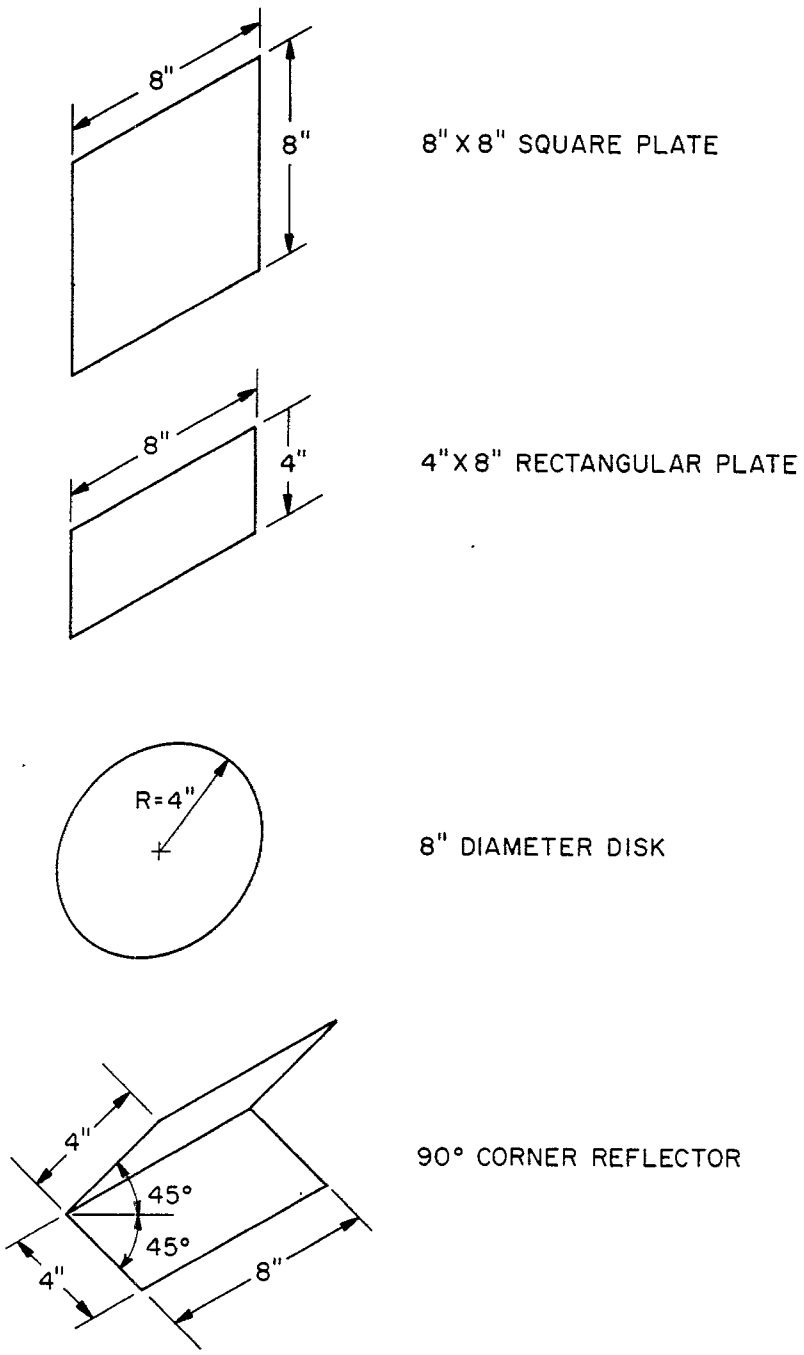

FIG. 33 Target geometry of 8" x 8" square plate, 4" x 8" rectangular plate, 8" diameter disk, and 90^0 corner reflector.

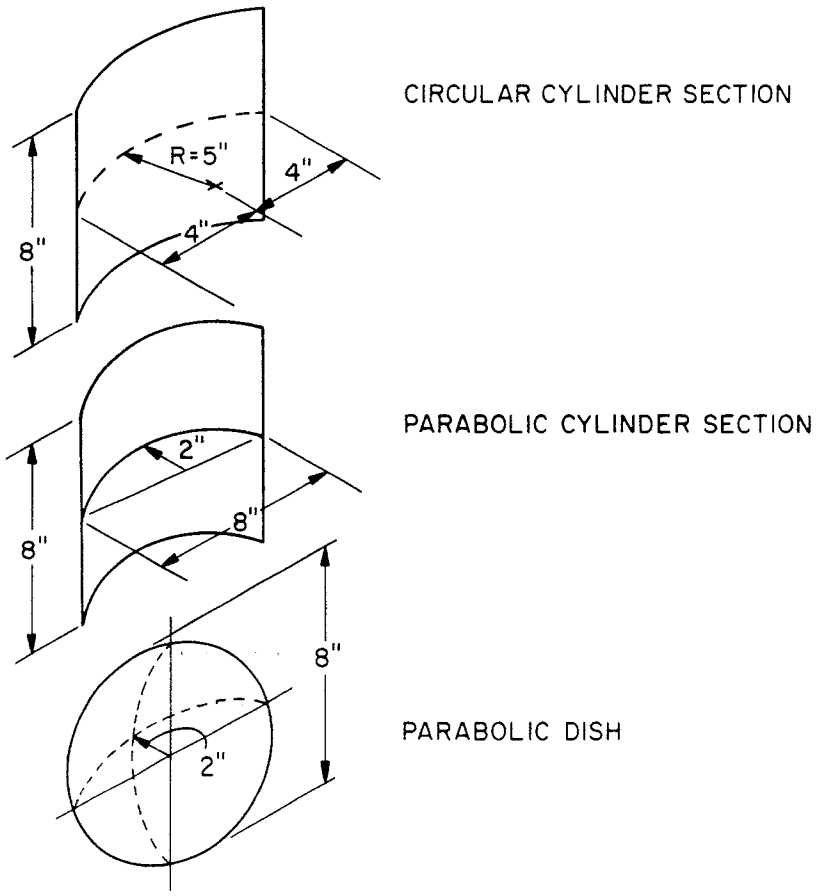

FIG. 34 Target geometry of circular cylinder section, parabolic cylinder section, and parabolic dish.

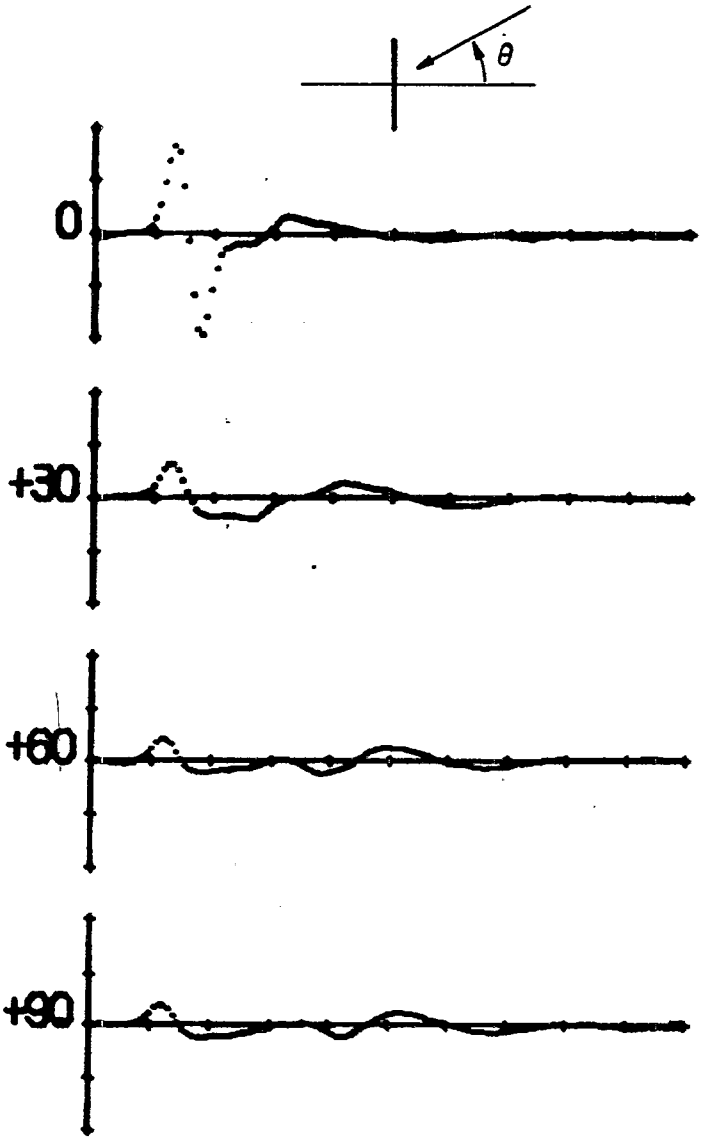

FIG. 35 Smoothed impulse response of an 8 inch-square plate with image plane normal to face and edge for TM polarization (horizontal scale: 0.5 ns/div.; vertical scale: 10 mV/div.).

smoothed impulse. This is followed approximately 0.8 ns later by a positive pulse which represents the effect of the creeping wave on the target. For 30° incidence, we first note a positive pulse from the near edge of the plate. This is followed 0.8 ns later by a direct return from the far edge of the plate. Finally, the return from the creeping wave at the far edge appears at approximately 1.2 ns after the first positive pulse. Moving on to 90°, again a positive pulse is noted from the near edge of the plate. At a time of 1.6 ns later, a negative pulse is noted, which is the return from the far edge of the plate. The second positive pulse is due to traveling waves set up on the plate which decay rapidly with time.

In Fig. 36, the smoothed impulse response of a 4×8 inch plate is shown for the case where the image plane is normal to the face and to the 8 inch edge. This provides the response for the case of TE polarization. For 0° incidence, we again note the initial part of the response represents the derivative of the incident smooth impulse. Again, this is followed by the creeping wave, which appears 0.8 ns later. It is interesting to note that the timing of this creeping wave is the same as it was for the 8 inch square plate. This indicates that the creeping wave is traveling in the 8 inch direction of the plate. It is also interesting to note that the amplitude of the smoothed doublet in this response is approximately one-half the amplitude of the smoothed doublet that was obtained for the 8 inch square plate. For 60° incidence, the first positive pulse represents a return from the near edge. This is followed by a negative pulse approximately 0.7 ns later, which can be attributed to the return from the far edge of the plate. The second positive pulse is due to the traveling waves which were set up in the long dimension of the plate. At 90° incidence, the initial positive pulse is due to the return from the near edge of the plate. At approximately 0.8 ns later, a very small negative pulse can be noted which is attributed to the return from the far edge of the plate. The second positive pulse again is due to the traveling wave which is set up on the plate and which decays very rapidly.

Figure 37 displays the smoothed impulse response of the 4×8 inch rectangular plate where the image plane is normal to the face and to the short edge of the plate. These responses represent the case of TE polarization for the incident wave. At 0° incidence, the differentiation of the incident

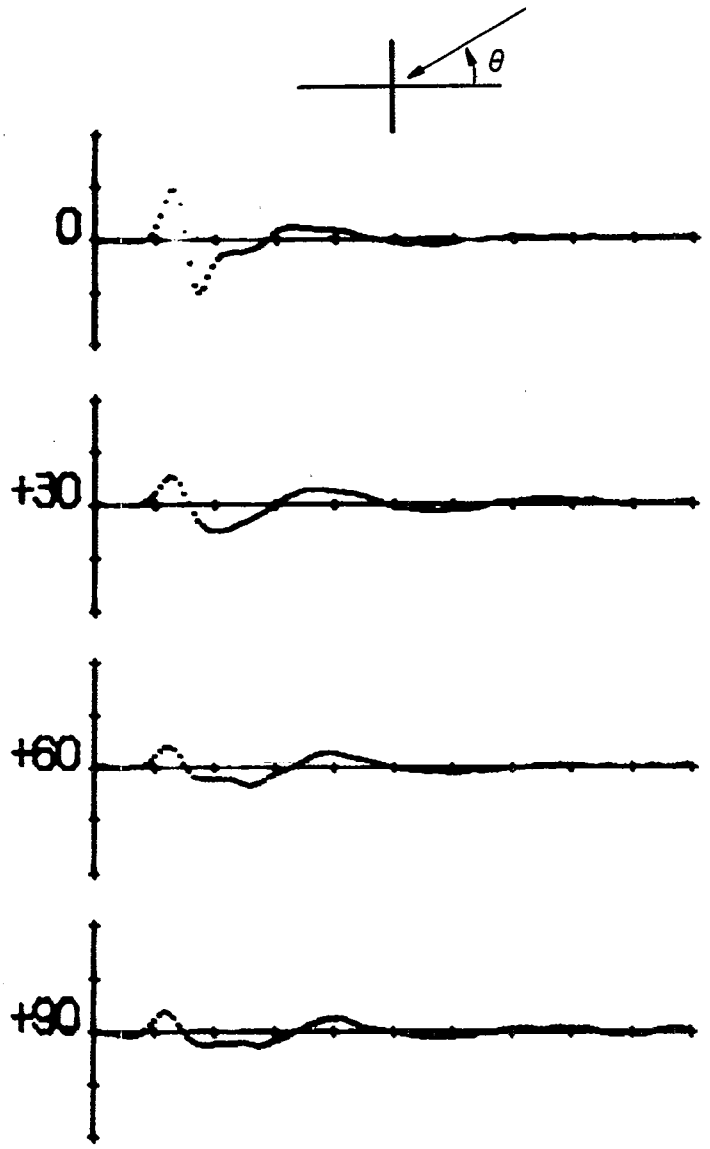

FIG. 36 Smoothed impulse response of 4 x 8 inch rectangular plate with image plane normal to face and 8-inch edge for TM polarization (horizontal scale: 0.5 ns/div.; vertical scale: 10 mV/div.).

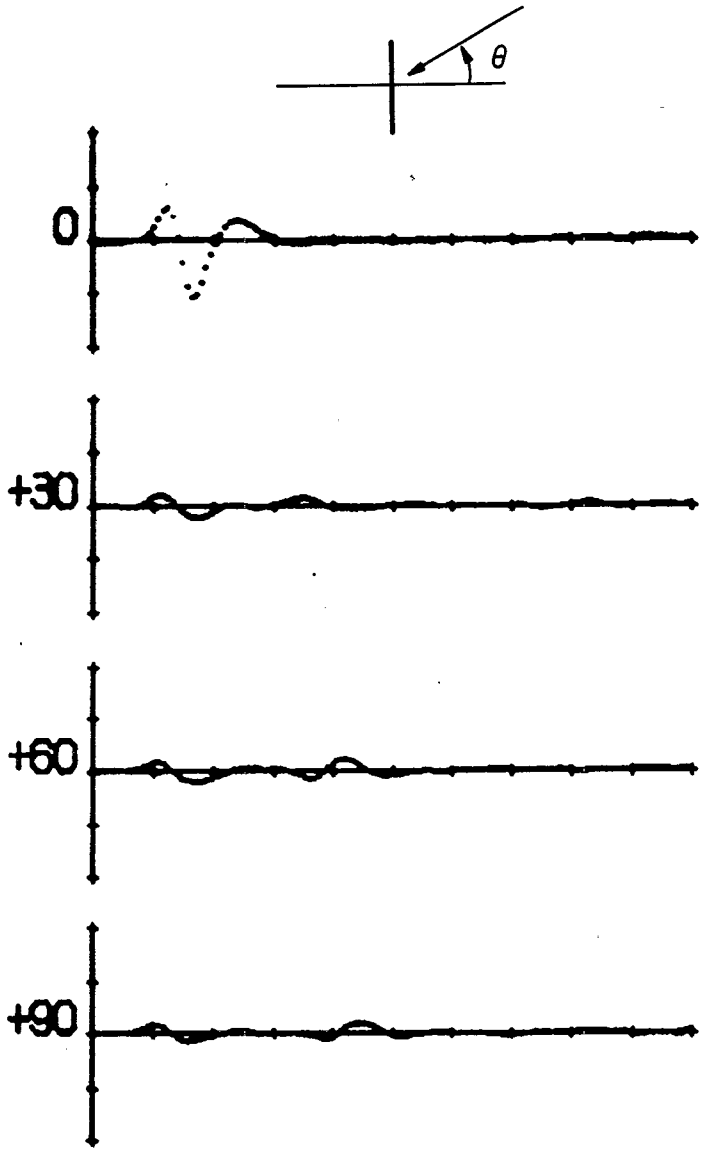

FIG. 37 Smoothed impulse response of 4 × 8 inch rectangular plate with image plane normal to face and 4-inch edge for TM polarization (horizontal scale: 0.5 ns/div.; vertical scale: 10 mV/div.).

pulse again appears as a smoothed doublet. For this case, the creeping wave return appears approximately 0.4 ns after the zero crossing of the smoothed doublet. This is because the creeping wave now travels along the short dimension of the rectangular plate. At 90° incidence, the first positive pulse is due to the return from the near edge of this plate. We note that its amplitude is down substantially from what it was in Fig. 36 for the TM case. This is due to the fact that the polarization is now parallel to the short side of this plate, and the actual length of the scatterer which the incident wave sees is only 4 inches. This positive pulse is followed by a negative swing which represents the traveling wave that is set up on the plate and which decays very rapidly in this case. At approximately 1.6 ns after the first positive peak, a second positive peak occurs which can be attributed to the return from the far edge of this rectangular plate.

In Fig. 38 the smoothed impulse response of an 8 inch diameter disc with image plane normal to the face is shown for various angles of incidence. For 0° incidence, the first portion of the return again appears as a smoothed doublet. This is followed approximately 0.8 ns later by a positive pulse which represents the creeping wave that travels around this target. At the remaining three angles of incidence, the first positive pulse is due to the return from the near edge of the disc. This is followed by a negative swing as the currents decay near this leading edge. The second positive pulse that appears in the three remaining angles of incidence moves further away from the first pulse as the angle increases. This is due to the fact that the distance which the creeping wave, or traveling wave, on the surface has to travel increases as the angle of the incidence increases. At 30°, the pulse appears approximately 1.2 ns after the first pulse. At 60°, the second pulse appears approximately 1.4 ns after the first pulse. And finally, at 90° the second pulse appears approximately 1.6 ns after the first pulse.

In Fig. 39, the smoothed impulse response of a two-dimension corner reflector with the image plane normal to the apex of the corner reflector is shown for various angles of incidence. The axis length on this corner reflector is 8 inches and the width of each plate is 4 inches. These responses are for the case of TM polarization, i.e., the incident $\vec{E}$-field parallel

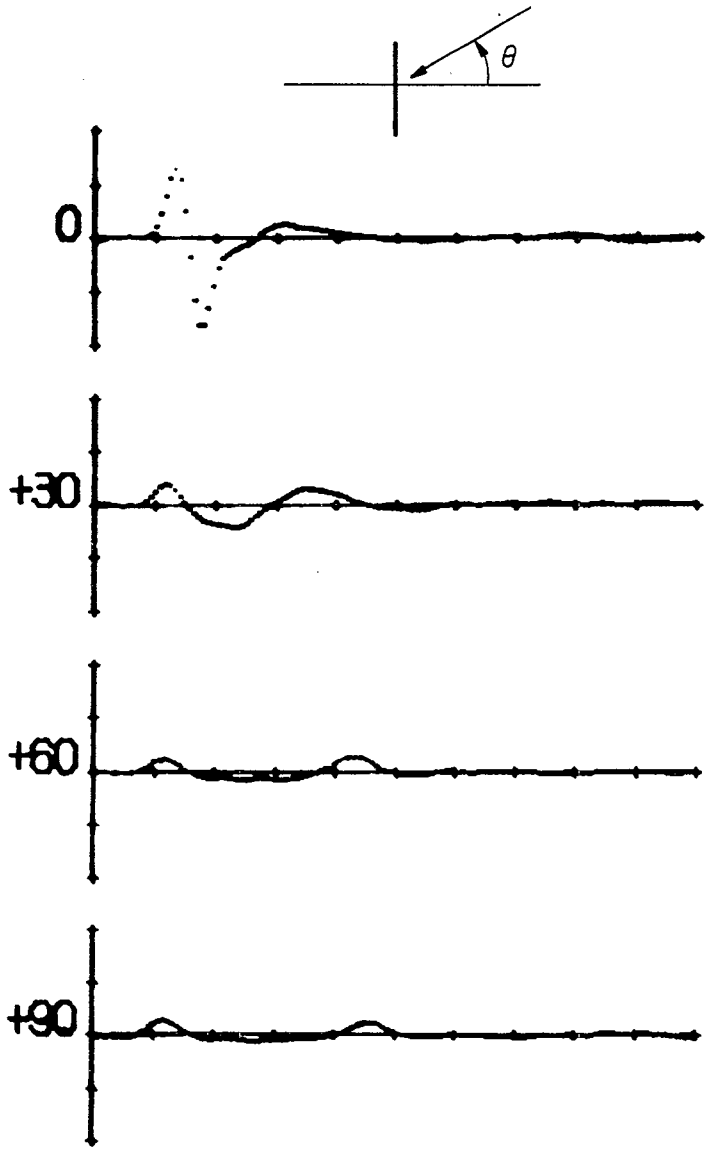

FIG. 38 Smoothed impulse response of 8-inch diameter disc with image plane normal to face and for TM polarization (horizontal scale: 0.5 ns/div.; vertical scale: 10 mV/div.).

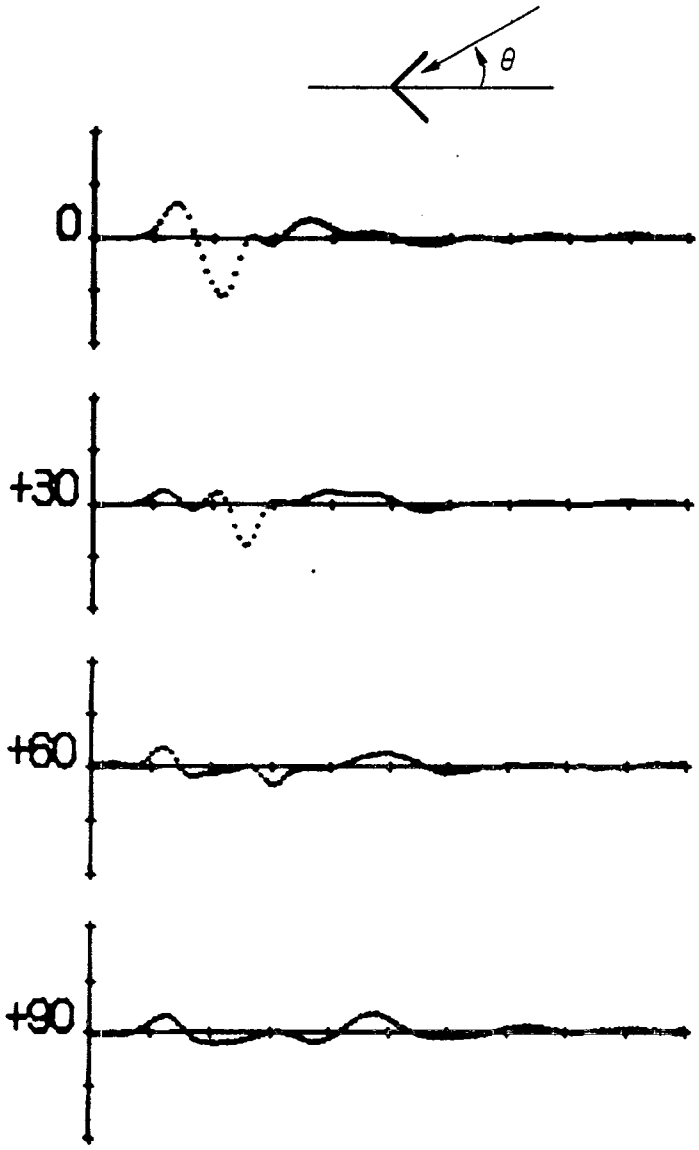

FIG. 39 Smoothed impulse response of 4 x 8 inch corner reflector with image plane normal to apex for TM polarization (horizontal scale: 0.5 ns/div.; vertical scale: 10 mV/div.).

to the axis of the corner reflector. The initial return at 0° incidence does appear to approximate a smoothed doublet as the first order of theory would predict. However, there is obvious smearing of the smoothed doublet present. For example, if one compares the width of this smoothed doublet in Fig. 39 with the width of the smoothed doublet that appears in Fig. 38 for 0° incidence on the disc, then one sees the impact of this smearing. The second positive pulse for this angle of incidence again can be attributed to a wave which travels around the rear of the corner reflector. This positive pulse appears approximately 0.8 ns after the zero crossing of the smooth doublet. As the angle of incidence increases from 0° to 90°, the returns from the near plate of the corner reflector and the far plate of the corner reflector become more separated. At 90° incidence, the first pulse can be attributed to the near edge of the near plate. The negative pulse which appears approximately 1.2 ns after this first positive pulse can be attributed to the far edge of the far plate. This is followed by a second positive pulse which can be attributed to a wave that travels around the back of the corner reflector.

In Fig. 40 the smoothed impulse response of the corner reflector for the case of TM polarization is shown for angles of incidence from the back side of this target. As the angle of incidence increases from 90° to 120° and then to 150°, the initial portion of the smoothed impulse return appears to approximate a smoothed doublet, especially at 120° and 150°. This is to be expected because the angle of incidence is becoming nearly normal to one side of the rear plate. At 180°, the first positive pulse is due to the return from the apex. The return from the far edges of the sides appears approximately 0.6 ns later as a negative pulse. For this angle of incidence, the wave which travels around the rear of the target becomes smeared.

In Fig. 41, the smoothed impulse response of the corner reflector is shown for the case where the image plane is coincident with the apex and symmetric with the target. These responses are shown for the case of TE polarization where the $\vec{E}$-field is perpendicular to the apex of the corner reflector. It is interesting to note here for 0° incidence the vast difference of this response from that obtained from the TM polarization which is shown in Fig. 39. Here, at 0° incidence no apparent smoothed doublet occurs in the

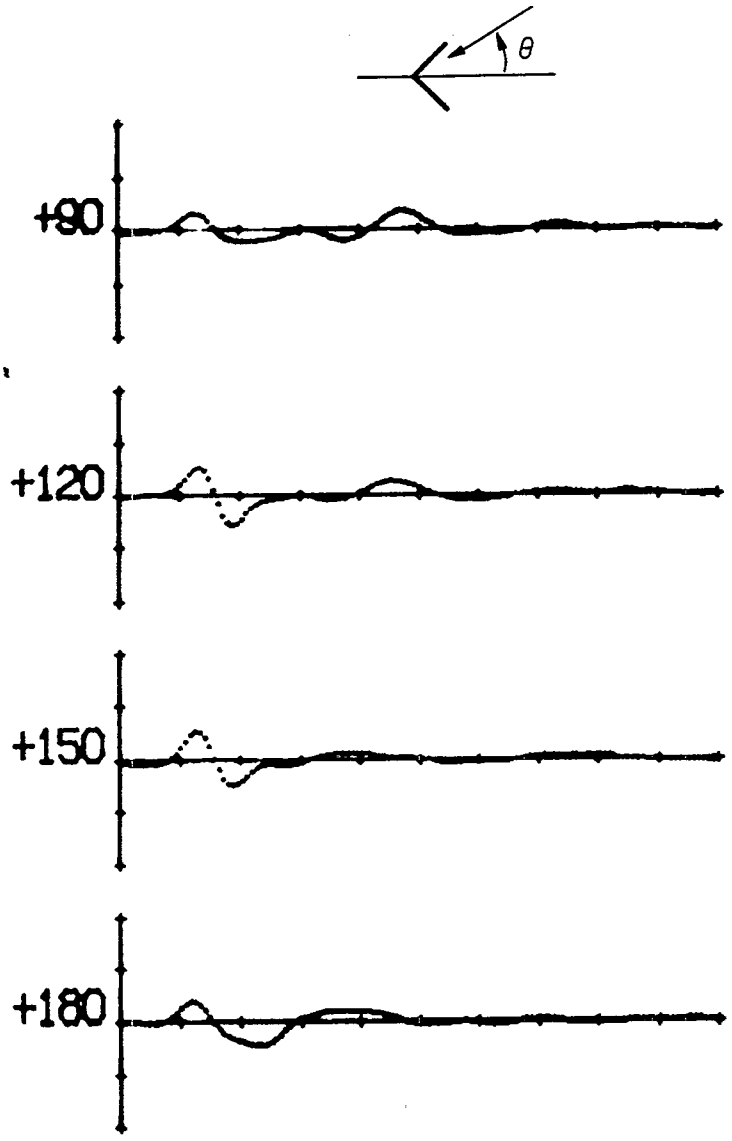

FIG. 40 Smoothed impulse response of 4 x 8 inch corner reflector with image plane normal to apex for TM polarization (horizontal scale: 0.5 ns/div.; vertical scale: 10 mV/div.).

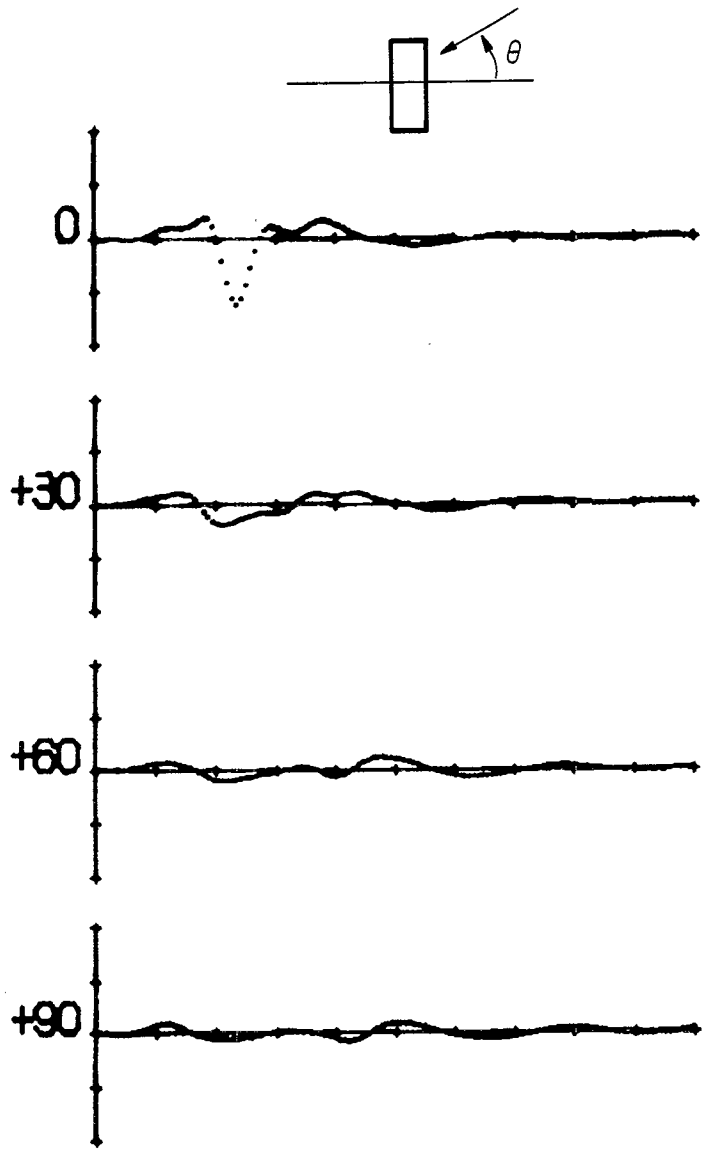

FIG. 41 Smoothed impulse response of 4 x 8 inch corner reflector with image plane coincident with apex for TE polarization (horizontal scale: 0.5 ns/div.; vertical scale: 10 mV/div.).

response and the initial part of the return is at a much lower level for this case. Apparently the scattering from the sides of the corner reflector when the $\vec{E}$-field is perpendicular to the edge is substantially less than it is when the $\vec{E}$-field is parallel to the edge. However, the return from the apex appears to be slightly larger than it was for the TM case. The creeping wave again appears at approximately the same time and is approximately the same magnitude as it is for the TM case. As the angle of incidence increases, the scattered waveform becomes more complicated. The effect of the near edge of the near plate becomes apparent, the effect of the far edge of the far plate becomes apparent, and also the creeping wave is still present. For example, at 90° the first positive peak is from the near edge of the near plate, the second negative peak is due to the far edge of the far plate, and the second positive peak is due to the creeping wave which travels around the target.

In Fig. 42, the smoothed impulse response is shown for the corner reflector with TE polarization when the angle of incidence is from the back side. In comparing the response for this polarization with that obtained for the TM polarization, at angles of incidence of 120° and 150° the apparent smoothed doublet nature of the response does not appear. At 180° incidence, the first positive pulse is attributed to the return from the apex. This is followed by a negative pulse which is attributed to the return from the far edge. Subsequently, a second positive pulse can be attributed to a wave which travels around the rear of the target. Note that there is less smearing of this creeping wave for the TE case than occurred for the TM case shown in Fig. 40. This is probably due to the different path that the creeping wave travels in the two polarizations.

In Fig. 43, the smoothed impulse response of a circular cylinder section is shown for the case where the image plane is normal to the axis of the cylinder. This target is the section of a cylinder with a radius of 5 inches and a height of 8 inches. The distance across the open face is also 8 inches for this target. For 0° incidence, the initial part of the return appears to be a rather smeared smoothed doublet. Note that the amplitude of the negative swing of this is probably 50% larger than the amplitude of the positive swing. This initial part of the return is followed by a varying

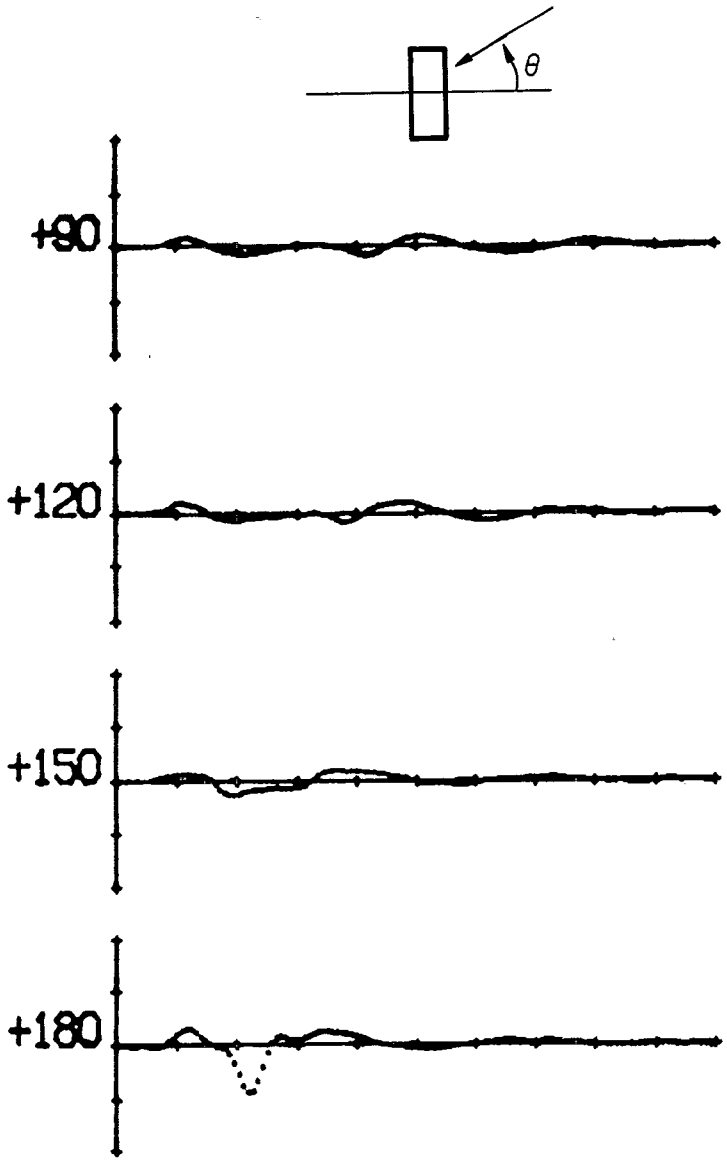

FIG. 42 Smoothed impulse response of 4 x 8 inch corner reflector with image plane coincident with apex for TE polarization (horizontal scale: 0.5 ns/div.; vertical scale: 10 mV/div.).

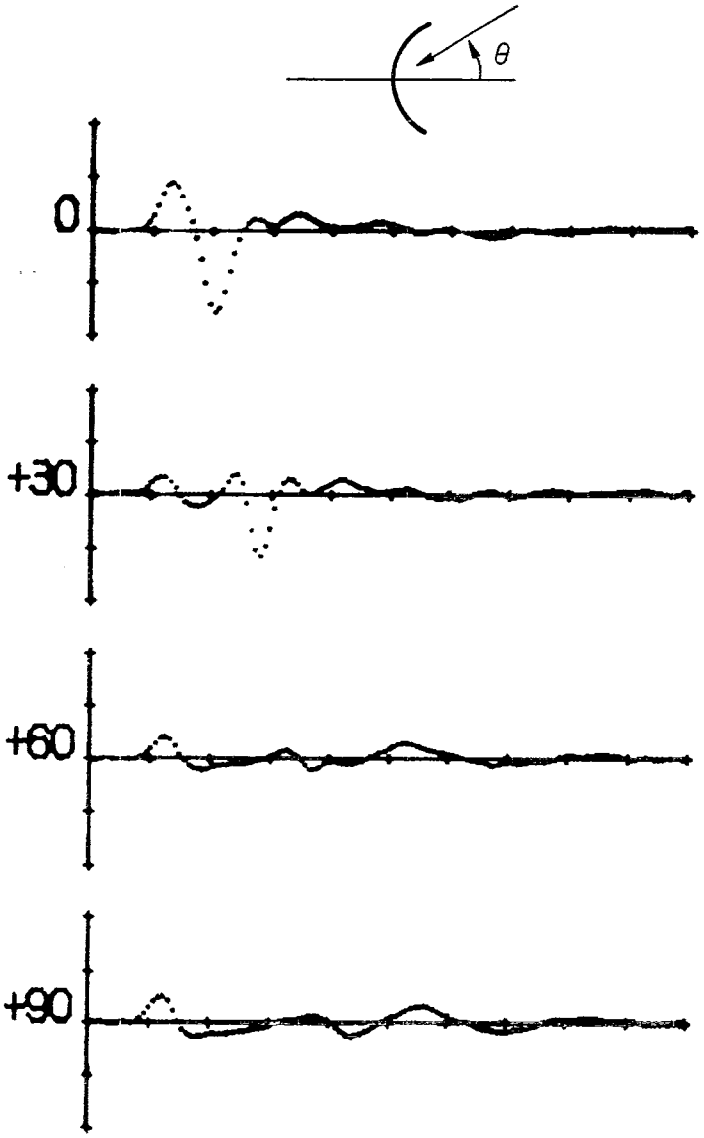

FIG. 43 Smoothed impulse response of circular cylinder section for image plane normal to cylinder axis for TM polarization (horizontal scale: 0.5 ns/div.; vertical scale: 10 mV/div.).

waveform that is due to waves traveling across the face of the cylinder and waves traveling around the rear of the cylinder. As the angle of incidence increases, the structure of the smoothed impulse response becomes more complicated. However, at 90° it is not difficult to relate the portions of the smoothed impulse response to the geometry of the target. The initial positive impulse for this angle of incidence is due to the near edge of this cylinder section. The negative pulse that follows approximately 1.6 ns later can be attributed to a return due to the far edge of this target. The second positive pulse which occurs at approximately 2.1 ns later can be attributed to a wave which travels around the rear of the target.

In Fig. 44, the smoothed impulse response is displayed for angles of incidence on this target that vary between 90° and 180°. Note that at 180° incidence the positive pulse which first appears is due to the specular return from the nose of the back side of the target. The negative swing that follows would be predicted by the physical optics approximation. The second negative pulse, which occurs approximately 0.4 ns after the first positive pulse, can be attributed to a return from the far edge of this target. The second positive pulse which appears approximately 1.1 ns later can be attributed to the creeping wave. Following this is some oscillation which apparently takes place on the concave side of this target.

In Fig. 45, the smoothed impulse response of a parabolic cylinder section is shown for the case where the image plane is normal to the axis of the cylinder and symmetric about the target. This target is a section of a parabolic cylinder. The height of the section is 8 inches, the width across the face is 8 inches, and the depth is 2 inches. This target is very similar in geometry to that of the circular cylinder section whose response is shown in Figs. 43 and 44. As a matter of fact, only minor differences can be discerned between the responses shown in Fig. 45 with a parabolic cylinder section for aspect angles of 0° to 90° and the response shown in Fig. 43 for the circular cylinder section.

Figure 46 displays the smoothed impulse response for this parabolic section for aspect angles of 90° through 180° at 30° increments. Again, the

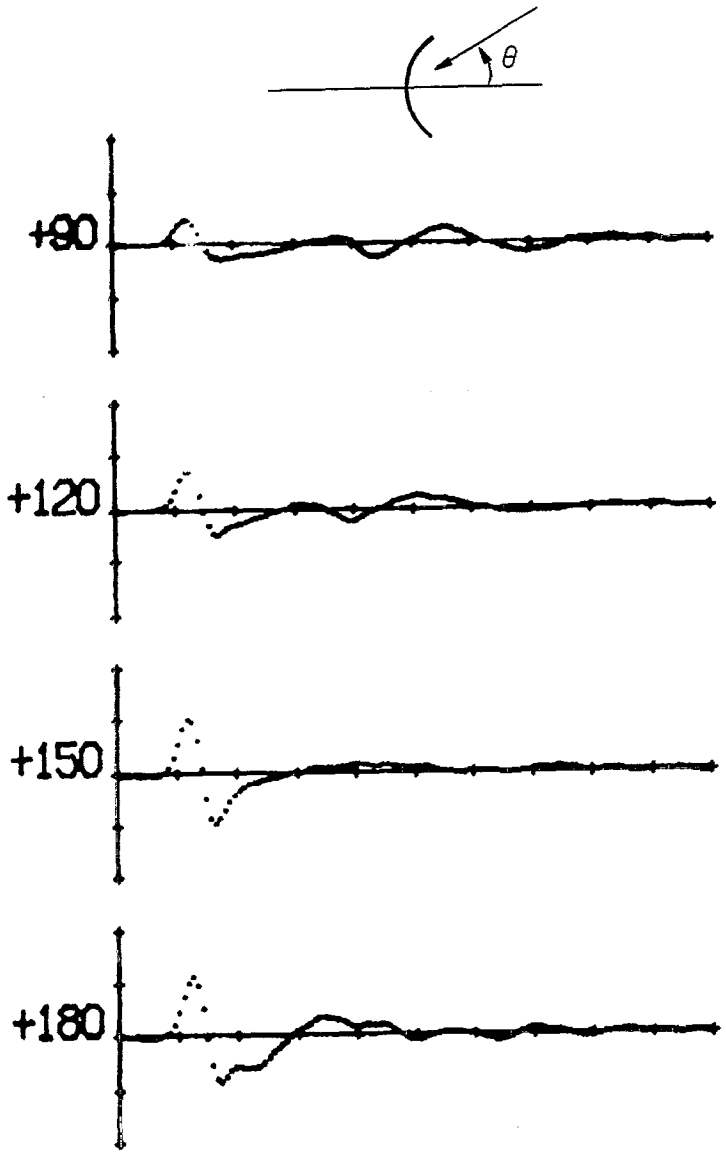

FIG. 44 Smoothed impulse response of circular cylinder section for image plane normal to cylinder axis for TM polarization (horizontal scale: 0.5 ns/div.; vertical scale: 10 mV/div.).

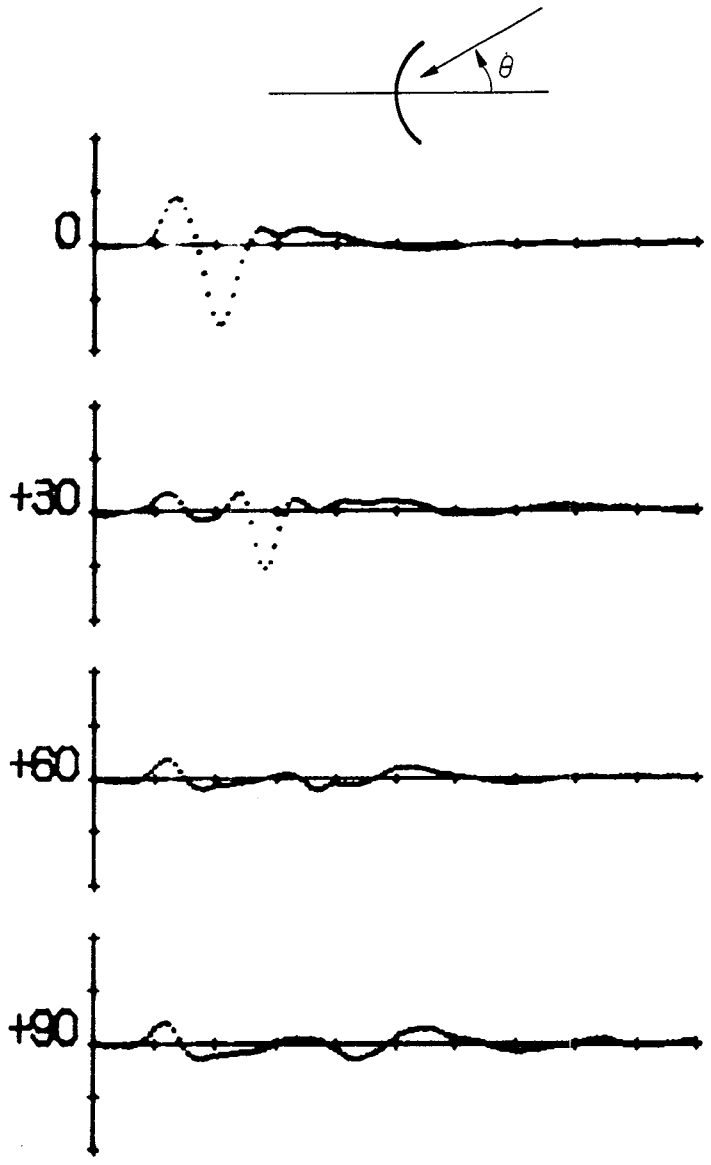

FIG. 45 Smoothed impulse response of parabolic cylinder section with image plane normal to cylinder axis for TM polarization (horizontal scale: 0.5 ns/div.; vertical scale: 5 mV/div.).

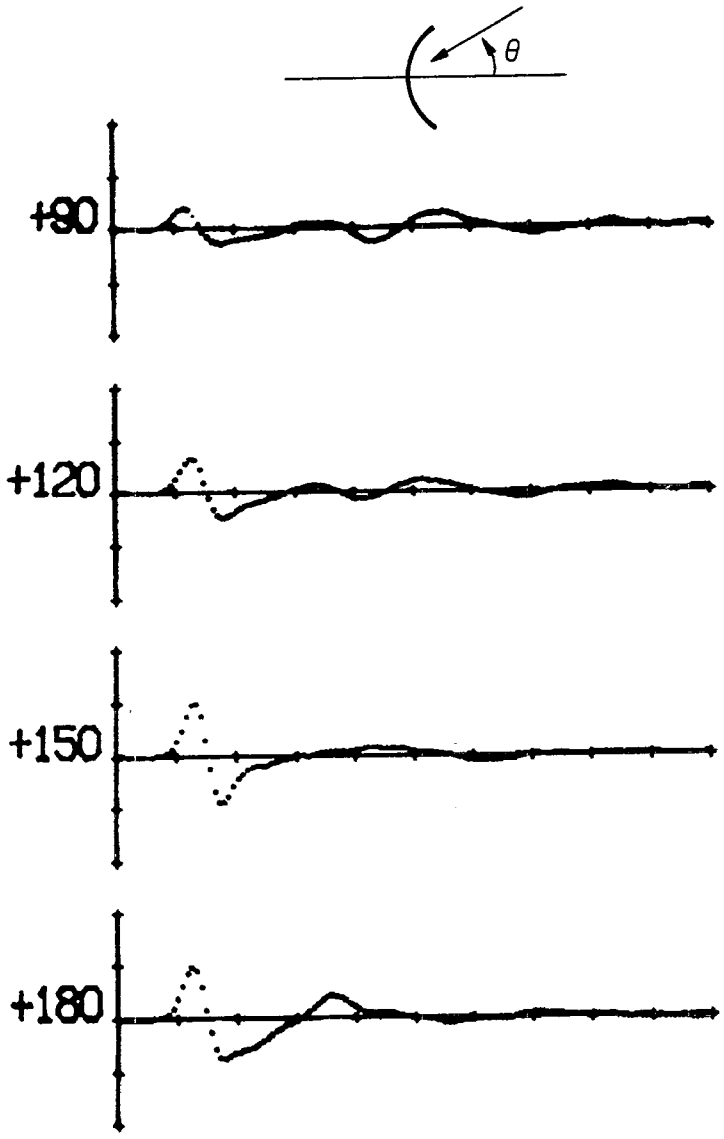

FIG. 46 Smoothed impulse response of parabolic cylinder section with image plane normal to cylinder axis for TM polarization (horizontal scale: 0.5 ns/div.; vertical scale: 5 mV/div.).

response of this target is very similar to that of the circular cylinder section shown in Fig. 44. In fact, only at an aspect angle of 180° can one see a noticeable difference in the two responses. For the parabolic section, the effect of the edge is less apparent than it is in the circular section.

In Figs. 47 and 48 the smoothed impulse response for a parabolic dish is shown for the case where the image plane is perpendicular to the face of the dish and symmetric about the dish. This target is a parabolic dish whose face is 8 inches across and whose depth is 2 inches. For an aspect angle of 0°, the smoothed impulse response is similar to that obtained for the parabolic section. However, as the aspect angle increases, more apparent differences in the two responses become obvious. For example, at 90° the parabolic dish now looks more like the 8 inch diameter disc shown in Fig. 38, where one can see the return from the near edge of the disc and also the return from the far edge of the disc. As the aspect angle increases from 90° to 180°, the creeping wave moves in closer in time to the initial pulse. In particular, at 180° the creeping wave appears approximately 1.0 ns after the initial pulse, which corresponds to the time that it would take a wave traveling the geometric distance around the rear of this target.

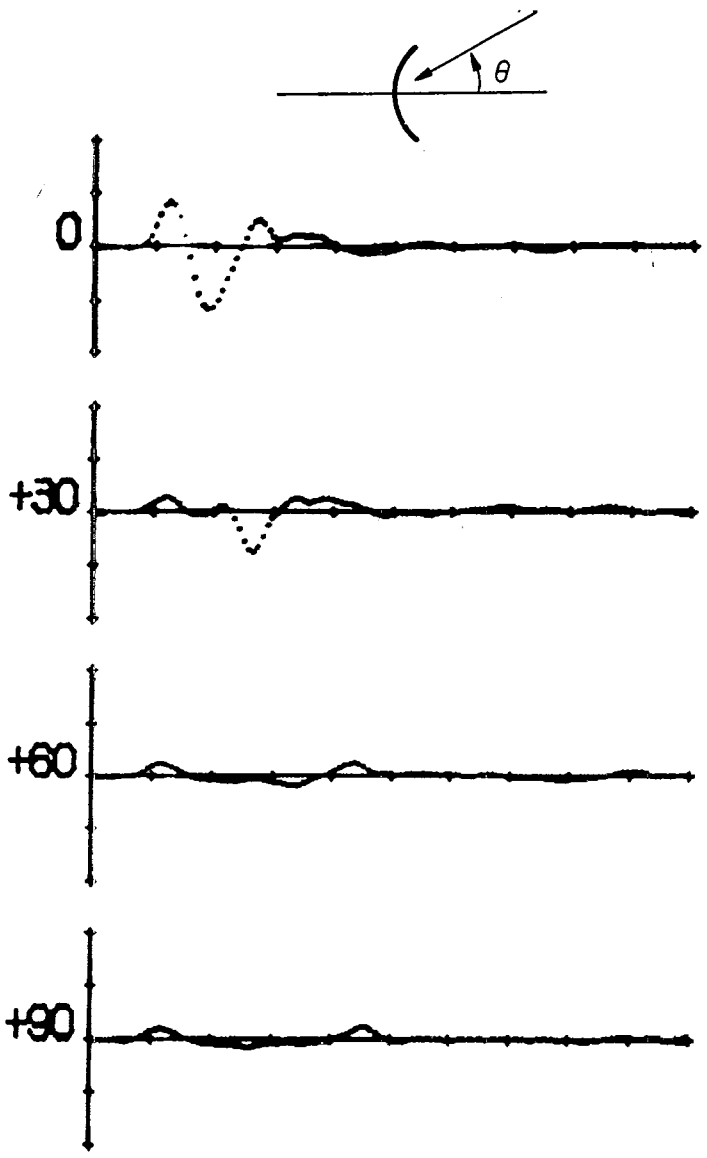

FIG. 47 Smoothed impulse response of parabolic dish with image plane normal to face for TM polarization (horizontal scale: 0.5 ns/div.; vertical scale: 10 mV/div.).

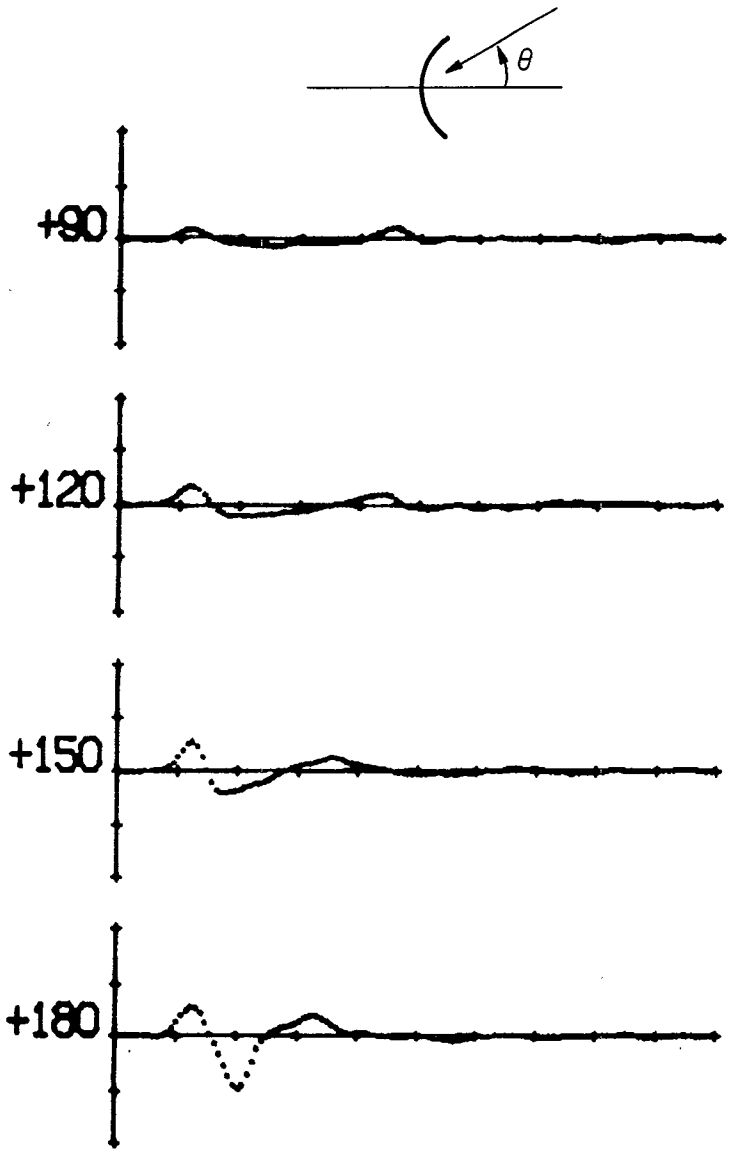

FIG. 48 Smoothed impulse response of parabolic dish with image plane symmetric about the dish for TM polarization (horizontal scale: 0.5 ns/div.; vertical scale: 10 mV/div.).

SECTION 4
EXTENSION OF SPACE-TIME INTEGRAL EQUATION TECHNIQUE TO OPEN, THIN SURFACES
(K. S. Menger and C. Maloy)

4.1 THE INFINITE PLANE

4.1.1 Introduction

This report describes a time-domain simulation of scattering problems in which the target is an open surface of zero thickness and zero resistivity. The scattered magnetic $\vec{H}$-field at a point distant from such a target has been computed on a Univac 418-III. The computations are numerically stable and the fields thus computed agree with the reflections from such targets measured on a time domain scattering range. Illumination of the target in these simulations was by a plane wave whose amplitude varied as a smooth (Gaussian) impulse in time. The time width of the impulse was set typically to about one-tenth the time required for light to traverse the target's longest dimension.

Briefly, this approach begins with solving for the current density $\vec{J}$ induced on the scattering surface by the incident wave.* With these currents, the $\vec{H}$-field scattered to any point outside the surface can be computed explicitly. To obtain the currents themselves, an integro-partial-differential equation for $\vec{J}$ in space and time is solved numerically. This formulation is due to Bennett,[1] who applied it to the simulation of thin wire scatterers. In the present application, the equation is solved on scattering surfaces of non-zero area where the tangential component of the total $\vec{E}$ field is known to vanish at all times.

Numerical approximations of the equation are such that at any point on the surface the current density for the next time increment can be computed explicitly from numbers that have already been computed; no matrix inversions are necessary. To achieve numerical stability, a priori knowledge of the behavior of $\vec{J}$ near edges was exploited. The component of current density perpendicular to an edge always vanishes at the edge due to the continuity of charge and to the absence of charge everywhere outside the surface. This

*Surface current density $\vec{J}$ is measured in amperes/meter. MKS units are used throughout.

property was used to extrapolate near edges, where the information is otherwise insufficient for numerical evaluation of certain one-sided spatial derivatives appearing in the integro-partial-differential equation. Also employed, and for the same reason, was the a priori behavior of the surface current density component parallel to the edge. This component varies hyperbolically with distance from the edge, and increases without bound at the edge itself if the resistivity is zero as has been assumed here.

Cartesian coordinates have been used for the rectangular and circular targets discussed in this section. For targets possessing cylindrical symmetry, a curvilinear coordinate is introduced which is coincident with the intersection of the scattering surface and a plane perpendicular to its longitudinal axis. A parabolic cylinder is given special attention, and the added axis for this particular case has the equation of a parabola. When expressed with the help of this fourth axis, all equations and boundary conditions employed for the rectangle are identical in form for the cylindrical targets. Indeed, the rectangle is a degenerate case of the open cylinder in the sense that the straight line is a degenerate form of a parabola. For the sake of presentation, however, the rectangular scattering surface will be discussed first to avoid initially the additional mathematics of the curvilinear coordinate.

4.1.2 Calculation of $\vec{H}$ from $\vec{J}$

Let $\vec{H}^i$ represent a magnetic field that is defined everywhere in empty space and for all time. If a perfectly conducting scatterer is introduced into the space at some fixed location, the magnetic field now present will in general differ from the original. Let this new total field be designated $\vec{H}^t$. Field $\vec{H}^t$ can be regarded as the vector total of the original field $\vec{H}^i$ (now regarded as incident upon the scatterer) and a scattered magnetic field $\vec{H}^s$ due to the presence of the target. In other words, for every point in space on or outside the scatterer designated by position vector $\vec{r}$ from some origin and for all time t measured from some reference event, $\vec{H}^s$ is defined by

$$\vec{H}^t(\vec{r}, t) = \vec{H}^i(\vec{r}, t) + \vec{H}^s(\vec{r}, t) \quad . \tag{26}$$

$\vec{H}^s$ is the magnetic field radiated by currents induced on the surface S' of the scatterer by $\vec{H}^t$ at that surface. Letting $\vec{J}(\vec{r}', t)$ represent this induced surface current density at each point $\vec{r}'$ on the surface at time t, then the scattered field $\vec{H}^s(\vec{r}, t)$ at any point $\vec{r}$ outside the surface S' and time t is given by

$$\vec{H}^s(\vec{r}, t) = \frac{1}{4\pi}\int_{S'} \frac{\vec{J}\left(\vec{r}', t - \frac{|\vec{r}-\vec{r}'|}{c}\right)}{|\vec{r}-\vec{r}'|^3} \times(\vec{r}-\vec{r}')\, dS' + \frac{1}{4\pi}\int_{S'} \frac{\frac{\partial \vec{J}}{\partial t}\left(\vec{r}', t - \frac{|\vec{r}-\vec{r}'|}{c}\right)}{c|\vec{r}-\vec{r}'|^2} \times(\vec{r}-\vec{r}')\, dS' \quad (27)$$

where c is the speed of light and each integration is carried over all points $\vec{r}'$ on the surface S'. Throughout this section, for any two points in space $\vec{r}_1$, $\vec{r}_2$, the Euclidean "line-of-sight" distance between them shall be denoted $|\vec{r}_1 - \vec{r}_2|$.

In principle then, a knowledge of $\vec{J}(\vec{r}', t)$ at all times t and for all points $\vec{r}'$ on S' is sufficient to compute scattered field $\vec{H}^s$. This solves the scattering problem in a manner that allows experimental verification. Whereas $\vec{J}$ itself would be difficult to measure in the laboratory, $\vec{H}^s$ is much less so.

4.1.3 Derivation of the Integro-Partial-Differential Equation for $\vec{J}$

To derive equations yielding the induced surface current $\vec{J}$, use is made of the given incident electric field $\vec{E}^i$, the scattered electric field $\vec{E}^s$, and the total electric field $\vec{E}^t$. These three electric fields accompany the three magnetic fields $\vec{H}^i$, $\vec{H}^s$, and $\vec{H}^t$ respectively, and are interrelated at every point $\vec{r}$ in space and time t by

$$\vec{E}^t(\vec{r}, t) = \vec{E}^i(\vec{r}, t) + \vec{E}^s(\vec{r}, t) \quad . \quad (28)$$

Applying Maxwell's equation $\vec{\nabla} \times \vec{E} = -\mu_o \frac{\partial \vec{H}}{\partial t}$ in free space to the scattered field alone gives

$$\vec{\nabla} \times \vec{E}^s + \mu_o \frac{\partial \vec{H}^s}{\partial t} = 0 \quad . \quad (29)$$

This, together with the vector potential $\vec{A}$ whose existence is assumed in $\vec{H}^s = \vec{\nabla} \times \vec{A}$ yields the equation

$$\vec{\nabla} \times \left(\vec{E}^s + \mu_o \frac{\partial \vec{A}}{\partial t} \right) = 0 \quad . \tag{30}$$

Any vector field whose curl vanishes everywhere in space must itself be the gradient of a scalar field. For the above vector field, namely $\vec{E}^s + \mu_o \frac{\partial \vec{A}}{\partial t}$, this scalar field potential shall be designated φ. Thus,

$$\vec{E}^s + \mu_o \frac{\partial \vec{A}}{\partial t} = -\vec{\nabla} \varphi \tag{31}$$

which after a time differentiation and use of $\epsilon_o \mu_o = 1/c^2$ becomes

$$\epsilon_o \frac{\partial \vec{E}^s}{\partial t} = - \frac{1}{c^2} \frac{\partial^2 \vec{A}}{\partial t^2} - \epsilon_o \vec{\nabla} \frac{\partial \varphi}{\partial t} \quad . \tag{32}$$

Applying Maxwell's equation $\vec{\nabla} \times \vec{H} = \vec{J} + \epsilon_o \frac{\partial \vec{E}}{\partial t}$ to the scattered field alone gives

$$\epsilon_o \frac{\partial \vec{E}^s}{\partial t} - \vec{\nabla} \times \vec{H}^s = \epsilon_o \frac{\partial \vec{E}^s}{\partial t} - \vec{\nabla} \times (\vec{\nabla} \times \vec{A}) = - \vec{J} \tag{33}$$

which with Eq. (32) becomes

$$- \frac{1}{c^2} \frac{\partial^2 \vec{A}}{\partial t^2} - \epsilon_o \vec{\nabla} \frac{\partial \varphi}{\partial t} - \vec{\nabla} \times (\vec{\nabla} \times \vec{A}) = - \vec{J} \quad . \tag{34}$$

Expansion of the curl of the curl of any vector field such as $\vec{A}$ is $\vec{\nabla}(\vec{\nabla} \cdot \vec{A}) - (\vec{\nabla} \cdot \vec{\nabla})\vec{A}$ so that Eq. (34) becomes

$$(\vec{\nabla} \cdot \vec{\nabla})\vec{A} - \frac{1}{c^2} \frac{\partial^2 A}{\partial t^2} - \vec{\nabla}\left(\epsilon_o \frac{\partial \varphi}{\partial t} + \vec{\nabla} \cdot \vec{A} \right) = - \vec{J} \quad . \tag{35}$$

The preceding relations, $\vec{\nabla} \times \vec{A} = \vec{H}^s$ and $\mu_o \frac{\partial \vec{A}}{\partial t} + \vec{\nabla}\varphi = -\vec{E}^s$, are insufficient to specify $\vec{A}$ uniquely, so another constraint must be chosen to relate these two potentials to one another. For the present purposes it is particularly convenient to choose the Lorentz gauge relation

$$\vec{\nabla} \cdot \vec{A} + \epsilon_o \frac{\partial \varphi}{\partial t} = 0 \tag{36}$$

because, upon taking the gradient of both sides, i.e.,

$$\vec{\nabla}(\vec{\nabla} \cdot \vec{A}) + \epsilon_o \vec{\nabla} \frac{\partial \varphi}{\partial t} = 0 \tag{37}$$

it can be used to uncouple $\vec{A}$ from φ in Eq. (35):

$$(\vec{\nabla} \cdot \vec{\nabla})\vec{A} - \frac{1}{c^2} \frac{\partial^2 \vec{A}}{\partial t^2} = -\vec{J} \ . \tag{38}$$

This wave equation for vector potential $\vec{A}$ is the direct result of and the motivation for the Lorentz gauge. The vector potential $\vec{A}$ computed from

$$\vec{A}(\vec{r}, t) = \frac{1}{4\pi} \int_\infty \frac{J\left(\vec{r}', t - \frac{|\vec{r}' - \vec{r}|}{c}\right)}{|\vec{r} - \vec{r}'|} dV' \tag{39}$$

at each space point $\vec{r}$ and time t satisfies Eq. (38); the integration is carried over every point $\vec{r}'$ in space.*

In the scattering problem, $\vec{J}$ is unknown and therefore $\vec{A}$ cannot be computed from Eq. (39) without further information. The added information is the $\vec{E}$-field boundary condition on the perfectly conducting surface; namely, the component of $\vec{E}^t$ tangent to the surface S' vanishes everywhere on that surface. Thus, for every point $\vec{r}'$ on S'

$$\left(\vec{E}^t(\vec{r}', t)\right)_{tan} = 0 = \left(\vec{E}^i(\vec{r}', t)\right)_{tan} + \left(\vec{E}^s(\vec{r}', t)\right)_{tan}$$

*Here, $\vec{J}$ is in amperes/meter; $\vec{A}$ is in amperes.

for all time. The above vector equation is equivalent to two scalar equations; the same is true of those vector equations to follow, which, like the above, allude to the surface tangent. Differentiating the above equation with respect to time gives

$$\epsilon_o \left(\frac{\partial \vec{E}^s}{\partial t}\right)_{tan} = - \epsilon_o \left(\frac{\partial \vec{E}^i}{\partial t}\right)_{tan}$$

and combining this with the tangential component of Eq. (32), i.e., with

$$\epsilon_o \left(\frac{\partial \vec{E}^s}{\partial t}\right)_{tan} = - \frac{1}{c^2} \left(\frac{\partial^2 \vec{A}}{\partial t^2}\right)_{tan} - \epsilon_o \left(\vec{\nabla} \frac{\partial \varphi}{\partial t}\right)_{tan}$$

gives

$$- \epsilon_o \left(\vec{\nabla} \frac{\partial \varphi}{\partial t}\right)_{tan} - \frac{1}{c^2} \left(\frac{\partial^2 \vec{A}}{\partial t^2}\right)_{tan} = - \epsilon_o \left(\frac{\partial \vec{E}^i}{\partial t}\right)_{tan}$$

which is valid for all time but only on the scattering surface S'. Substituting the tangential component of the gradient of the Lorentz gauge, Eq. (36), namely

$$\left(\vec{\nabla}(\vec{\nabla} \cdot \vec{A})\right)_{tan} + \epsilon_o \left(\vec{\nabla} \frac{\partial \varphi}{\partial t}\right)_{tan} = 0$$

into the preceding gives

$$\left(\vec{\nabla}(\vec{\nabla} \cdot \vec{A})\right)_{tan} - \frac{1}{c^2} \left(\frac{\partial^2 \vec{A}}{\partial t^2}\right)_{tan} = - \epsilon_o \left(\frac{\partial \vec{E}^i}{\partial t}\right)_{tan} . \qquad (40)$$

Again, this equation holds only for points on the surface S'. Observe that the forcing function on the right-hand side is known because it is directly calculable by differentiation with respect to time of the incident electric field, a given field in this problem.

Equation (40) is one of the two equations solved numerically in the present approach. The other required equation is obtained from a specialization of Eq. (39). Since $\vec{J}$ vanishes everywhere outside the conducting surface, the integration in that equation need be carried over the surface S' only:

$$\vec{A}(\vec{r}, t) = \frac{1}{4\pi} \int_{S'} \frac{\vec{J}\left(\vec{r}', t - \frac{|\vec{r} - \vec{r}'|}{c}\right)}{|\vec{r} - \vec{r}'|} dS' \qquad (41)$$

for any point $\vec{r}$ in space and every time t .*

Equations (40) and (41) can be combined to give a single integro-partial-differential equation for $\vec{J}$ in space and time

$$\left[\vec{\nabla}\left(\vec{\nabla} \cdot \frac{1}{4\pi} \int_{S'} \frac{\vec{J}\left(\vec{r}', t - \frac{|\vec{r} - \vec{r}'|}{c}\right) dS'}{|\vec{r} - \vec{r}'|}\right) - \frac{1}{c^2} \frac{\partial^2}{\partial t^2}\left(\frac{1}{4\pi} \int_{S'} \frac{\vec{J}\left(\vec{r}', t - \frac{|\vec{r} - \vec{r}'|}{c}\right)}{|\vec{r} - \vec{r}'|} dS'\right)\right]_{tan}$$

$$= -\epsilon_o \left(\frac{\partial \vec{E}^i}{\partial t}\right)_{tan} .$$

It is, however, more convenient for numerical solution to deal with the distinct equations (40) and (41). It remains to be shown that Eqs. (40) and (41) can in fact be solved numerically to yield the desired current density $\vec{J}$, buried as it is in the kernel of an integral. This is done in the next section.

4.1.4 Analytical Expressions for the Numerical Solution of $\vec{J}$

The kernel in Eq. (41) is singular when the integration passes through the point $\vec{r}' = \vec{r}$. Accordingly, the numerical solution for $\vec{J}$ begins with the splitting of this integral into two integrals, one of which integrates the kernel over a subsection $S'_{\vec{r}}$ of the surface S' . Subsection $S'_{\vec{r}}$ includes

*Here $\vec{J}$ is in amperes/meter; $\vec{A}$ is still in amperes.

the point $\vec{r}$ and has an area which is small compared to the area of S'. The second integral integrates the kernel over the remainder of the surface, $S' - S'_{\vec{r}}$, where the kernel is everywhere nonsingular. Thus, for each $\vec{r}$ on S'

$$\vec{A}(\vec{r},t) = \frac{1}{4\pi}\int_{S'_{\vec{r}}} \frac{\vec{J}\left(\vec{r}', t - \frac{|\vec{r}-\vec{r}'|}{c}\right)}{|\vec{r}-\vec{r}'|}\, dS' + \frac{1}{4\pi}\int_{S'-S'_{\vec{r}}} \frac{\vec{J}\left(\vec{r}', t - \frac{|\vec{r}-\vec{r}'|}{c}\right)}{|\vec{r}-\vec{r}'|}\, dS' \quad (42)$$

for all time. It will be convenient to designate these two pieces that make up the original surface integral by shorter labels; accordingly, let

$$\vec{A}'(\vec{r},t) = \frac{1}{4\pi}\int_{S'_{\vec{r}}} \frac{\vec{J}\left(\vec{r}', t - \frac{|\vec{r}-\vec{r}'|}{c}\right)}{|\vec{r}-\vec{r}'|}\, dS' \quad (43)$$

and

$$\vec{A}''(\vec{r},t) = \frac{1}{4\pi}\int_{S'-S'_{\vec{r}}} \frac{\vec{J}\left(\vec{r}', t - \frac{|\vec{r}-\vec{r}'|}{c}\right)}{|\vec{r}-\vec{r}'|}\, dS' \quad (44)$$

so that $\vec{A}(\vec{r},t) = \vec{A}'(\vec{r},t) + \vec{A}''(\vec{r},t)$ everywhere and always.

Even though the kernel in Eq. (43) passes through a singularity, $\vec{A}'(\vec{r},t)$ can be approximated analytically. Appendix 8.1 demonstrates that if S' is a square patch of surface, δ on a side, and if $\vec{J}$ is assumed constant over S' and equal to its value at the center $\vec{r}$ of the square, namely $\vec{J}(\vec{r},t)$, then

$$\vec{A}'(\vec{r},t) \approx \frac{\delta \cdot \ell n(1+\sqrt{2})}{\pi}\ \vec{J}(\vec{r},t)\ .$$

The error in this approximation approaches zero as $\delta \to 0$. The fact that $\vec{J}$ is proportional to $\vec{A}'$ everywhere and always is important to this numerical approach; the relationship as presented in Eq. (45) below is the one used in actual computation:

$$\vec{J}(\vec{r}, t) = \frac{\pi}{\delta \cdot \ell n(1+\sqrt{2})} \vec{A}'(\vec{r}, t) \quad . \tag{45}$$

To conclude the formulation of the computational formulas, Eq. (40) is recast into Eq. (46) below by substituting $\vec{A}' + \vec{A}''$ for $\vec{A}$ and rearranging some terms:

$$\frac{1}{c^2}\left(\frac{\partial^2 \vec{A}'}{\partial t^2}\right)_{tan} = \epsilon_o\left(\frac{\partial \vec{E}^i}{\partial t}\right)_{tan} - \frac{1}{c^2}\left(\frac{\partial^2 \vec{A}''}{\partial t^2}\right)_{tan} + \left(\vec{\nabla}(\vec{\nabla} \cdot \vec{A}')\right)_{tan} + \left(\vec{\nabla}(\vec{\nabla} \cdot \vec{A}'')\right)_{tan} . \tag{46}$$

Formulations (44) and (46) are due to Bennett, who applied them in the simulation of a thin-wire scatterer of zero area. In this section, they will be specialized to scattering surfaces of nonzero area. For this purpose, the equations are quantized where necessary to permit calculation of $\vec{A}'$, $\vec{A}''$, and $\vec{J}$ on a computer.

4.1.5 Quantizing and Processing for the Infinite Plane Scatterer

In the section to follow, Eqs. (44), (45) and (46) are specialized for an infinite plane target of zero thickness. Space will be measured by a Cartesian coordinate system whose x- and y-axes are located in the plane of the target.

Since the component of current density normal to the target, J_z , vanishes everywhere for all time, Eq. (45) specializes to the three scalar

equations

$$J_z(x, y, t) = 0$$

$$J_y(x, y, t) = \frac{\pi}{\delta \cdot \ell n(1+\sqrt{2})} A'_y(x, y, t)$$

$$J_x(x, y, t) = \frac{\pi}{\delta \cdot \ell n(1+\sqrt{2})} A'_x(x, y, t) \qquad (47)$$

which are valid at all points (x, y) on the scattering plane for all time. Notice that the z-component of the above vector equation implies that $A'_z(x, y, t) = 0$ everywhere and always.

Equation (44) specializes to the three scalar relations below, and these are valid at all points (x, y) on the scatterer and at all times t :

$$A''_z(x, y, t) = 0$$

$$A''_y(x, y, t) = \frac{1}{4\pi} \int_{-\infty}^{\infty} \int_{-\infty}^{\infty} \frac{J_y\left(x', y', t - \frac{\sqrt{(x-x')^2 + (y-y')^2}}{c}\right)}{\sqrt{(x-x')^2 + (y-y')^2}} \, dx' \, dy'$$

$$A''_z(x, y, t) = \frac{1}{4\pi} \int_{-\infty}^{\infty} \int_{-\infty}^{\infty} \frac{J_x\left(x', y', t - \sqrt{(x-x')^2 + (y-y')^2}\right)}{\sqrt{(x-x')^2 + (y-y')^2}} \, dx' \, dy'. \qquad (48)$$

Both of the above integrations are carried over the entire xy plane <u>except</u> for a square patch of side δ centered at the point (x, y) with edges parallel to the x- and y-axes. Side δ will be specified when these analytic formulas are quantized for digital computation.

The gradient of the divergence of the vector potential required in Eq. (46) is computed in Cartesian coordinates as follows. Recalling that $A_z = A'_z + A''_z = 0$ everywhere and always, and letting $\vec{A} = \langle A_x, A_y, A_z \rangle = \langle A_x, A_y, 0 \rangle$:

$$\vec{\nabla}(\vec{\nabla}\cdot\vec{A}) = \vec{\nabla}\left(\frac{\partial A_x}{\partial x} + \frac{\partial A_y}{\partial y}\right)$$

$$= \left\langle \frac{\partial^2 A_x}{\partial x^2} + \frac{\partial^2 A_y}{\partial x \partial y}\ ,\ \frac{\partial^2 A_x}{\partial x \partial y} + \frac{\partial^2 A_y}{\partial y^2}\ ,\ \frac{\partial^2 A_x}{\partial x \partial z} + \frac{\partial^2 A_y}{\partial y \partial z} \right\rangle .$$

Along the two directions tangent to the planar surface, namely the x-axis and y-axis directions, Eq. (46) specializes, after some rearrangement, to

$$\frac{1}{c^2}\frac{\partial^2 A'_x}{\partial t^2} = \epsilon_o \frac{\partial E^i_x}{\partial t} - \frac{1}{c^2}\frac{\partial^2 A''_x}{\partial t^2} + \frac{\partial^2 A'_x}{\partial x^2} + \frac{\partial^2 A'_y}{\partial x \partial y} + \frac{\partial^2 A''_x}{\partial x^2} + \frac{\partial^2 A''_y}{\partial x \partial y}$$

and

$$\frac{1}{c^2}\frac{\partial^2 A'_y}{\partial t^2} = \epsilon_o \frac{\partial E^i_y}{\partial t} - \frac{1}{c^2}\frac{\partial^2 A''_y}{\partial t^2} + \frac{\partial^2 A'_x}{\partial x \partial y} + \frac{\partial^2 A'_y}{\partial y^2} + \frac{\partial^2 A''_x}{\partial x \partial y} + \frac{\partial^2 A''_y}{\partial y^2} \qquad (49)$$

both of which are valid everywhere on the scattering planar surface S', which is also the xy plane, at all times.

For purposes of digital processing, the planar target is tessellated into an infinite two-dimensional array of squares, each of side $\delta = \Delta s$. Equations (47), (48), and (49) are computed at the center of each such square patch. The origin of the coordinate system is such that patch centers are the set of points $(x, y) = (m\,\Delta s, n\,\Delta s)$, where m and n range over all the integers. Furthermore, the equations are computed only at the times $t = k\Delta t$, where Δt is fixed in any given simulation and k ranges over all the integers. Time is measured from the occurrence of some easily specified event; for this discussion $t = 0$ when the earliest nonzero portion of the incident wave first strikes any part of the target. This is a particularly convenient choice of time origin because for all $t < 0$, the target can be assumed to have been immersed in field-free space, so that both $\vec{J}$ and $\vec{A}$ are zero everywhere on the target for <u>all</u> negative times.

To begin the description of the digital processing for this planar target and others as well, it will be assumed that the fields $\vec{J}$, $\vec{A}'$, and $\vec{A}''$ have been computed at all patch centers on the target for all times that are integral multiples of Δt up to and including the specific time $k\Delta t$. At the conclusion of one iteration of the processing to be described, the fields $\vec{J}$, $\vec{A}'$, and $\vec{A}''$ will have been computed at all patch centers for time $k\Delta t + \Delta t$. If the processing is just beginning (i.e., if $k=0$), then the past values of $\vec{J}$, $\vec{A}'$, and $\vec{A}''$ are all zero. In either case, the fact that at the end of one processing iteration the values of these three fields are known on the target for all times up to and including the time $k\Delta t + \Delta t$ implies that now they can be computed for time $k\Delta t + 2\Delta t$ in the next iteration. Thus the assumption is proven valid, and by induction $\vec{J}$, $\vec{A}'$, and $\vec{A}''$ can be computed for all $k\Delta t$.

Consider any one patch center $(m\Delta s, n\Delta s)$ and the objective of computing $\vec{J}$ at this space point for time $k\Delta t + \Delta t$. Fields $\vec{A}''$, $\vec{A}'$, and $\vec{J}$ are computed at this space-time point $(m\Delta s, n\Delta s, k\Delta t + \Delta t)$, in that order, in the following manner.

Each integral in Eq. (48) is approximated by a double summation. For $\vec{A}''$,

$$A_x''(m\Delta s, n\Delta s, k\Delta t + \Delta t)$$

$$= \frac{(\Delta s)^2}{4\pi} \sum_{m'} \sum_{n'} \frac{J_x\left(m'\Delta s, n'\Delta s, k\Delta t + \Delta t - \frac{\sqrt{(m\Delta s - m'\Delta s)^2 + (n\Delta s - n'\Delta s)^2}}{c}\right)}{\sqrt{(m\Delta s - m'\Delta s)^2 + (n\Delta s - n'\Delta s)^2}} \qquad (50)$$

where the double summation is carried over all patch centers $(m'\Delta s, n'\Delta s)$, except $(m'\Delta s, n'\Delta s) = (m\Delta s, n\Delta s)$, the space point at which A_x'' is being evaluated. In the infinite planar target, this would imply that m' and n' each range from $-\infty$ to ∞. However, the summation need only deal with "active" patches, i.e., those $(m'\Delta s, n'\Delta s)$ for which

$$k\Delta t + \Delta t - \frac{\sqrt{(m\Delta s - m'\Delta s)^2 + (n\Delta s - n'\Delta s)^2}}{c} \geq 0 \quad .$$

When the left-hand side of this inequality is negative, $\vec{J}$ vanishes and contributes nothing to the summation. Indeed, the inequality is satisfied by only those patch centers $(m'\Delta s, n'\Delta s)$ which are within a radius of $c(k\Delta t + \Delta t)$ from $(m\Delta s, n\Delta s)$, and these are always finite in number.

Another important consideration is that

$$k\Delta t + \Delta t - \frac{\sqrt{(m\Delta s - m'\Delta s)^2 + (n\Delta s - n'\Delta s)^2}}{c} \leq k\Delta t$$

hold because if the left-hand side exceeds $k\Delta t$, a future value of $\vec{J}$ is required that has not yet been computed, violating the assumption made at the outset of this discussion. Recalling that $(m\Delta s, n\Delta s)$ is excluded from the summation for $A''(m\Delta s, n\Delta s)$, the left-hand side of the above inequality is smallest at the four patch centers nearest $(m\Delta s, n\Delta s)$, e.g., for $(m\Delta s + \Delta s, n\Delta s)$. To satisfy the initial assumption it is then necessary that $\Delta t - \frac{\Delta s}{c} \leq 0$.

If Δt has been selected to satisfy $c\Delta t \leq \Delta s$, then $J(m'\Delta s, n'\Delta s, \tau)$ where $\tau = k\Delta t + \Delta t - \frac{\sqrt{(m\Delta s - m'\Delta s)^2 + (n\Delta s - n'\Delta s)^2}}{c}$, is indeed a past value of J_x. However, it has not been computed if, as is generally the case, $\frac{\sqrt{(m\Delta s - m'\Delta s)^2 + (n\Delta s - n'\Delta s)^2}}{c}$ is not an integral multiple of Δt. In the present approach, the required value of J_x is obtained by linear interpolation in time at the patch $(m'\Delta s, n'\Delta s)$ in question. Thus

$$J_x(m'\Delta s, n'\Delta s, \tau) \approx \left(\left\lfloor \frac{\tau}{\Delta t} \right\rfloor + 1 - \frac{\tau}{\Delta t}\right) \cdot J_x\left(m'\Delta s, n'\Delta s, \left\lfloor \frac{\tau}{\Delta t} \right\rfloor \Delta t\right)$$

$$+ \left(\frac{\tau}{\Delta t} - \left\lfloor \frac{\tau}{\Delta t} \right\rfloor\right) \cdot J_x\left(m'\Delta s, n'\Delta s, \left\lfloor \frac{\tau}{\Delta t} \right\rfloor \Delta t + \Delta t\right) \quad , \qquad (51)$$

where $\left\lfloor \frac{\tau}{\Delta t} \right\rfloor$ is the floor of $\frac{\tau}{\Delta t}$, i.e., the largest integer not exceeding $\frac{\tau}{\Delta t}$.

For the special case in which the infinite plane is illuminated by a plane wave whose front is parallel to the target, every patch receives the same forcing field. Hence the vector fields $\vec{J}$, $\vec{A}'$, and $\vec{A}''$ have time dependencies that are common to all patches. Thus computation at any given patch center, say that at the origin $(0, 0)$, solves the problem for the entire target. Only $\vec{J}(0, 0, k\Delta t)$, $\vec{A}'(0, 0, k\Delta t)$ and $\vec{A}''(0, 0, k\Delta t)$ need be computed and stored for $k \geq 0$, a fact which greatly simplifies the computer program that simulates the infinite plane case.

The computation of $A''_x(m\Delta s, n\Delta s, k\Delta t + \Delta t)$ is followed by the analogous computation $A''_y(m\Delta s, n\Delta s, k\Delta t + \Delta t)$

$$= \frac{(\Delta s)^2}{4\pi} \sum_{m'} \sum_{n'} \frac{J_y\left(m'\Delta s, n'\Delta s, k\Delta t + \Delta t - \frac{\sqrt{(m\Delta s - m'\Delta s)^2 + (n\Delta s - n'\Delta s)^2}}{c}\right)}{\sqrt{(m\Delta s - m'\Delta s)^2 + (n\Delta s - n'\Delta s)^2}} \qquad (52)$$

summed over all patches $(m'\Delta s, n'\Delta s) \neq (m\Delta s, n\Delta s)$, where the linear interpolation

$$J_y(m'\Delta s, n'\Delta s, \tau) \approx \left(\left\lfloor \frac{\tau}{\Delta t} \right\rfloor + 1 - \frac{\tau}{\Delta t}\right) \cdot J_y\left(m'\Delta s, n'\Delta s, \left\lfloor \frac{\tau}{\Delta t} \right\rfloor \Delta t\right)$$

$$+ \left(\frac{\tau}{\Delta t} - \left\lfloor \frac{\tau}{\Delta t} \right\rfloor\right) \cdot J_y\left(m'\Delta s, n'\Delta s, \left\lfloor \frac{\tau}{\Delta t} \right\rfloor \Delta t + \Delta t\right) \qquad (53)$$

is used on the active patches as required, with $\left\lfloor \frac{\tau}{\Delta t} \right\rfloor$ and $\frac{\tau}{\Delta t}$ as in Eq. (51).

Computed next are A'_x and A'_y at $(m\Delta s, n\Delta s, k\Delta t + \Delta t)$ via a quantized version of Eq. (49). Partial derivatives appearing in those two equations are replaced with the numerical approximation below, where F stands for any of the scalar fields A'_x, A'_y, A''_x, A''_y :

$$\frac{\partial^2 F}{\partial t^2}(m\Delta s, n\Delta s, k\Delta t) \approx \frac{F(m\Delta s, n\Delta s, k\Delta t + \Delta t) - 2F(m\Delta s, n\Delta s, k\Delta t) + F(m\Delta s, n\Delta s, k\Delta t - \Delta t)}{(\Delta t)^2}$$

$$\frac{\partial^2 F}{\partial x^2}(m\Delta s, n\Delta s, k\Delta t) \approx \frac{F(m\Delta s + \Delta s, n\Delta s, k\Delta t) - 2F(m\Delta s, n\Delta s, k\Delta t) + F(m\Delta s - \Delta s, n\Delta s, k\Delta t)}{(\Delta s)^2}$$

$$\frac{\partial^2 F}{\partial y^2}(m\Delta s, n\Delta s, k\Delta t) \approx \frac{F(m\Delta s, n\Delta s + \Delta s, k\Delta t) - 2F(m\Delta s, n\Delta s, k\Delta t) + F(m\Delta s, n\Delta s - \Delta s, k\Delta t)}{(\Delta s)^2}$$

$$\frac{\partial^2 F}{\partial x \partial y}(m\Delta s, n\Delta s, k\Delta t) \approx \frac{F(m\Delta s + \Delta s, n\Delta s + \Delta s, k\Delta t) + F(m\Delta s - \Delta s, n\Delta s - \Delta s, k\Delta t)}{4(\Delta s)^2}$$

$$- \frac{F(m\Delta s + \Delta s, n\Delta s - \Delta s, k\Delta t) + F(m\Delta s - \Delta s, n\Delta s + \Delta s, k\Delta t)}{4(\Delta s)^2} \qquad (54)$$

It should be clear that for infinite plane parallel plane-wave illumination, all spatial derivatives of the above sort vanish, and only the temporal derivatives remain. In the finite flat figures discussed later, however, the spatial derivatives in general do not vanish.

With approximations (54) each derivative in Eq. (49) requires three or four values of A'_x, A'_y, A''_x, A''_y, and of this collection, all have been computed at this point in the processing with the exception of $A'_x(m\Delta s, n\Delta s, k\Delta t + \Delta t)$ and $A'_y(m\Delta s, n\Delta s, k\Delta t + \Delta t)$. Using approximations (54) then for the derivatives in Eq. (49) and solving for the unknown in each equation, gives

$$
\begin{aligned}
A_x'(m\Delta s, n\Delta s, k\Delta t + \Delta t) = {} & 2A_x'(m\Delta s, n\Delta s, k\Delta t) - A_x'(m\Delta s, n\Delta s, k\Delta t - \Delta t) \\
& + (c\Delta t)^2 \epsilon_o \frac{\partial E_x^i}{\partial t}(m\Delta s, n\Delta s, k\Delta t) \\
& - A_x''(m\Delta s, n\Delta s, k\Delta t + \Delta t) + 2A_x''(m\Delta s, n\Delta s, k\Delta t) \\
& - A_x''(m\Delta s, n\Delta s, k\Delta t - \Delta t) \\
& + \left(\frac{c\Delta t}{\Delta s}\right)^2 \Big[A_x'(m\Delta s + \Delta s, n\Delta s, k\Delta t) \\
& - 2A_x'(m\Delta s, n\Delta s, k\Delta t) \\
& + A_x'(m\Delta s - \Delta s, n\Delta s, k\Delta t) \\
& + A_x''(m\Delta s + \Delta s, n\Delta s, k\Delta t) - 2A_x''(m\Delta s, n\Delta s, k\Delta t) + A_x''(m\Delta s - \Delta s, n\Delta s, k\Delta t) \\
& + \frac{A_y'(m\Delta s + \Delta s, n\Delta s + \Delta s, k\Delta t) + A_y'(m\Delta s - \Delta s, n\Delta s - \Delta s, k\Delta t)}{4} \\
& - \frac{A_y'(m\Delta s + \Delta s, n\Delta s - \Delta s, k\Delta t) + A_y'(m\Delta s - \Delta s, n\Delta s + \Delta s, k\Delta t)}{4} \\
& + \frac{A_y''(m\Delta s + \Delta s, n\Delta s + \Delta s, k\Delta t) + A_y''(m\Delta s - \Delta s, n\Delta s - \Delta s, k\Delta t)}{4} \\
& - \frac{A_y''(m\Delta s + \Delta s, n\Delta s - \Delta s, k\Delta t) + A_y''(m\Delta s - \Delta s, n\Delta s + \Delta s, k\Delta t)}{4} \Big] \qquad (55)
\end{aligned}
$$

and

$$A'_y(m\Delta s, n\Delta s, k\Delta t + \Delta t) =$$

$$2A'_y(m\Delta s, n\Delta s, k\Delta t) - A'_y(m\Delta s, n\Delta s, k\Delta t - \Delta t) + (c\Delta t)^2 \varepsilon_o \frac{\partial E_y^i}{\partial t}(m\Delta s, n\Delta s, k\Delta t)$$

$$- A''_y(m\Delta s, n\Delta s, k\Delta t + \Delta t) + 2A''_y(m\Delta s, n\Delta s, k\Delta t) - A''_y(m\Delta s, n\Delta s, k\Delta t - \Delta t)$$

$$+ \left(\frac{c\Delta t}{\Delta s}\right)^2 \Big[A'_y(m\Delta s, n\Delta s + \Delta s, k\Delta t) - 2A'_y(m\Delta s, n\Delta s, k\Delta t) + A'_y(m\Delta s, n\Delta s - \Delta s, k\Delta t)$$

$$+ A''_y(m\Delta s, n\Delta s + \Delta s, k\Delta t) - 2A''_y(m\Delta s, n\Delta s, k\Delta t) + A''_y(m\Delta s, n\Delta s - \Delta s, k\Delta t)$$

$$+ \frac{A'_x(m\Delta s + \Delta s, n\Delta s + \Delta s, k\Delta t) + A'_x(m\Delta s - \Delta s, n\Delta s - \Delta s, k\Delta t)}{4}$$

$$- \frac{A'_x(m\Delta s + \Delta s, n\Delta s - \Delta s, k\Delta t) + A'_x(m\Delta s - \Delta s, n\Delta s + \Delta s, k\Delta t)}{4}$$

$$+ \frac{A''_x(m\Delta s + \Delta s, n\Delta s + \Delta s, k\Delta t) + A''_x(m\Delta s - \Delta s, n\Delta s - \Delta s, k\Delta t)}{4}$$

$$- \frac{A''_x(m\Delta s + \Delta s, n\Delta s - \Delta s, k\Delta t) + A''_x(m\Delta s - \Delta s, n\Delta s + \Delta s, k\Delta t)}{4}\Big] . \qquad (56)$$

The x- and y-components of the forcing field $\varepsilon_o \frac{\partial E^i}{\partial t}$ can be evaluated at each space-time point $(m\Delta s, n\Delta s, k\Delta t)$ directly from the time derivative of the incident field $\vec{E}^i$ at each point, provided that $\vec{E}^i$ is differentiable. For the simulations to be discussed later, $\vec{E}^i$ was a smoothed impulse and the required values of the forcing field were obtained from the analytic expression for the corresponding smoothed doublet. Observe also that the values of $\vec{A}'$ and $\vec{A}''$ at the space-time point $(m\Delta s, n\Delta s, k\Delta t + \Delta t)$ are required in Eqs. (55) and (56); these were computed earlier in Eqs. (50) and (52). All other field values appearing in those two formulas are at the time $k\Delta t$ or prior. Thus $A'_x(m\Delta s, n\Delta s, k\Delta t + \Delta t)$ and $A'_y(m\Delta s, n\Delta s, k\Delta t + \Delta t)$

are computed explicitly by Eqs. (55) and (56) respectively; in particular no matrix inversion is necessary.

The final processing step makes use of Eq. (47) to compute the current density. Thus

$$J_x(m\Delta s, n\Delta s, k\Delta t + \Delta t) = \frac{\pi}{\Delta s \, \ell n(1+\sqrt{2})} A'_x(m\Delta s, n\Delta s, k\Delta t + \Delta t) \tag{57}$$

and

$$J_y(m\Delta s, n\Delta s, k\Delta t + \Delta t) = \frac{\pi}{\Delta s \, \ell n(1+\sqrt{2})} A'_y(m\Delta s, n\Delta s, k\Delta t + \Delta t) \quad . \tag{58}$$

This finishes the calculating required to compute $\vec{J}$ for any patch center at time $k\Delta t + \Delta t$. When $\vec{J}$ has been computed for all patch centers at $k\Delta t + \Delta t$ (points, which because of the explicit nature of this series of computations, can be processed in any order) one entire iteration has been completed. Values of $\vec{J}$, $\vec{A}'$, $\vec{A}''$ are now known for all patch centers and at all multiples of Δt up to and including $k\Delta t + \Delta t$. This is the required information for computing these three vector fields at $k\Delta t + 2\Delta t$. By induction, this iterative procedure can be conducted out to $k\Delta t$ for any $k > 0$.

4.2 THE RECTANGLE AND THE CIRCLE

Spatial derivatives present a problem for finite figures that did not arise in the infinite plane. For a patch centered at or near the edge (or corner) of a finite figure, one or more of the spatial derivatives in Eq. (49) cannot be evaluated if they are approximated as in Eq. (54) because some of the values of $\vec{A}'$ and $\vec{A}''$ called for in Eqs. (55) and (56) are not available at such an edge-interior patch since they are values at spatial points outside the scattering surface. For those patches which are <u>properly</u> interior to the figure in the sense that all eight neighboring patches are interior, Eqs. (50) through (58) are used without modification. For those patches which are <u>edge</u> interior in the sense that they are not properly interior, extrapolation procedures or their equivalent must be employed.

Clearly the values of $\vec{J}$ at edge-interior patch centers are part of the information required to compute the scattered magnetic field $\vec{H}^s$ as discussed in Sec. 4.1. These same values are also necessary to compute $\vec{A}''$ everywhere on the surface in the next iteration. If $\vec{J}$ itself is extrapolated at the edge-interior patch centers, then it is necessary to compute $\vec{A}''$ at those same patches, but not $\vec{A}'$. The extrapolation procedure for $\vec{J}$ to be described is applied to each edge-interior patch after all field values have been computed in a given iteration using Eqs. (50) - (58) at each properly interior patch center.

The following extrapolation procedure was found to be numerically stable for rectangular targets. It exploits the a priori behavior of $\vec{J}$ at and near the edges of any thin scatterer, flat or otherwise. Figure 49(a) presents a blown-up view at the edge of a thin scattering surface S', where two orthogonal components of $\vec{J}$ in the plane that is tangent at space point (x_o, y_o) have also been represented.

Let ρ designate the function which with each point on S' associates the (scalar) distance that it is from the nearest edge point. In the figure, for example, (x_o, y_o) is distance $\rho(x_o, y_o)$ from its nearest edge point (x_e, y_e). Also shown in the figure is $J_{/\!/}(x_o, y_o)$ which is the component of $\vec{J}$ at (x_o, y_o) parallel to the edge of the surface at point (x_e, y_e). Similarly, $J_{\perp}(x_o, y_o)$ is the component of $\vec{J}(x_o, y_o)$ which is perpendicular to that edge at (x_e, y_e). The extrapolation procedure exploits the fact that $J_{\perp}(x_o, y_o) \approx 0$ and $J_{/\!/}(x_o, y_o) = \frac{K}{\rho(x_o, y_o)}$ for some constant K (Ref. 8, p. 569). In fact, $J_{/\!/}(x_o, y_o)$ increases without limit as (x_o, y_o) is made to approach (x_e, y_e), and $J_{\perp}(x_e, y_e) = 0$.

Given now a rectangular target on which the x- and y-axes have been aligned parallel to its two pairs of opposing sides respectively, it will be assumed that the dimensions of the rectangle are $M\Delta s$ by $N\Delta s$, where M and N are positive integers, and also that the perimeter of the rectangle is the collection of outside edges of all the edge-interior (square) patches. Thus, if $(m\Delta s, n\Delta s)$ in this coordinate system is the center of an edge-interior patch in this rectangle, then $\rho(m\Delta s, n\Delta s) = \Delta s/2$. An example of such a tessellated rectangle is shown in Fig. 49(b).

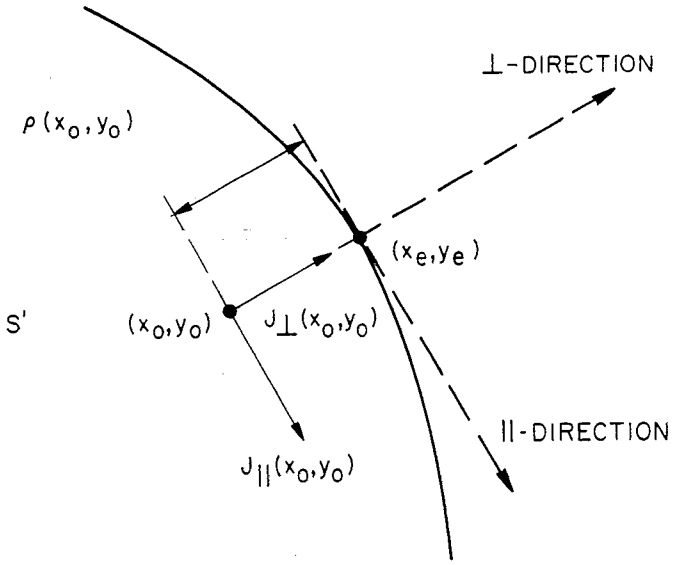

(a)

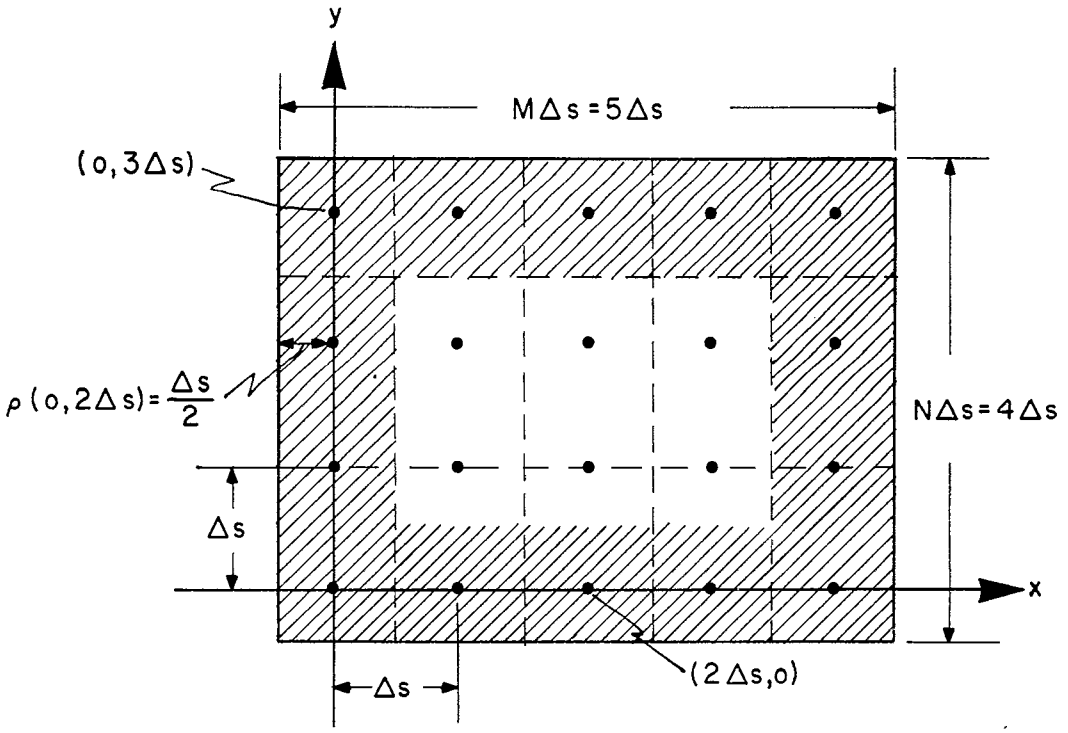

(b)

FIG. 49 (a) Exploded view of planar scattering surface S' near an edge.

(b) A tessellated rectangle: the shaded patches are edge interior, while the others are properly interior. Point $(0, 3\Delta s)$ is a corner edge-interior patch center for which $J_x(0, 3\Delta s, k\Delta t) = 0$ and $J_y(0, 3\Delta s, k\Delta t) = 0$ for all k. Point $(2\Delta s, 0)$ is a bottom edge-interior patch center for which $J_x(2\Delta s, 0) = 3J_x(2\Delta s, \Delta s)$ and $J_y(2\Delta s, 0) = 0$ for all k.

Extrapolation for $\vec{J}$ at point $(m\Delta s, n\Delta s)$ near the right-hand edge of the rectangle in Fig. 49(b) will be demonstrated as a typical example of the procedure. For this particular edge interior patch center:

$$J_{\perp}(m\Delta s, n\Delta s, k\Delta t) = J_x(m\Delta s, n\Delta s, k\Delta t) = 0$$

and

$$J_{/\!/}(m\Delta s, n\Delta s, k\Delta t) = J_y(m\Delta s, n\Delta s, k\Delta t) = \frac{K}{\left(\frac{\Delta s}{2}\right)}$$

for any integer $k \geq 0$. Constant K for this point is obtained from the knowledge of $\vec{J}$ at neighboring patch center $(m\Delta s - \Delta s, n\Delta s)$ to the immediate left of $(m\Delta s, n\Delta s)$. Also, it is assumed that the hyperbolic behavior of $J_{/\!/}$ extends at least a distance $3\Delta s/2$ from the edge of the rectangle. Thus

$$J_y(m\Delta s - \Delta s, n\Delta s, k\Delta t) = \frac{K}{\rho(m\Delta s - \Delta s, n\Delta s)} = \frac{K}{(3\Delta s/2)} \quad .$$

This indeed provides an estimate for K because $(m\Delta s - \Delta s, n\Delta s)$ is a properly interior point and therefore $J(m\Delta s - \Delta s, n\Delta s, k\Delta t)$ has been computed earlier in this iteration. Using K computed from the above gives

$$J_y(m\Delta s, n\Delta s, k\Delta t) = \frac{\left(\frac{3\Delta s}{2}\right) J_y(m\Delta s - \Delta s, n\Delta s, k\Delta t)}{\left(\frac{\Delta s}{2}\right)} = 3J_y(m\Delta s - \Delta s, n\Delta s, k\Delta t) \quad .$$

Of course, $\vec{J}$ at an interior patch center near another edge of the rectangle is computed analogously. For example, for $(m\Delta s, n\Delta s)$ near the bottom edge

$$J_{\perp}(m\Delta s, n\Delta s, k\Delta t) = J_y(m\Delta s, n\Delta s, k\Delta t) = 0 \quad ,$$

and

$$J_{/\!/}(m\Delta s, n\Delta s, k\Delta t) = J_x(m\Delta s, n\Delta s, k\Delta t) = 3J_x(m\Delta s, n\Delta s + \Delta s, k\Delta t)$$

for any integer $k \geq 0$.

In general then, Eqs. (57) and (58) are, for an edge-interior patch center, replaced by

$$J_{\perp}(m\Delta s, n\Delta s, k\Delta t + \Delta t) = 0 \qquad (57')$$

and

$$J_{/\!/}(m\Delta s, n\Delta s, k\Delta t + \Delta t) = \frac{\sqrt{(m\Delta s - x_e)^2 + (n'\Delta s - y_e)^2}}{\rho(m\Delta s, n\Delta s)} J_{/\!/}(m'\Delta s, n'\Delta s, k\Delta t + \Delta t) \quad , \quad (58')$$

where $(m'\Delta s, n'\Delta s)$ is the nearest neighboring patch center to $(m\Delta s, n\Delta s)$ that is also properly interior to the scattering surface S' ; and where $\sqrt{(m'\Delta s - x_e)^2 + (n'\Delta s - y_e)^2}$ is the distance from $(m'\Delta s, n'\Delta s)$ to (x_e, y_e) , the latter again being the edge point nearest $(m\Delta s, n\Delta s)$. These numbers are dependent only upon the shape of the target and the location of patch centers—they are time independent. In fact, for the rectangle and coordinate system just discussed, it is also true that

$$\sqrt{(m'\Delta s - x_e)^2 + (n'\Delta s - y_e)^2} = \rho(m'\Delta s, n'\Delta s) \quad ,$$

so that the extrapolation for $J_{/\!/}$ as given by Eq. (58') is truly hyperbolic. However, none of these features need hold for an arbitrary pairing of surface and coordinate system. Indeed, this is true even of the rectangle whose edges are not parallel to the x- and y-axes. It is this problem, but only this problem, which requires further attention in simulation of the circular target.

To conclude the discussion for the rectangular target simulation, the four corners are points where the perimeter has no tangent, and therefore parallel and perpendicular directions there are at best ambiguous. For an

edge-interior patch center $(m\Delta s, n\Delta s)$ closest to a corner of the rectangle, Eqs. (57) and (58) are replaced by $\vec{J} = 0$ there; that is:

$$J_{\perp}(m\Delta s, n\Delta s, k\Delta t + \Delta t) = 0 \qquad (57'')$$

and

$$J_{//}(m\Delta s, n\Delta s, k\Delta t + \Delta t) = 0 \quad . \qquad (58'')$$

4.3 THE PARABOLIC CYLINDER

In this section, Eqs. (44), (45) and (46) will be specialized for surfaces possessing cylindrical symmetry. A surface possesses this symmetry if it can be generated by the displacement, orthogonally, of a curve lying in two dimensions into the third dimension. An example of such a shape, having finite extent in all three dimensions, is presented in Fig. 50. There, the cylindrical surface S' is generated by some finite curve segment C' lying in the yz-plane. Most precisely, C' consists of the points (x, y, z) having the form $\big(0, y, g(y)\big)$ for all y in the range $0 \le y \le b$. Function g is given, and for this discussion it must be everywhere differentiable. Special attention will be given to the particular case where g defines a parabola.

Cylindrical surface S' , then, consists of all points (x, y, z) having the form $\big(x, y, g(y)\big)$ for all x and y in the ranges $0 \le x \le a$ and $0 \le y \le b$. The parabolic cylinder to receive particular attention herein is generated by a parabola $g(y) = Gy^2$ for some positive real number G that is fixed for any given surface, for all y in the range $-b \le y \le b$. This particular class of parabolic cylinders passes through the x-axis and is symmetric with respect to the xz-plane. Figure 51 shows such a parabolic cylinder together with a fourth coordinate, the u-axis. The x- and u-axes are a particularly convenient orthogonal coordinate pair with which to specialize Eq. (49). Generally, if the u-axis is made to pass through the curve

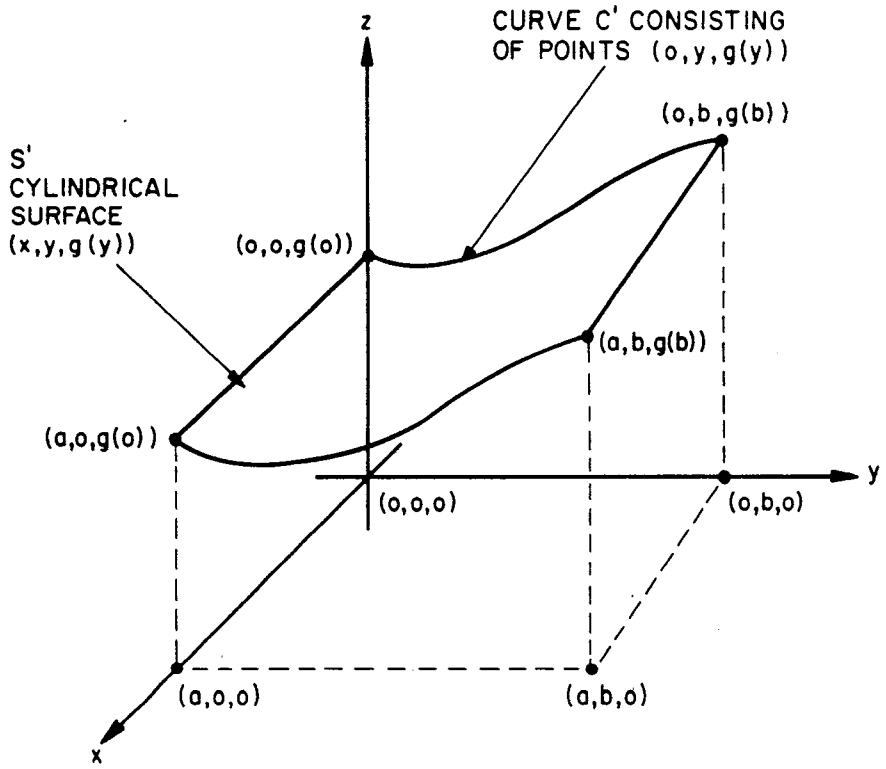

FIG. 50 A surface S' possessing cylindrical symmetry generated by segment C'.

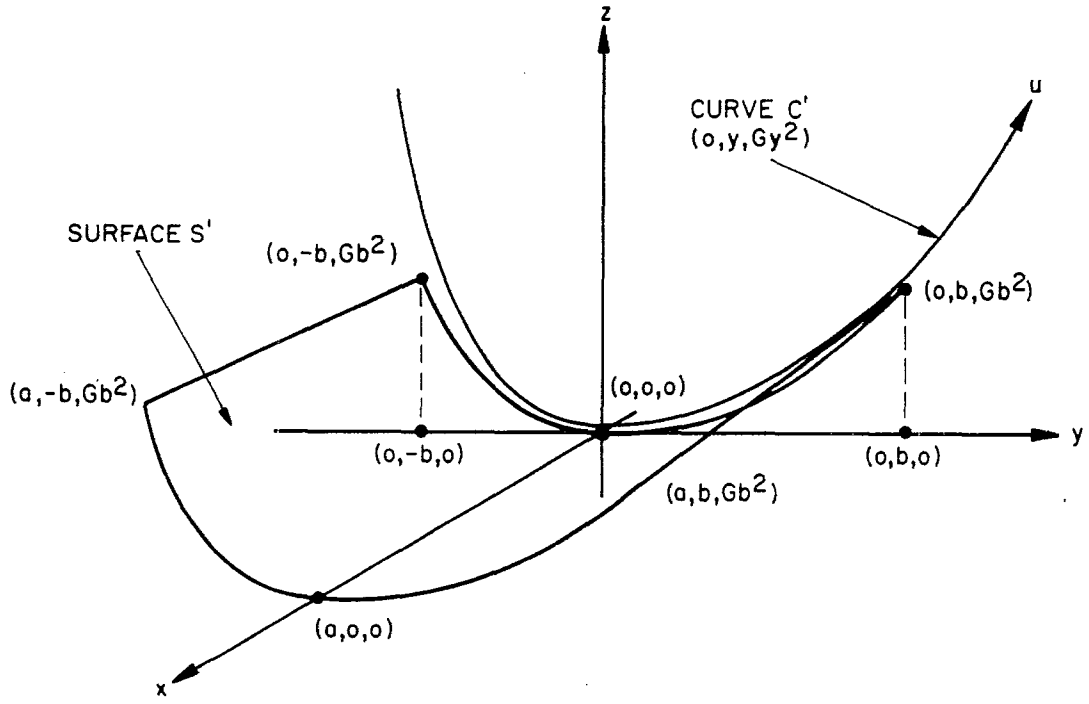

FIG. 51 A parabolic cylinder S' generated by segment of parabola C' .

$\left(0, y, g(y)\right)$ for all real y and if distance on the u-axis is defined appropriately, then the form of the Eq. (49) is preserved; i.e., the equations in x and u corresponding to those in Eq. (49) are obtained by replacing every occurrence of y in Eq. (49) with u, whether that occurrence be as a subscript or as a differential. Indeed, with distance along the u-axis as defined below, the "degenerate" case $g = 0$ yields a generating curve C' that is coincident with the y-axis, so that the u-axis is identical to the y-axis for this case.

Distance along the u-axis is the arc-length, parallel to the yz-plane, measured from the x-axis. Thus, a point $\left(x, y, g(y)\right)$ on the surface is specified in xu-coordinates by (x, u) where $u = h(y) = \int_0^y \sqrt{1 + \left(g'(\xi)\right)^2}\, d\xi$ with g' designating the first derivative of g. This is summarized by writing $\left(x, y, g(y)\right) \Leftrightarrow \left(x, h(y)\right)$, which expresses the correspondence — it is not an equality — of the ordinates in different systems for the same point in physical space.

Since every point $\vec{r}$ on S' can be specified by the ordered pair (x, u), it is convenient to let h^* designate the function relating the u-component of any point $\vec{r}$ on S' to the y-component of that same point. In other words, h^* is the inverse of h defined above, provided this inverse is in fact a function. For the class of parabolas under special consideration here, u increases monotonically with y over the entire range $-\infty < y < +\infty$ regardless of the fixed positive G. Thus the correspondence between u and y is one-to-one, and it follows that h^* is a well defined function for each parabola. Appendix 8.2 shows how, for the u-component of a given point $\vec{r}$ on S', the y-component $y = h^*(u)$ can be computed from the transcendental Eq. (59) below.

If $y = 0$, then $u = 0$ and for all $y \neq 0$, u takes on the sign of y. This sign defines the sense of a u-direction; at surface point $(x_o, u_o) \Leftrightarrow \left[x_o, h^*(u_o), g\left(h^*(u_o)\right)\right]$, the u-direction is parallel to the yz-plane and makes an angle $\arctan\left[g'\left(h^*(u_o)\right)\right]$ with the y-axis. Letting $h^*(u_o) = y_o$ so that $\left[x_o, h^*(u_o), g\left(h^*(u_o)\right)\right] = \left(x_o, y_o, g(y_o)\right)$, this angle then can also be expressed as $\arctan\left(g'(y_o)\right)$. The direction perpendicular

to S' at any point will be designated the p-direction. Its sense is such as to make x, u, p a local right-hand coordinate system at the point.

The preceding definitions will here be specialized for the parabolic cylinder. Beginning with $g(y) = Gy^2$, $G \geq 0$ fixed, it follows that $g'(y) = 2Gy$ for all y . Therefore

$$u = h(y) = \int_0^y \sqrt{1 + (2G\xi)^2}\, d\xi = \frac{y}{2}\sqrt{1 + (2Gy)^2} + \frac{1}{4G}\, \ell n\left(2Gy + \sqrt{1 + (2Gy)^2}\right) \quad (59)$$

for all $y \geq 0$. Symmetry of the parabola implies that for $y < 0$, $u = h(y) = -h(-y)$.

Observe that $G = 0$ implies that the parabolic cylinder "degenerates" to a rectangle of sides $2b$ by a , lying in the xy-plane. Also, taking the limit in Eq. (59):

$$\lim_{G \to 0} u(y) = \frac{y}{2} + \frac{y}{2} = y$$

for all y . This bears out an earlier observation that if function g is the zero function, the u-axis does indeed degenerate into the y-axis.

Returning to the more general case of arbitrary g , with the orthogonal x- and u-axes Eq. (45) can be specialized immediately to

$$J_x(x, u, t) \approx \frac{\pi}{\delta \cdot \ell n(1 + \sqrt{2})} A_x'(x, u, t) \quad ,$$

$$J_u(x, u, t) \approx \frac{\pi}{\delta \cdot \ell n(1 + \sqrt{2})} A_u'(x, u, t) \quad ,$$

and

$$J_p(x, u, t) = 0 \quad (60)$$

for all time t and each point $\vec{r}$ given by (x, u) on the cylindrical surface S'. Here, $J_u(\vec{r}, t)$ is the component of $\vec{J}(\vec{r}, t)$ in the u-direction. If the u-axis is not identical to the y-axis, then the direction of J_u depends on $\vec{r}$, but regardless of g and $\vec{r}$, J_u is always perpendicular to J_x and parallel to the yz-plane. Furthermore, $J_p(\vec{r}, t)$, the component of $\vec{J}(\vec{r}, t)$ perpendicular to the cylindrical surface S', vanishes for all g, not just for the rectangular surface $g = 0$.

In xu-coordinates, Eq. (44) specializes, as in the rectangular case, to

$$A''_x(\vec{r}, t) = \frac{1}{4\pi} \int_{S' - S'_{\vec{r}}} \frac{J_x\left(\vec{r}, t - \frac{|\vec{r} - \vec{r}'|}{c}\right)}{|\vec{r} - \vec{r}'|} \, dS'$$

where the distance $|\vec{r} - \vec{r}'|$ is <u>not</u> some curvilinear distance measured over the surface S', but is rather the Euclidean "line-of-sight" distance between points $\vec{r}$ and $\vec{r}'$. For $\vec{r}$ and $\vec{r}'$ both on S' (i.e., given by (x, u) and (x', u') respectively):

$$|\vec{r} - \vec{r}'| = |(x, u) - (x', u')| = \sqrt{(x - x')^2 + \left(h^*(u) - h^*(u')\right)^2 + \left[g\left(h^*(u)\right) - g\left(h^*(u')\right)\right]^2} \, .$$

Since the cylinder extends from $h(-b)$ to $h(b)$ along the u-axis and from 0 to a along the x-axis, the preceding surface integral specializes to

$$A''_x(x, u, t) = \frac{1}{4\pi} \int_0^a \int_{h(-b)}^{h(b)} \frac{J_x\left(x, u, t - \frac{|(x, u) - (x', u')|}{c}\right)}{|(x, u) - (x', u')|} \, du' \, dx' \quad (61)$$

for every (x, u) on S'.

Equation (44) cannot be specialized for $A''_u(\vec{r}, t)$ as quickly as it was for $A''_x(\vec{r}, t)$ because, in general, direction u at $\vec{r}$ does not coincide

with direction u' at $\vec{r}'$. Rather, for any $\vec{r}$ on S' the specialization must be obtained from $A''_u(\vec{r}, t) = A''_y(\vec{r}, t)\cos\theta(\vec{r}) + A''_z(\vec{r}, t)\sin\theta(\vec{r})$ for all time t, where

$$A''_y(\vec{r}, t) = \frac{1}{4\pi}\int_{S'-S'_{\vec{r}}} \frac{J_y\left(\vec{r}', t - \frac{|\vec{r}-\vec{r}'|}{c}\right)}{|\vec{r}-\vec{r}'|}\, dS'$$

$$A''_z(\vec{r}, t) = \frac{1}{4\pi}\int_{S'-S'_{\vec{r}}} \frac{J_z\left(\vec{r}, t - \frac{|\vec{r}-\vec{r}'|}{c}\right)}{|\vec{r}-\vec{r}'|}\, dS'$$

and $\theta(\vec{r}) = \theta(x, u) = \arctan\left[g'\left(h^*(u)\right)\right]$. Figure 52 illustrates the situation; it is apparent that for all $\vec{r}$ on S' and for all time t,

$$J_y(\vec{r}, t) = J_u(\vec{r}, t)\cos\theta(\vec{r}) \quad ,$$

and

$$J_z(\vec{r}, t) = J_u(\vec{r}, t)\sin\theta(\vec{r}) \quad .$$

Using these relationships in the two kernels and then combining them gives

$$A''_u(\vec{r}, t) = \frac{1}{4\pi}\int_{S'-S'_{\vec{r}}} \frac{J_{u'}\left(\vec{r}', t - \frac{|\vec{r}-\vec{r}'|}{c}\right)}{|\vec{r}-\vec{r}'|} \cdot \cos\left(\theta(\vec{r}) - \theta(\vec{r}')\right) \cdot dS' \quad .$$

That is, for $\vec{r}$ and $\vec{r}'$ given by (x, u) and (x', u') respectively:

$$A''_u(x, u, t) = \frac{1}{4\pi}\int_0^a \int_{h(-b)}^{h(b)} \frac{J_{u'}\left(x, u, t - \frac{|(x, u)-(x', u')|}{c}\right)}{|(x, u)-(x', u')|} \cdot \cos\left(\theta(x, u) - \theta(x', u')\right) du'\, dx' \qquad (62)$$

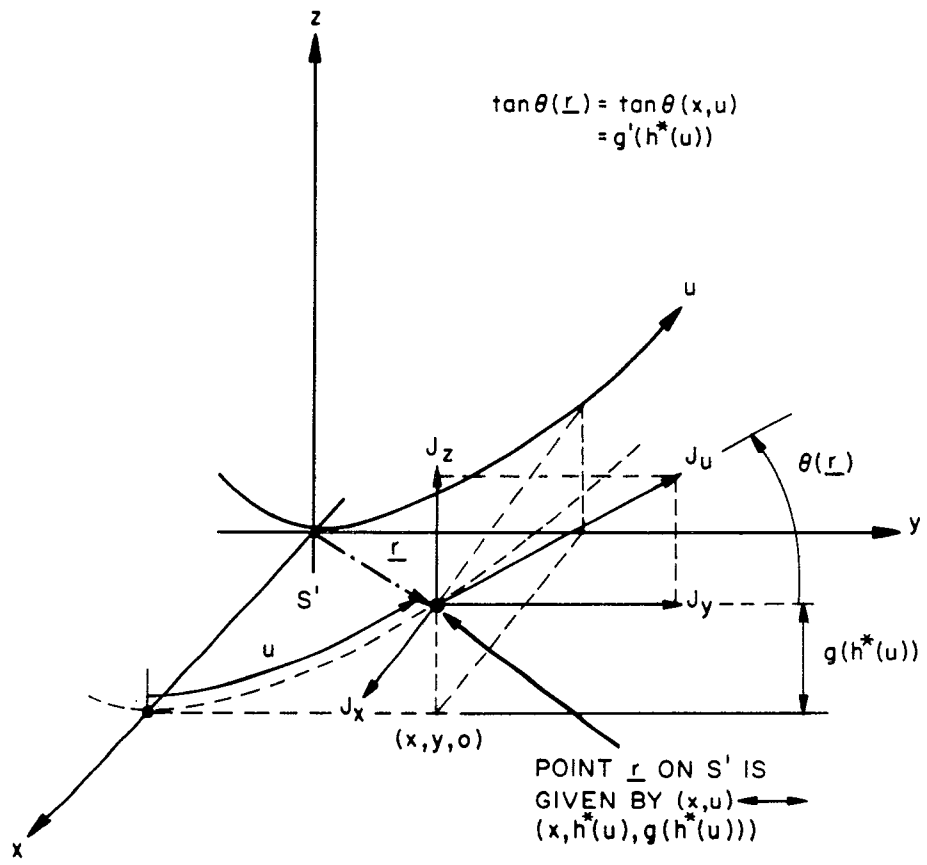

FIG. 52 Surface S' with current density $\vec{J}$ resolved for the computations in Eq. (62).

for all time t and all (x, u) on S' .

Finally, Eq. (44) must also be specialized for $A''_p(\vec{r}, t)$; unlike flat scattering surfaces, it does not vanish. In fact,

$$A''_p(\vec{r}, t) = -A''_y(\vec{r}, t) \sin\theta(\vec{r}) + A''_z(\vec{r}, t) \cos\theta(\vec{r}) \quad .$$

Using the same relationships leading to Eq. (62),

$$A''_p(\vec{r}, t) = \frac{1}{4\pi} \int_{S'-S'_{\vec{r}}} \frac{J_{u'}\left(\vec{r}', t - \frac{|\vec{r} - \vec{r}'|}{c}\right)}{|\vec{r} - \vec{r}'|} \cdot \sin\left(\theta(\vec{r}') - \theta(\vec{r})\right) dS'$$

at every point $\vec{r}$ on S' and for all time t .

It remains only to specialize Eq. (46) for the x- and u-axes. For any vector field $\vec{F}$ and scalar field f whose spatial derivatives all exist,*

$$\vec{\nabla} \cdot \vec{F} = \frac{\partial F_x}{\partial x} + \frac{\partial F_u}{\partial u} + \frac{\partial F_p}{\partial p}$$

and

$$\vec{\nabla} f = \left(\frac{\partial f}{\partial x}, \frac{\partial f}{\partial u}, \frac{\partial f}{\partial p}\right) \quad .$$

Applying the latter to $f = \vec{\nabla} \cdot \vec{F}$ gives

$$\vec{\nabla}(\vec{\nabla} \cdot \vec{F}) = \left(\frac{\partial^2 F_x}{\partial x^2} + \frac{\partial^2 F_u}{\partial x \partial u} + \frac{\partial^2 F_p}{\partial x \partial p}, \frac{\partial^2 F_x}{\partial x \partial u} + \frac{\partial^2 F_u}{\partial u^2} + \frac{\partial^2 F_p}{\partial u \partial p}, \frac{\partial^2 F_x}{\partial x \partial p} + \frac{\partial^2 F_u}{\partial u \partial p} + \frac{\partial^2 F_p}{\partial p^2} \right) \quad .$$

---

*Recall that both Δx and Δu are arclengths along the x- and u-axes respectively. The p-direction has been defined only where it is needed, namely at S' . There, Δp can be defined as an arclength in the direction perpendicular to S' ; its magnitude is small compared to the minimum radius of curvature of curve segment C' .

The tangential directions in Eqs. (46) are x and u, so the specialization becomes

$$\frac{1}{c^2}\frac{\partial^2 A_x'}{\partial t^2} = \epsilon_o \frac{\partial E_x^i}{\partial t} - \frac{1}{c^2}\frac{\partial^2 A_x''}{\partial t^2} + \frac{\partial^2 A_x'}{\partial x^2} + \frac{\partial^2 A_u'}{\partial x \partial u} + \frac{\partial^2 A_p'}{\partial x \partial p} + \frac{\partial^2 A_x''}{\partial x^2} + \frac{\partial^2 A_y''}{\partial x \partial u} + \frac{\partial^2 A_p''}{\partial x \partial p}$$

and

$$\frac{1}{c^2}\frac{\partial^2 A_u'}{\partial t^2} = \epsilon_o \frac{\partial E_u^i}{\partial t} - \frac{1}{c^2}\frac{\partial^2 A_u''}{\partial t^2} + \frac{\partial^2 A_x'}{\partial x \partial u} + \frac{\partial^2 A_u'}{\partial u^2} + \frac{\partial^2 A_p'}{\partial u \partial p} + \frac{\partial^2 A_x''}{\partial x \partial u} + \frac{\partial^2 A_u''}{\partial u^2} + \frac{\partial^2 A_p''}{\partial u \partial p} \quad .$$

In Appendix 8.3 it is shown that the boundary condition

$$\frac{\partial A_p'}{\partial p} + \frac{\partial A_p''}{\partial p} = 0$$

at S' can be imposed without violating the consistency of previous equations involving $\vec{A} = \vec{A}' + \vec{A}''$. Thus $\frac{\partial^2 A_p'}{\partial x \partial p} + \frac{\partial^2 A_p''}{\partial x \partial p}$ and $\frac{\partial^2 A_p'}{\partial u \partial p} + \frac{\partial^2 A_p''}{\partial u \partial p}$ both vanish, yielding

$$\frac{1}{c^2}\frac{\partial^2 A_x'}{\partial t^2} = \epsilon_o \frac{\partial E_x^i}{\partial t} - \frac{1}{c^2}\frac{\partial^2 A_x''}{\partial t^2} + \frac{\partial^2 A_x'}{\partial x^2} + \frac{\partial^2 A_y'}{\partial x \partial u} + \frac{\partial^2 A_x''}{\partial x^2} + \frac{\partial^2 A_u''}{\partial x \partial u} \quad ,$$

and

$$\frac{1}{c^2}\frac{\partial^2 A_u'}{\partial t^2} = \epsilon_o \frac{\partial E_u^i}{\partial t} - \frac{1}{c^2}\frac{\partial^2 A_u''}{\partial t^2} + \frac{\partial^2 A_x'}{\partial x \partial u} + \frac{\partial^2 A_u'}{\partial u^2} + \frac{\partial^2 A_x''}{\partial x \partial u} + \frac{\partial^2 A_u''}{\partial u^2} \qquad (63)$$

valid always and everywhere on S'.

Comparison of Eq. (60) giving $\vec{J}$ on the cylindrical surface with Eq. (47) for the infinite plane reveals that Eq. (60) can be obtained from Eq. (47) by substituting u for every occurrence of y in Eq. (47), and p

for every occurrence of z . Wave equations (63) are similarly obtainable from those in Eq. (49), as is Eq. (61) from Eq. (48) for A''_x . Of course, in Eqs. (48) and (61) the limits of integration are essentially different; they would in fact also carry over if Eq. (48) were a specialization for the rectangle rather than the infinite plane: then the limits would be common to both specializations because $h(y) = y$ for all y if $G = 0$; in particular $h(b) = b$ and $h(-b) = -b$. And finally, A''_u in Eq. (62) is obtainable from A''_y in Eq. (48) using the above letter substitutions if a trigonometric factor is also introduced into the kernel for A''_u . (The factor reduces to unity for all planar scattering surfaces.)

It follows then that all of the digital processing equations developed for the rectangular scattering surface have the same form for the cylindrical scattering surface, with two exceptions. One is that $|\vec{r} - \vec{r}'|$, which occurs in the double summations for A''_x and A''_u , must now be computed by considering all three Cartesian components of $\vec{r}$ and $\vec{r}'$ instead of just the two components as in Eqs. (50) and (52) for A''_x and A''_y . The other exception is that the trigonmetric factor must be included in the double summation for A''_u . Neither of these exceptions presents difficulties for quantizing, so the processing equations for the cylinder need not be rewritten here.

The iterative process for the cylinder is identical to that described for the rectangle, including the treatment of edges and corners since, locally, the edge of a region of a curved surface approaches that of a plane surface.

To conclude the discussion of the cylindrical scattering surface, the above mentioned trigonmetric factor is derived below. This factor in the kernel of Eq. (62) is equivalent to $\cos\theta(x, u) \cdot \cos\theta(x', u') + \sin\theta(x, u) \cdot \sin\theta(x', u')$. Let y designate the y-component of the point $(x, u) \Leftrightarrow \left[x, h^*(u), g\left(h^*(u)\right)\right] = \left(x, y, g(y)\right)$. Recall that $\tan\theta(x, u) = g'(y)$, so that

$$\cos\theta(x, u) = 1/\sqrt{1 + \left(g'(y)\right)^2}$$

and

$$\sin\theta(x, u) = g'(y)/\sqrt{1+\left(g'(y)\right)^2} \quad .$$

Performing the same calculations for (x', u') and combining yields

$$\cos\Big(\theta(x, u) - \theta(x', u')\Big) = \frac{1 + g'\Big(h^*(u)\Big) \cdot g'\Big(h^*(u')\Big)}{\sqrt{\Big[1+\Big[g'\Big(h^*(u)\Big)\Big]^2\Big]\Big[1+\Big[g'\Big(h^*(u')\Big)\Big]^2\Big]}} \cdot$$

4.4 EXPERIMENTAL VERIFICATION

In time domain measurements made on the Sperry Research Center scattering range, the observation point was selected at a distance that was much larger than the longest dimension on the scatterer. Again choosing a coordinate system with its origin centered on the scattering surface, this is equivalent to saying that for the observation point $\vec{r}$, $|\vec{r}| >> |\vec{r}'|$ for all $\vec{r}'$ on S' . For this situation, Eq. (27), which gives the magnetic field vector $\vec{H}^s$ scattered back to $\vec{r}$, can be simplified by employing the approximation

$$|\vec{r} - \vec{r}'| \approx |\vec{r}| \quad \text{for all} \quad \vec{r}' \text{ on } S' \quad .$$

Employing this approximation in Eq. (27) gives

$$\vec{H}^s(\vec{r}, t) = \frac{1}{4\pi|\vec{r}|^2} \int_{S'} \vec{J}\Big(\vec{r}', t - \frac{|\vec{r} - \vec{r}'|}{c}\Big) \times \frac{\vec{r}}{|\vec{r}|}\, dS'$$

$$+ \frac{1}{c4\pi|\vec{r}|} \int_{S'} \frac{\partial \vec{J}}{\partial t}\Big(\vec{r}', t - \frac{|\vec{r} - \vec{r}'|}{c}\Big) \times \frac{\vec{r}}{|\vec{r}|}\, dS' \quad .$$

The first integral is inversely proportional to $|\vec{r}|^2$, whereas the second is inversely proportional to $|\vec{r}|$. Thus, for $|\vec{r}|$ sufficiently great the first can be neglected altogether. The relation finally used to compute this far-field $\vec{H}^{sf}$ from $\vec{J}$ for comparing the computing total field $\vec{H}^t$ with the measured $\vec{H}^t$ is

$$\vec{H}^{sf}(\vec{r}, t) = \frac{1}{4\pi c|\vec{r}|} \int_{S'} \frac{\partial \vec{J}}{\partial t}\left(\vec{r}', t - \frac{|\vec{r} - \vec{r}'|}{c}\right) \times \left(\frac{\vec{r}}{|\vec{r}|}\right) dS' \qquad (64)$$

which is valid for all time t at any point $\vec{r}$ sufficiently distant from S' to permit the approximation $|\vec{r} - \vec{r}'| \approx |\vec{r}|$ for all $\vec{r}'$ on S'.

Figures 53 through 56 are plots of backscattered magnetic field data for the three target shapes considered in this report. Each plot compares the data computed from the simulation of a specific target with measured range data from a target of the same shape. The measured data were obtained on the time domain scattering range discussed in Sec. 3 of this report. The plotted range data have been scaled in distance to account for differences in dimensions between the actual and simulated targets. The data were also processed to account for the difference in forcing functions generated by the actual and hypothesized transmitters.

In all four plots the abscissa represents time; more precisely, the quantity plotted is ct, which is measured in meters. When measuring time in this manner the unit is referred to as a light-meter, so an event of duration p in light-meters is also the time in seconds that it takes light to travel a distance of p meters.

All simulations assumed an incident plane wave whose time variation was a smoothed (Gaussian) impulse. In other words, at time t the amplitude was proportional to $e^{-(a_N ct)^2}$, where for each of the four runs presented here $a_N = 1$ inverse light-meters was chosen. More precisely, the variation $e^{-(a_N ct)^2}$ applies to the origin of the spatial coordinates. In every case this origin was located on the scattering surface S' at a point referred to as the "center" of the target. Thus, for the purpose of these plots, and contrary to the convention adopted in previous sections, $ct = 0$ now marks

the time when the peak of the incident smoothed impulse strikes the center of the target. In general then, the time variation of the incident plane wave at an arbitrary point (x, y, z) in space is proportional to $e^{-(a_N ct - z)^2}$.

The ordinate in Figs. 53-56 plots the normalized component of the magnetic field which is scattered back to the receiver. Specifically, the plotted quantity is

$$H_i^{sf}(\vec{R}, t) = |\vec{R}| \frac{\vec{H}^i(\vec{R}, 0)}{|\vec{H}^i(\vec{R}, 0)|} \cdot \vec{H}^{sf}(\vec{R}, t)$$

where $\vec{H}^{sf}(\vec{R}, t)$ for any time t is the far scattered magnetic field given in Eq. (64) for the point $\vec{r} = \vec{R}$, the location of the transmitter. Thus $|\vec{R}|$ is the distance of the transmitter from the center of the target. Appearance of the dot-product $\vec{H}^{sf}(\vec{R}, t)$ with the vector $\frac{\vec{H}^i(\vec{R}, 0)}{|\vec{H}^i(\vec{R}, 0)|}$ of unit magnitude, implies that $H_i^{sf}(\vec{R}, t)$ is the component of $\vec{H}^{sf}(\vec{R}, t)$ having the same direction as the incident field $\vec{H}^i(R, 0)$ at the receiver site. In the MKS system, magnetic field $\vec{H}$ is measured in amperes/meter; it follows that the plotted quantity H_i^{sf} is measured in amperes.

Also common to the four simulations was the size of the patch: side $\Delta s = 0.25$ meters in all of the figures. The time increment $c\Delta t = 0.20$ light-meters was common as well. This choice complies with the condition $c\Delta t \leq \Delta s$ discussed in Sec. 4.1.

Figures 53 and 54 present the far reflections measured on the scattering range from a square surface 8 inches on a side. Sides of the simulated square were each $10\Delta s$ and $\vec{J}$ was computed at the centers of 100 patches. In both simulations, $\vec{H}^i$ was parallel to one of the edges of the target. Incident angles (measured between $\vec{H}^i$ and the direction normal to the plane of the surface S') were 0° and 45° in Figs. 53 and 54 respectively.

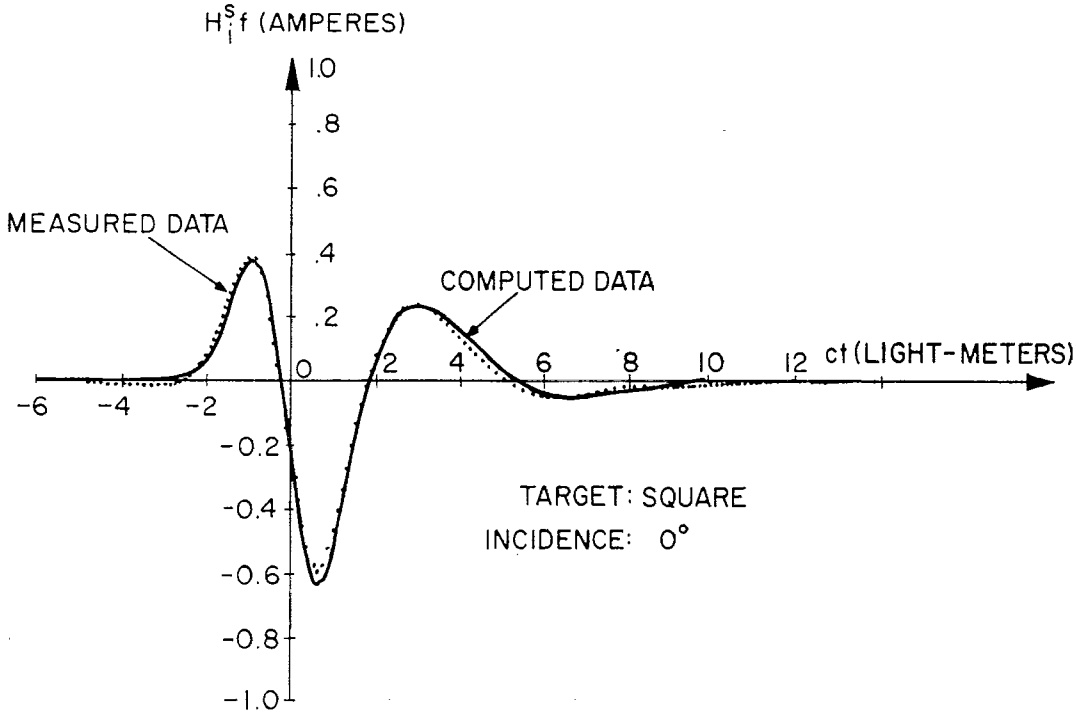

FIG. 53 Comparison of measured and computed backscattered magnetic field for 8" x 8" square target at 0^o incidence.

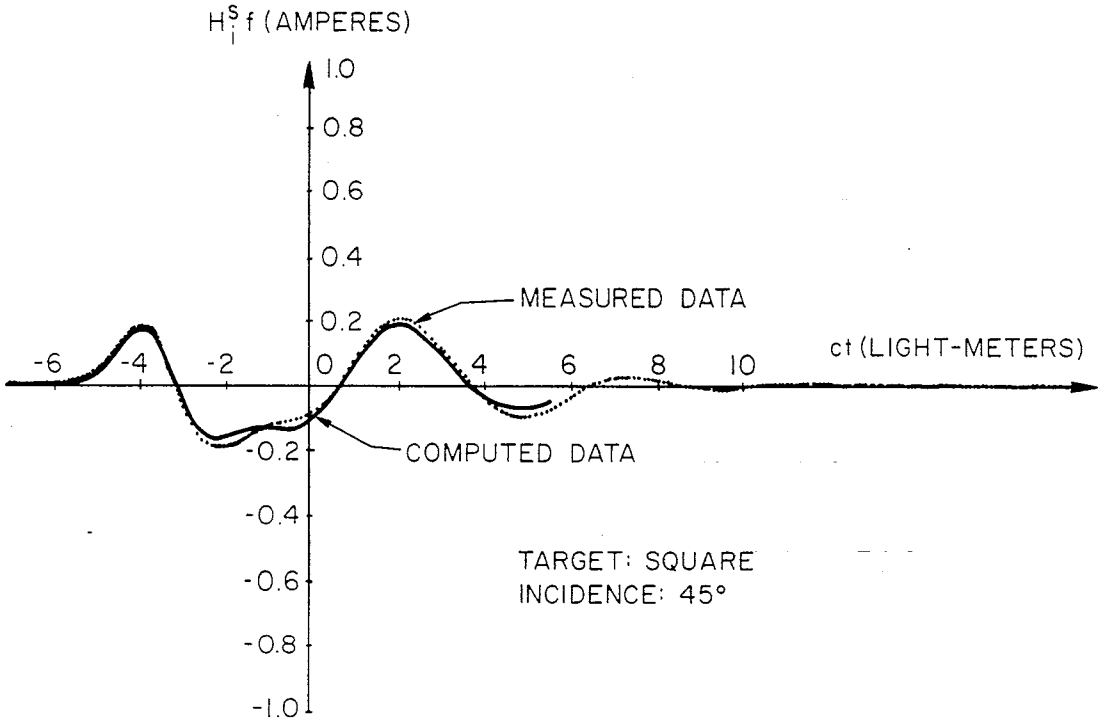

FIG. 54 Comparison of measured and computed backscattered magnetic field for 8"× 8" square target at 45° incidence.

Figure 55 presents the far reflections measured on the scattering range from a disc 8 inches in diameter. The diameter of the circle in the simulation was $8\Delta s$ and $\vec{J}$ was computed at the centers of 56 patches. Incidence was perpendicular to the plane of the disc (i.e., the plane wave was parallel to the disc itself).

To date, simulation of the disc has not yet been perfected. In the simulation plotted in Fig. 55, the target's circumference was approximated by a staircase-shaped curve; that is, the square patches near the circumference were either entirely included or entirely excluded from the processing, depending on whether the patch center was or was not inside the circle, respectively. Refinement of this procedure will further improve the accuracy of the simulation at times prior to about $ct = 4$ light-meters.

At about 4 light-meters an oscillation in the simulated magnetic field becomes apparent; its amplitude increases with time thereafter. This instability is due to problems of numerical approximations in the edge region of the circle. As mentioned at the conclusion of Sec. 4.2, there are difficulties in implementing the hyperbolic extrapolation technique at points on the circumference where the tangent is parallel to neither the x- nor the y-axis. This problem has not yet been entirely solved.

Figure 56 compares a computed reflection with a measured reflection from a parabolic cylinder. With reference to Fig. 51, the dimensions of the cylindrical target measured in the scattering range were $a = 8$ inches deep, $2b = 8$ inches wide at the throat, and the edges of the throat rise $Gb^2 = 2$ inches above the bottom of the cylinder (i.e., above xy-plane). Thus, $b = 4$ inches and the parabolic constant $G = 2/4^2 = 1/8$.

The dimensions of the simulated cylinder were: depth $a = 8\Delta s$; width, as measured along the u-axis, $2h(4) = 9\Delta s$. Current density $\vec{J}$ was computed at the centers of 72 patches. With reference again to Fig. 51, the plane wave assumed in the simulation was incident in the -z direction, with $\vec{H}^i$ parallel to the y-axis.

For the cylinder, as for the rectangle, hyperbolic extrapolation at the edges works well, and the solution is both accurate and numerically stable.

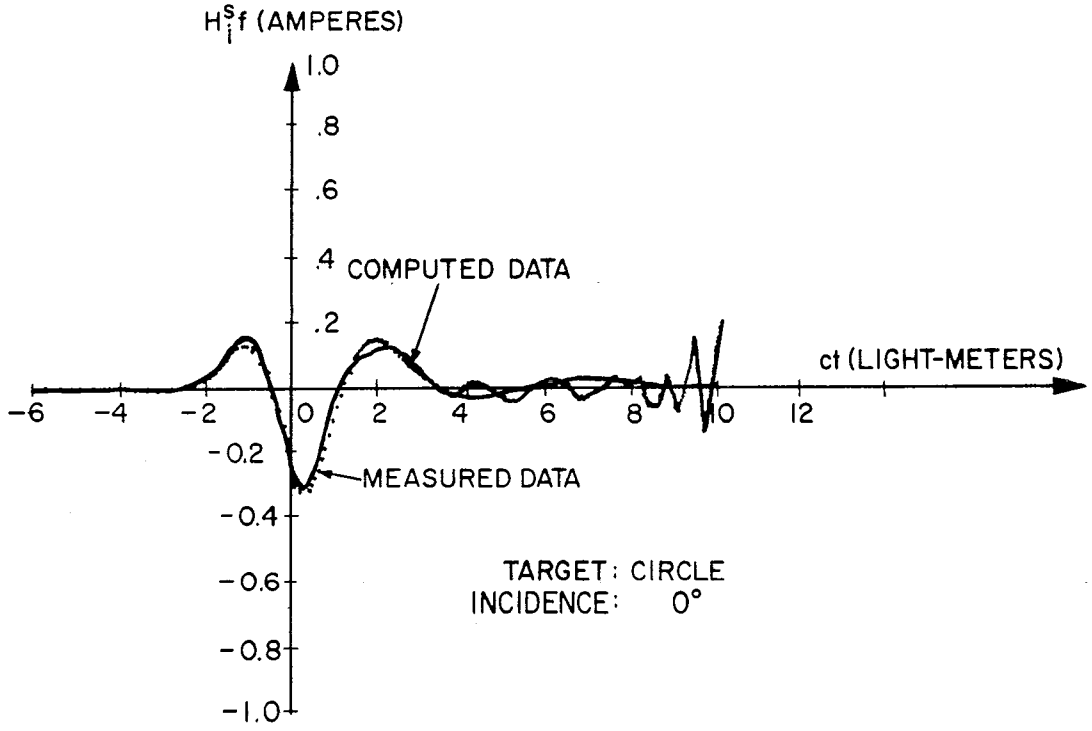

FIG. 55 Comparison of measured and computed backscattered magnetic field for an 8" disk at 0^o incidence.

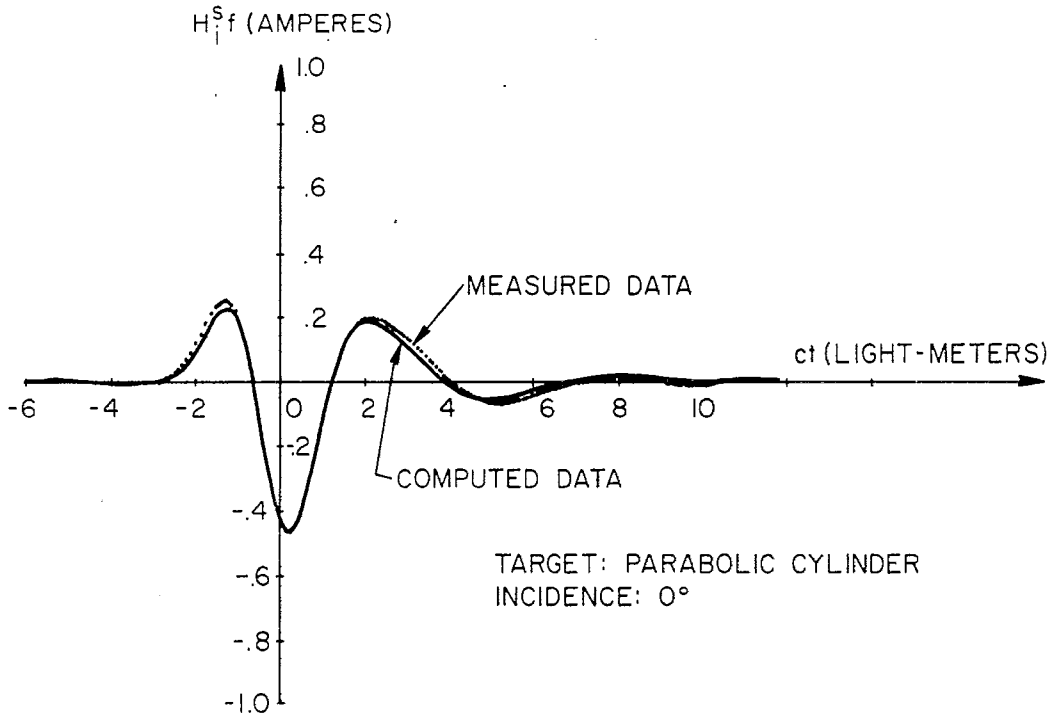

FIG. 56 Comparison of measured and computed backscattered magnetic field for a parabolic cylinder (a = 8", 2b = 8") at 0° incidence.

SECTION 5
TIME DOMAIN APPROACH TO INVERSE SCATTERING
(R. Hieronymus, J. DeLorenzo, and C. L. Bennett)

5.1 DEVELOPMENT OF SPACE-TIME INVERSION EQUATION

As early as 1958, researchers[10] knew that if physical optics currents are postulated on the surface of a scatterer, then they produce an approximate impulse response that is simply the second derivative of the projected area function of the target. It follows, according to this approximate theory, that the ramp response is proportional to the area function which can then be related to the linear dimensions of the scattering object. Many researchers have developed schemes for obtaining target geometry from the area function using the physical optics approximations.[11,12] The results of these studies have produced reasonable approximations to the target geometry.

In this study, the inverse scattering problem is formulated as an inversion of the space-time integral equation. This technique shows (as expected from the asymptotic nature of the physical optics solution) that the relation between the impulse response and two derivatives of the area function is exact only at the leading edge of the scattered field response, a single point in time. After the leading edge, the response is altered by currents arriving from other space points. Therefore, the physical optics solution must be "corrected" by these currents flowing on the body. For a given object, if the incident pulse width is short compared to body size (the optical limit) then the correction currents will have a small effect, and optical rays can be placed in one-to-one correspondence with points on the body. On the other hand, if the size of the body is comparable to a pulse width, then the "correction" terms have a strong effect on the solution and the physical optics solution is degraded. In the case of small bodies, the correction terms dominate the result and the physical optics solution is meaningless.

5.1.1 Derivation of General Equation

The derivation of the inversion procedure begins with the exact expression for the surface currents, namely

$$\vec{J}(\vec{r}, t) = 2\hat{a}_n \times \vec{H}^i(\vec{r}, t) + \vec{J}_c(\vec{r}, t)$$

where

$$\vec{J}_c(\vec{r}, t) = \frac{1}{2\pi} \int_S \hat{a}_n \times \left\{ \left[\frac{1}{R^2} + \frac{1}{R} \frac{\partial}{\partial \tau} \right] \vec{J}(\vec{r}', \tau) \times \hat{a}_R \right\} dS' \quad (65)$$

$$\tau = t - R$$

$\vec{H}^i(\vec{r}, t)$ = incident magnetic field

$\hat{a}_n$ = unit vector normal to surface

$\vec{r}$ = position vector to observation point

$\vec{r}'$ = position vector to integration point

$R = |\vec{r} - \vec{r}'|$

$\hat{a}_R = \dfrac{\vec{r} - \vec{r}'}{R}$

t = time in light-meters.

In the physical optics approximation, only the first term in Eq. (65) is retained. The effect of this approximation then is to neglect the currents $(\vec{J}_c)$ which flow on the surface after the incident field has passed over the object.

The far scattered field of an object, $\vec{H}^s(\vec{r}, t)$, is computed by the quadrature

$$\vec{H}^s(\vec{r}, t) = \frac{1}{4\pi r_o} \frac{\partial}{\partial t} \int \left\{ \vec{J}(\vec{r}', \tau) \times \hat{a}_r \right\} dS' \quad (66)$$

$$\tau = t - R$$

once the surface currents are known. If the currents as expressed by Eq. (65) are used in Eq. (66), the result is

$$r_o \vec{H}^s(\vec{r}, t) = \frac{1}{4\pi} \frac{\partial}{\partial t} \int \left\{ 2\hat{a}_n \times \vec{H}^i(\vec{r}', \tau) \times \hat{a}_r \right\} dS'$$

$$\tau = t - R$$

$$+ \frac{1}{4\pi} \frac{\partial}{\partial t} \int \left\{ \vec{J}_c(\vec{r}', \tau) \times \hat{a}_r \right\} dS' \quad . \qquad (67)$$

$$\tau = t - R$$

If the incident field is an impulse, then the first term in Eq. (67) is simply the quadrature that has been recognized previously[10] to be proportional to the second derivative of the area function. Assuming the incident wave is an electromagnetic impulse, then Eq. (67) becomes

$$r_o \vec{H}_I^s(\vec{r}, t) = \frac{1}{2\pi} \frac{\partial^2 S(t_s)}{\partial t^2} \hat{a}_H + \frac{1}{4\pi} \frac{\partial}{\partial t} \int \left\{ \vec{J}_{cI}(r', \tau) \times \hat{a}_r \right\} dS' \qquad (68)$$

$$\tau = t - R$$

where

$r_o \vec{H}_I^s(\vec{r}, t)$ = the impulse response of the target

$S(t_s)$ = the silhouette area of the scatterer as delineated by the incident impulse assumed moving over the scatterer at one half the free-space velocity

r_o = distance of far-field observer from the origin

$t = t_s + r_o$

$\hat{a}_H = \dfrac{\vec{H}^i}{|\vec{H}^i|}$

$\vec{J}_{cI} = \vec{J}_c$ that results from an incident impulse.

This equation may be simplified by use of the theory of linear systems to obtain

$$r_o \vec{H}_R^s(\vec{r}, t) = \frac{1}{2\pi} S(t_s)\, \hat{a}_H + \frac{1}{4\pi} \frac{\partial}{\partial t} \int_S \left\{ \vec{J}_{cR}(\vec{r}', \tau) \times \hat{a}_r \right\} dS' \qquad (69)$$

$$\tau = t - R$$

where

$r_o \vec{H}_R^s$ = the ramp response of the target

$\vec{J}_{cR} = \vec{J}_c$ that results from an incident ramp waveform.

Thus, by direct consideration of the space-time integral equation the exact relationship between the target response and the target geometry has been obtained. In particular, Eq. (69) gives the target ramp response in terms of both the target area function and the contribution due to the "correction currents," $\vec{J}_c$. Moreover, it is important to note that the correction currents as given in Eq. (65) are time-retarded functions of currents at other space points, and thus will be zero at the leading edge of the incident wavefront as it travels across the target. It is this feature, exclusive to the time domain formulation, that allows the determination of the target geometry from its ramp (or equivalently, impulse) response.

5.1.2 Derivation of Equation for Rotationally Symmetric Objects

The preceding paragraphs developed the exact relation between the ramp response of an object, its projected area function and correction currents. The salient feature of that result is that we can relate the target geometry to a remotely measured parameter, the far-field ramp response. In order to demonstrate the utility of these equations, the remainder of this section will be concerned with the derivation of an inversion procedure for rotationally symmetric targets.

Consider the case of the field backscattered from a target rotationally symmetric about the z-axis with an axially incident ramp waveform as

shown in Fig. 57. The target is completely described by $\rho = \rho(z)$ and the area function is given by

$$S = \pi\rho^2(z, t) \quad . \tag{70}$$

Hence, substituting into Eq. (69) and rearranging yields

$$\rho(z, t) = \left[2r_o H_R^s(\vec{r}, t) - \frac{1}{2\pi} \int_S \left\{ \vec{J}_{cR}(\vec{r}', \tau) \times \hat{a}_r \right\} dS' \right]^{1/2} . \tag{71}$$

This equation gives $\rho(z, t)$ in terms of the target ramp response, which is known, and in terms of the correction currents at earlier times, which have either been previously computed or are known to be zero. An iterative procedure for determining the target geometry parameter $\rho(z, t)$ can now be developed.

It is assumed that a far-field measurement of the ramp response of an object or of some function from which it can be computed has been obtained. The first step in the procedure is to obtain an estimate of ρ from Eq. (71), neglecting the surface integral. With this estimate of ρ, the geometric functions of ρ that are required for the solution of Eq. (65) for the correction currents $\vec{J}_{cR}$ are computed. Once these functions are computed, $\vec{J}_{cR}$ is obtained by numerical solution in Eq. (65). The iteration proceeds with the computation of the second estimate of ρ, another calculation of correction currents, and so on until ρ is determined to the desired accuracy.

A discussion of the implementation of the procedure and examples of its use are presented in the following sections.

5.2 NUMERICAL SOLUTION

The implementation of the iterative procedure for determining the target geometry function $\rho(z, t)$ from its far-field ramp response was carried out using numerical techniques on a digital computer. The core of the method

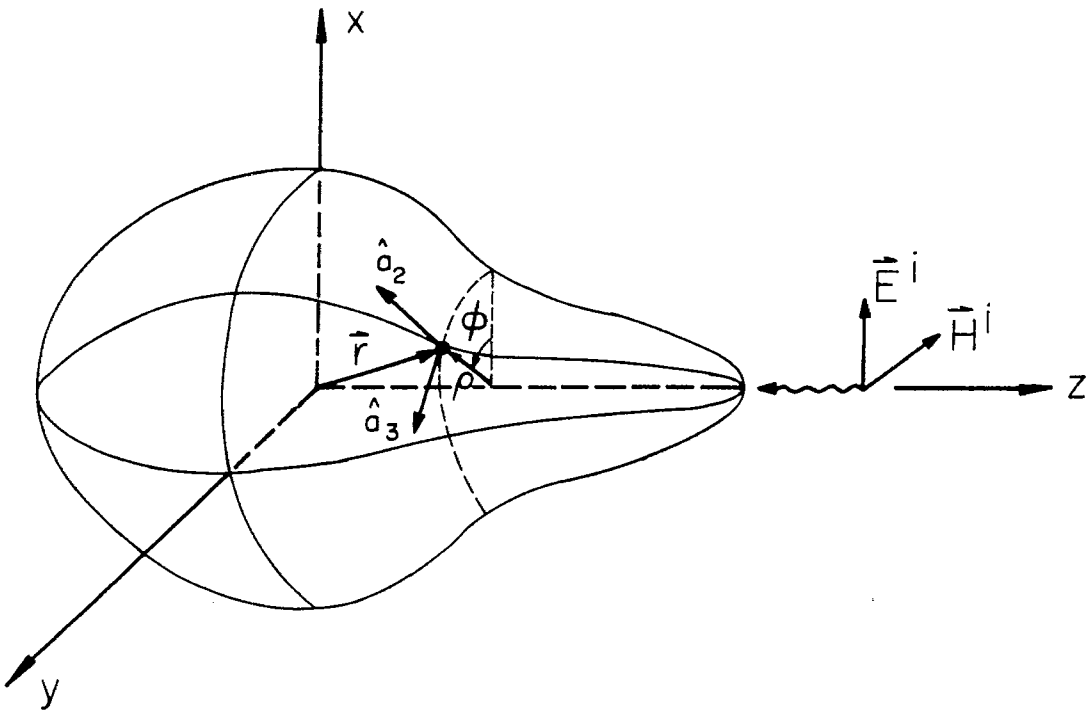

FIG. 57 Geometry of rotationally symmetric scattering problem.

was the program ROTSY, which calculates the surface currents and far-scattered field of a rotationally symmetric object given an incident waveform and a set of parameters describing the geometry of the scattering object. The general flow of the iterative procedure is charted in Fig. 58. The computer program INVER was written to implement this procedure.

An initial estimate of $\rho(z, t)$ is obtained from Eq. (71) by neglecting the surface integral, giving

$$\rho_1(z, t) = \left[2r_o \vec{H}_R^s(\vec{r}, t)\right]^{1/2} .$$

From this estimate, the geometry parameters required by ROTSY are calculated. Because of the integration necessary, a grid on the surface of the scatterer must be defined. To accomplish this the surface is first divided into bands of equal arc length centered on the z axis. Then each band is divided into patches of equal area. In addition to the grid, ROTSY also requires the midpoint z_i of each band, the corresponding $\rho(z_i)$, and the components of the unit normal at $\rho(z_i)$.

These geometry parameters along with a defined incident ramp waveform and the location of the far-field observer are then given as inputs to the ROTSY program. ROTSY uses these inputs to first solve Eq. (65) for the currents on the surface of the scatterer and then from these, it solves Eq. (66) for the far-scattered field. As noted previously, Eq. (65) can be solved solely because the minimum spacing between grid sample points is greater than the time step, which assures that the necessary correction currents have already been computed or are known to be zero. The result is that Eq. (65) is a recurrence relation in time and is solved in ROTSY by incremental steps in the time domain. The time derivatives in Eq. (65) are calculated by using a four-point polynomial interpolation.

The far-field response $r_o\vec{H}_{R1}^s(\vec{r}, t)$ generated by $\rho_1(z, t)$ is then used in Eq. (69) to determine the far-field contribution due to the correction currents, so that

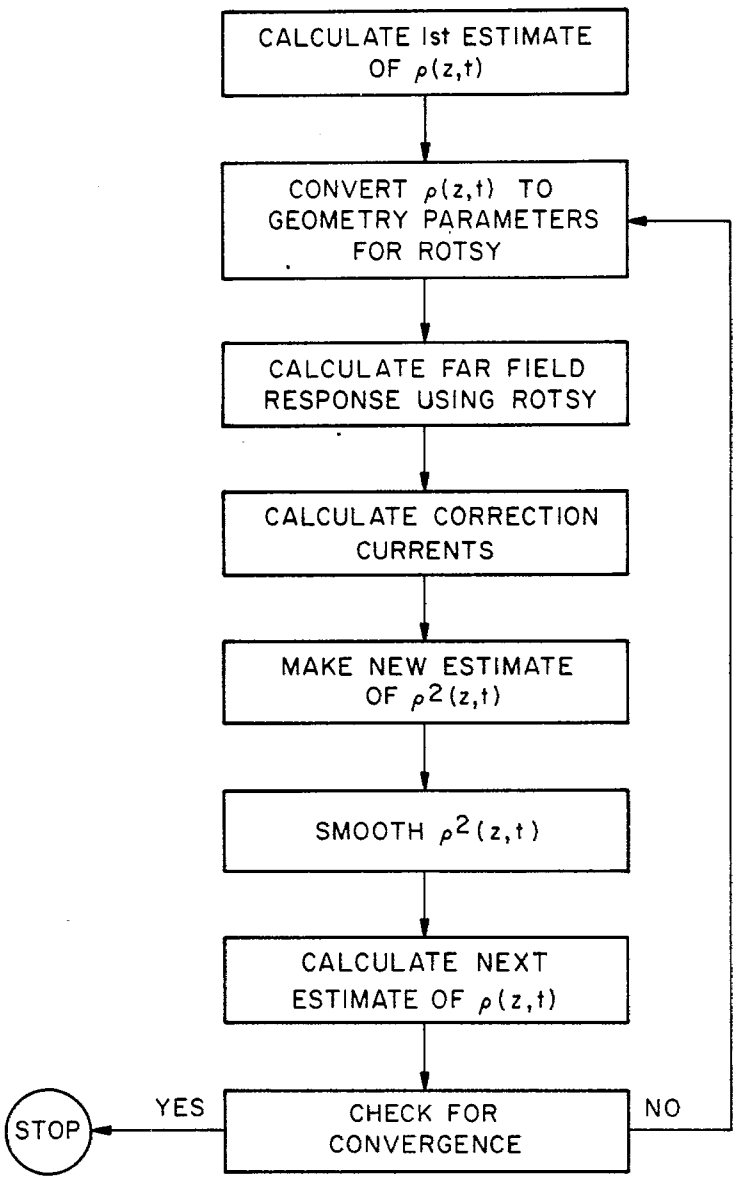

FIG. 58 Iterative procedure used in INVER.

$$\frac{\partial}{\partial t}\int_{\tau = t - R}\left\{\vec{J}_{cR}(\vec{r}', \tau) \times \hat{a}_r\right\} dS' = 4\pi r_o \vec{H}^s_{R1}(\vec{r}, t) - 2\pi\rho_1^2(z, t) \quad .$$

This contribution is then used in Eq. (71) to obtain a new estimate of $\rho^2(z, t)$,

$$\rho_2^2(z, t) = 2r_o\vec{H}^s_R - \frac{1}{2\pi}\frac{\partial}{\partial t}\int_{s_1}\left\{\vec{J}_{cR}(\vec{r}', \tau) \times \hat{a}_r\right\} dS_1' \quad .$$
$$\tau = t - R$$

This new estimate of $\rho^2(z, t)$ is then smoothed using the linear smoothing

$$\rho_n' = \frac{2\rho_{n-1} + 3\rho_n + 3\rho_{n+1}}{8} \quad .$$

It was found that smoothing was necessary because of the coarseness of the integration time step necessary to keep computer run times within reasonable limits. This particular smoothing technique was chosen because it seemed to be effective along horizontal line segments while also taking into account the direction of convergence of the procedure.

From this smoothed $\rho_2^2(z, t)$, the next estimate $\rho_2(z, t)$ is obtained. It is then compared with $\rho_1(z, t)$ to see if the procedure has converged. If it has, the iterative process stops. If not, new geometry parameters are calculated for $\rho_2(z, t)$ and the iterations continue until convergence occurs. The convergence criterion used in INVER demands that the percentage change in $\rho(z, t)$ from one iteration to the next be less than some small number, i.e.,

$$\left|\frac{\rho_{i-1}(z, t) - \rho_i(z, t)}{\rho_{i-1}(z, t)}\right| < \epsilon \qquad \forall \rho(z, t) \quad .$$

The choice of ε is described in the following section.

A computer plot routine was also written to give perspective plots of the estimates of the target contour. All lines hidden from view have been eliminated in the plots. The coordinate axis and the view angle for the plots is shown in Fig. 59.

5.3 RESULTS

The iterative procedure described in the previous section was tested for four rotationally symmetric objects:

(1) A sphere

(2) A cylinder with two sphere caps

(3) A cylinder with a flat front end and a sphere-capped back end, and

(4) A cylinder with a sphere-capped front end and a flat back end.

For all four objects, the radius of the spherical segments was 0.5 meters. The radius of the cylinder body was also 0.5 meters and its length was 1 meter. Figure 60 shows the contours of the four objects tested. In all cases the incident wave was axially incident and the far field was calculated in the backscatter direction. Plots of the ramp responses of the four objects are given in Fig. 61.

For the computer runs made on these objects, the iterative procedure was not terminated at some predesignated point of convergence. Rather, it was decided to allow the procedure to continue in order to study the stability of the solutions. Studies were conducted after the runs were completed to determine the maximum percentage variation (as defined in the previous section) at each step in the iteration. Those results are presented in this section.

The testing of the inversion procedure on these four objects gave, in general, very good results. Two of the objects (1 and 3) converged exactly to the desired solution and remained stable at that point. One of the remaining (object 2) reached the desired target contour but did not remain stable.

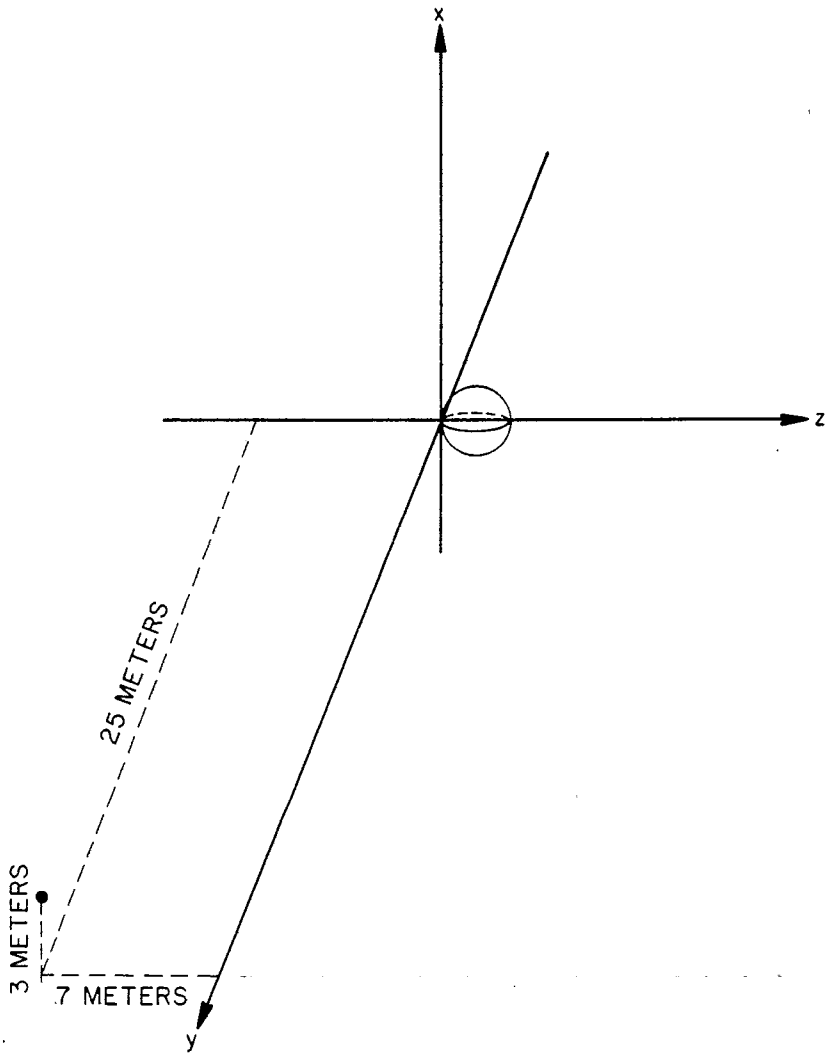

FIG. 59 Coordinate axes and view angle for perspective plots.

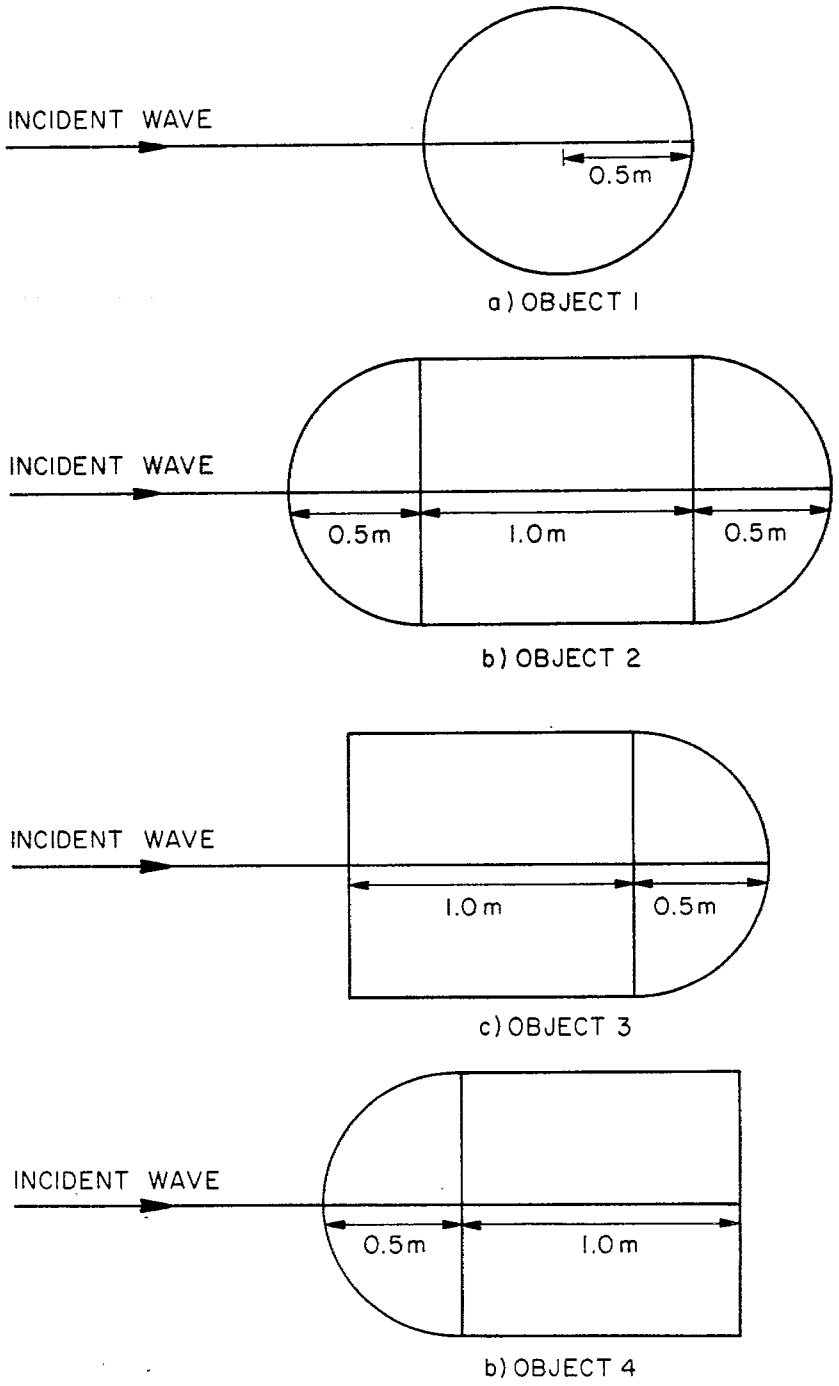

FIG. 60 Geometry of objects used for test of inversion procedure.

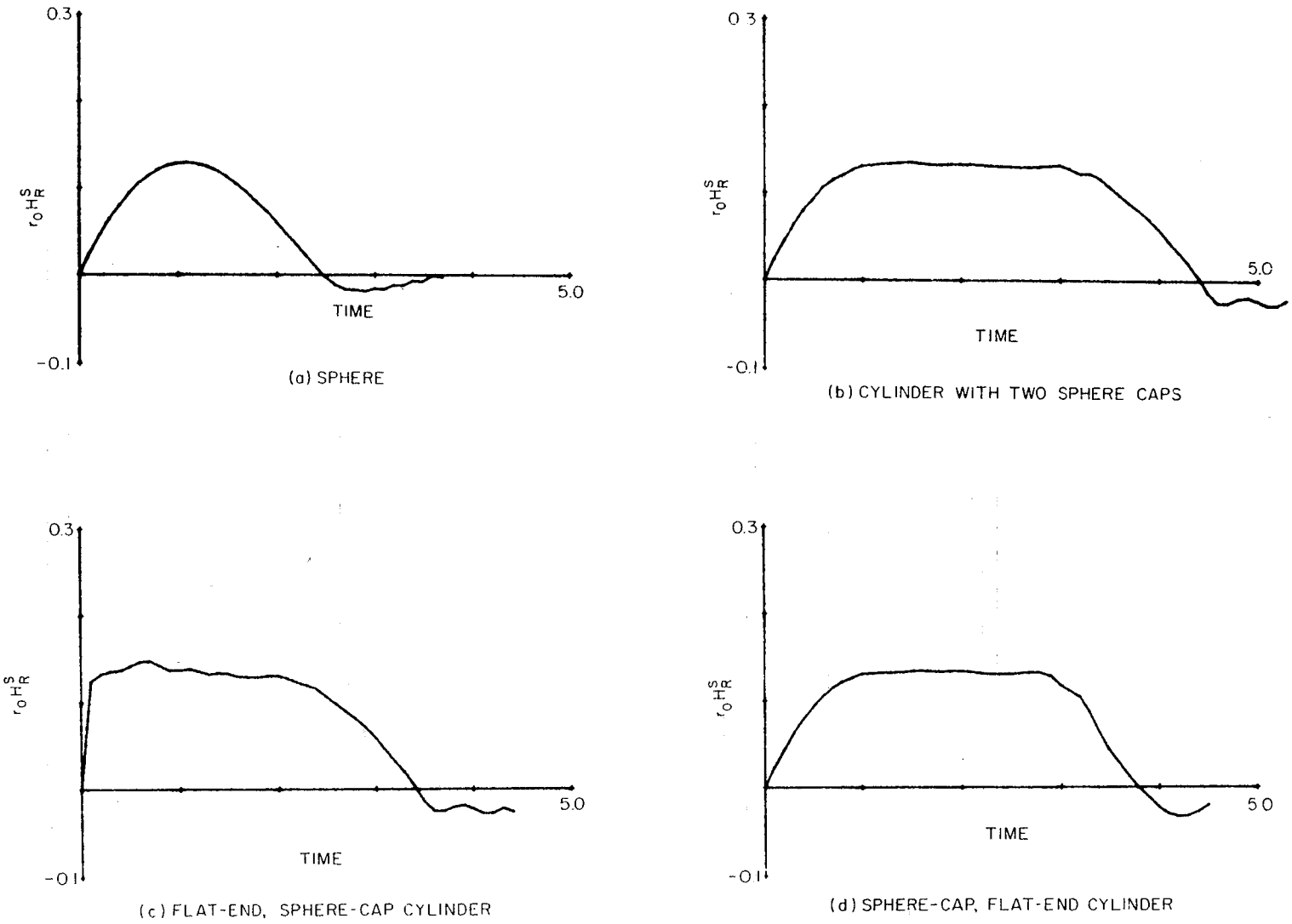

FIG. 61 Far field ramp response (backscatter direction) for four objects tested.

The other (object 4) approaches but never actually reached the desired contour.

5.3.1 Sphere

The results obtained for the sphere, as expected, were the most accurate of all the objects. Figure 62 shows perspective plots of several estimates in the iterative procedure. Graphs of some of the $\rho(z, t)$ contours for the sphere are given in Fig. 63(a).

Note that at iteration 5 the results were in very close agreement with the actual contour. The estimate then began to move past the desired contour. It then corrected for this error by moving back outside the contour and converging in again. The result remained stable at the desired contour after iteration 19. The small error on the front of the sphere was a result of the weights used in the smoothing technique, which tended to smooth those $\rho(z, t)$ values upward.

The convergence criterion worked very well for determining the convergence of the sphere. The maximum percentage variation at iteration 20 was less than 10% and by iteration 31 it had decreased to .04%.

5.3.2 Cylinder With Two Sphere Caps

The cylinder with two sphere caps gave fairly accurate results, although not as good as for objects 1 and 3. Figure 64 shows perspective plots of the iteration estimates for this target; two dimensional contour plots are given in Fig. 63(b).

The estimates were in close agreement with the actual contour along the front sphere cap and the cylinder body. The estimates moved in at both iterations 10 and 25 to closely approximate the back sphere cap. They did not, however, remain stable at that point. At iterations 11 and 26 the estimates moved back outside the desired contour and began to converge in again. It is possible that if the procedure were allowed to continue through more iterations a stable result could be achieved. This did not, however, appear to be the case in the 30 iterations performed.

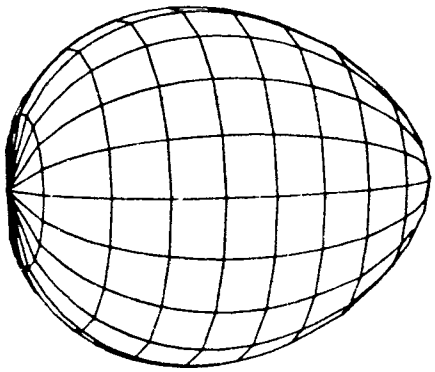

ESTIMATE 1

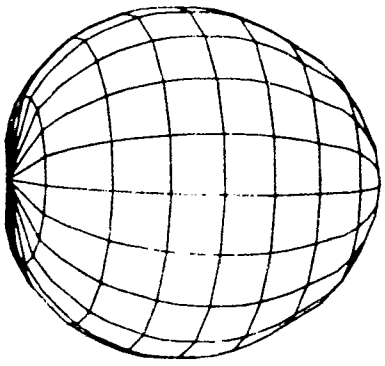

ESTIMATE 2

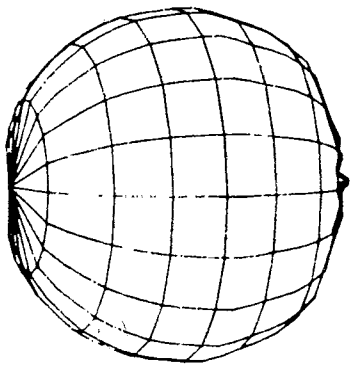

ESTIMATE 9

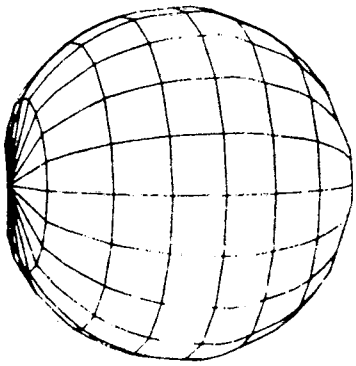

ESTIMATE 19

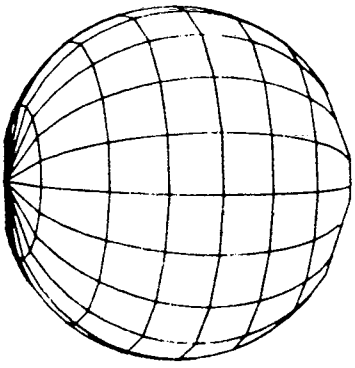

ACTUAL CONTOUR

FIG. 62 Perspective plots of contour estimates for a sphere.

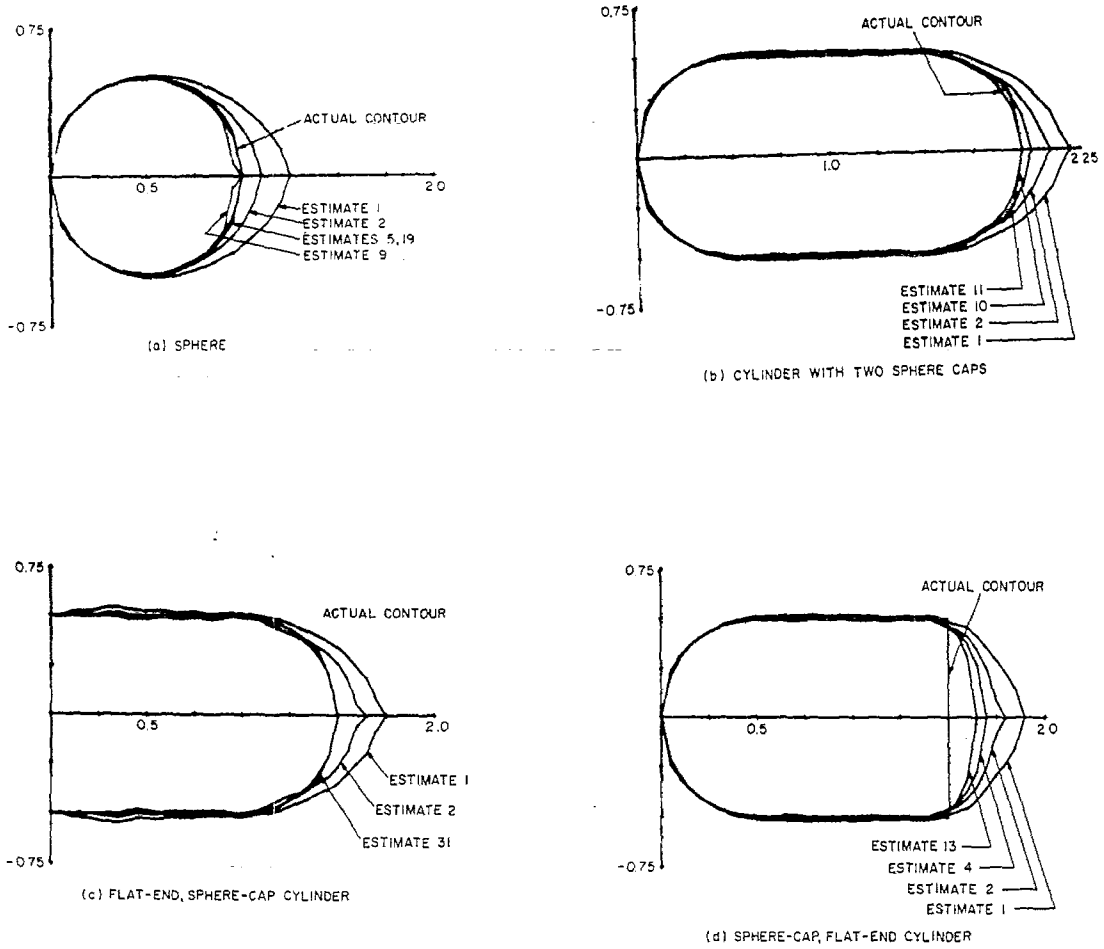

FIG. 63 Contour estimates for four objects tested.

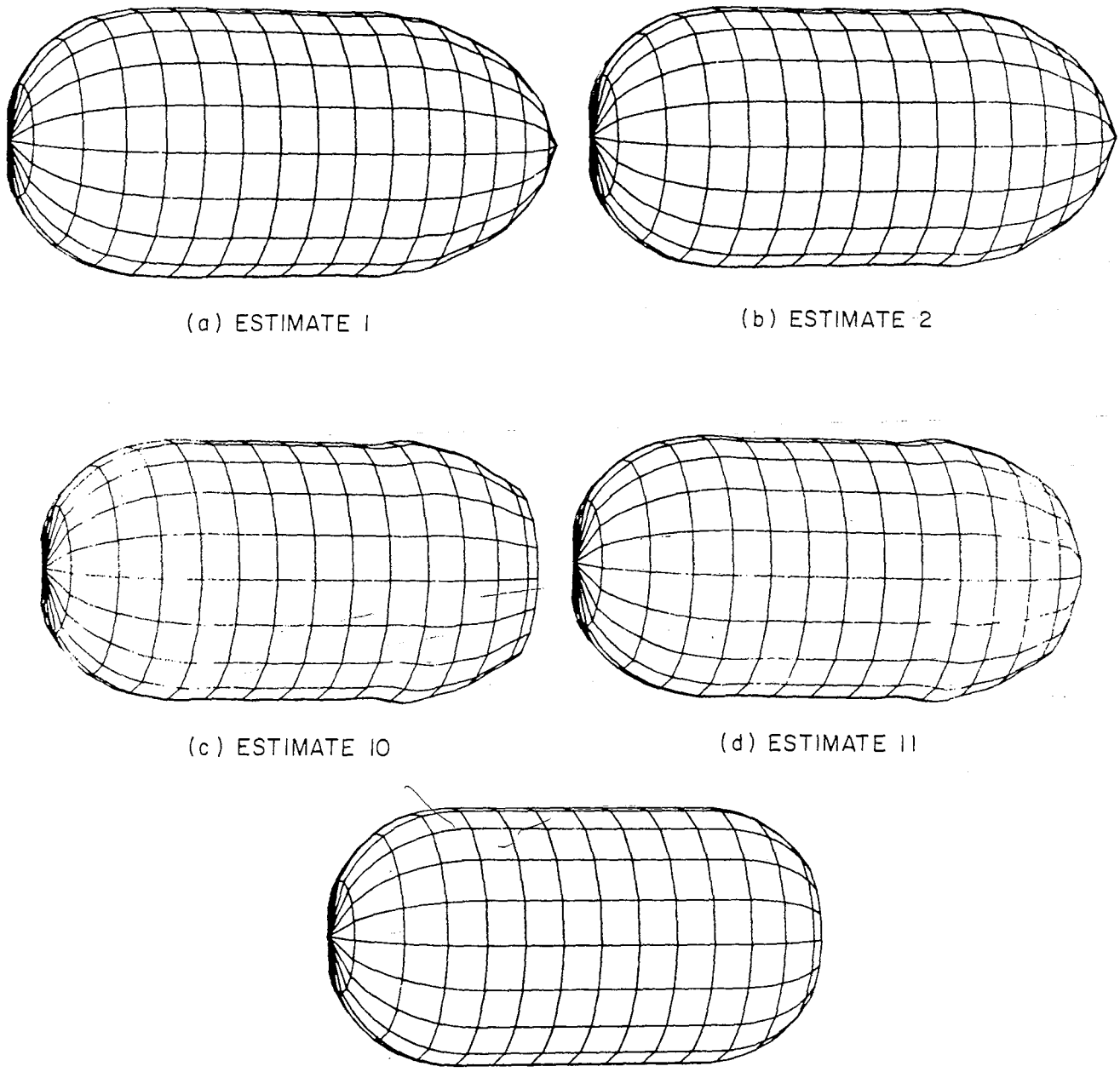

FIG. 64 Perspective plots of contour estimates for a cylinder with two sphere caps.

The convergence criterion did not indicate convergence for this figure. There were periods of relatively small variation as the estimates became close to the desired contour. The instability of the results, however, caused the variation to increase dramatically once the actual contour was reached.

5.3.3 Flat-End Sphere-Cap Cylinder

The results for this object were also very good. It converged to the desired contour and remained stable at that point. Perspective plots of the contour estimates are given in Fig. 65; the two-dimensional contour is shown in Fig. 63(c).

The flat-end, sphere-cap (FE-SC) cylinder converged directly to its desired solution. There was some slight oscillation along the cylinder body, but the agreement in general, was good. At iteration 20, the estimate first reached the general desired contour. It then continued to smooth out the errors along the contour. These successive iterations point out one characteristic of this procedure — errors above and below the contour tend to cancel each other. This tends to lead to a more stable solution.

It should be pointed out that for the FE-SC cylinder it was determined from the initial $\rho(z, t)$ estimate that the front end of this object was flat. At that time geometry parameters for ROTSY were determined for the front, and these parameters were held constant over the rest of the iterations.

For the FE-SC cylinder the convergence criterion was not as effective in determining convergence as for the sphere. There were some periods of very small variation during the conversion process that were comparable to the variation found after convergence had occurred. A criterion requiring the maximum percentage variation to be less than ϵ for some number of iterations would have been a more effective convergence criterion for this object.

5.3.4 Sphere-Cap Flat-End Cylinder

The results for the sphere-cap flat-end (SC-FE) cylinder were not as accurate as for the other figures. This was expected, however, because of the

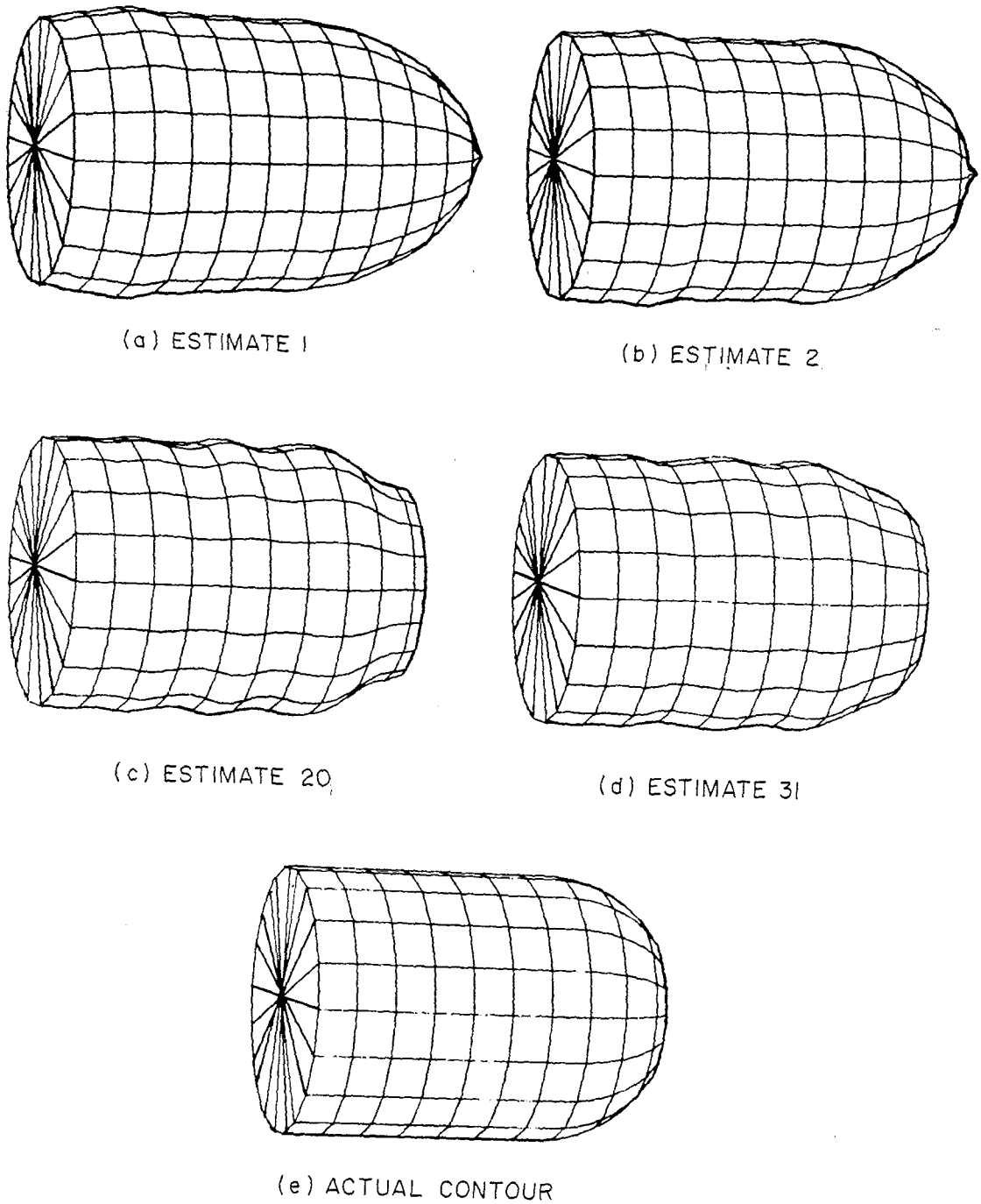

FIG. 65 Perspective plots of contour estimates for a flat-end sphere-cap cylinder.

problem of getting the tail of the SC-FE ramp response to converge to a vertical line. However, the results, shown in perspective in Fig. 66 and in contour in Fig. 63(d), were fairly close to the actual contour.

As with object 2, the estimates were in very close agreement with the actual contour along the sphere cap and cylinder body. There was the same slight oscillation along the cylinder body found in objects 2 and 3. The estimates for the flat back moved in to within 0.3 meters of the desired result but never reached the vertical drop required.

The convergence criterion did not indicate convergence for this figure. There were, however, periods of slow variation during the convergence process that would indicate that some modified criterion such as that discussed in Sec. 5.3.3 would be a more effective measure of convergence.

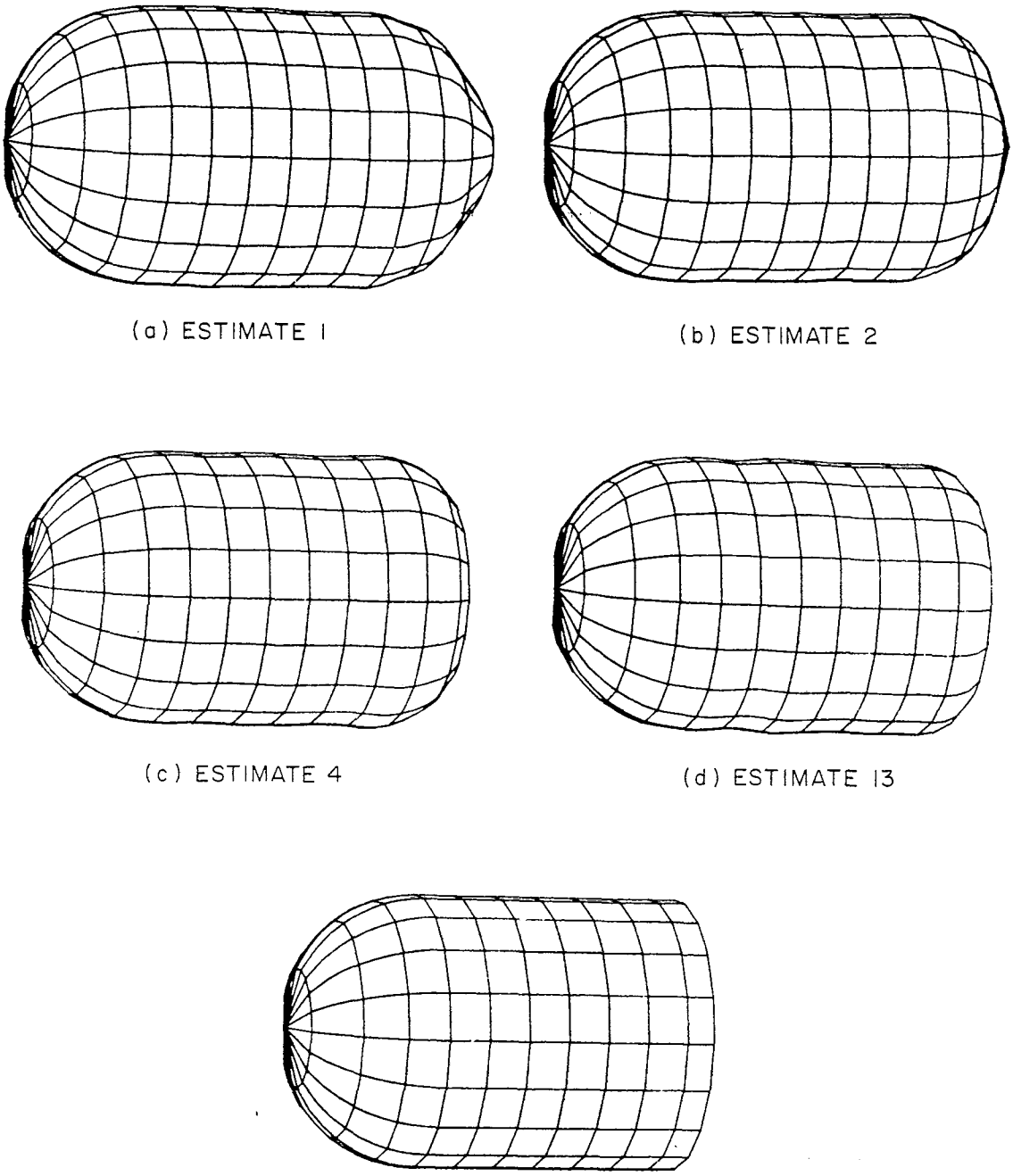

FIG. 66 Perspective plots of contour estimates for a sphere-cap flat-end cylinder.

SECTION 6
CONCLUSIONS

In this study the technique for computing the impulse response of smooth convex targets has been extended to bodies which have edges and to open thin surfaces. The foundation of this technique is the space-time integral equation approach to the solution of the electromagnetic scattering problem. This coupled with the impulse response augmentation technique, is used to yield the total impulse response or the frequency response over the entire spectrum for a target. This, in turn, can be used to compute the response of a target due to any incident radar waveform, regardless of waveshape or carrier frequency.

New numerical procedures for solution of the space-time integral equation were developed for computing the smoothed impulse response of targets with edges. These procedures allow a variable space patch size, while at the same time removing the restriction that the time increment must be less than the minimum distance between space sample points. This permits the use of small patch size in the neighborhood of edges, where the spatial variation of the surface current can be most rapid, and normal patch size over the smooth convex regions of the surfaces. The net result is a more accurate, more efficient (in terms of computer running time and memory requirements) solution procedure. Using the resulting improved smoothed impulse response computations, the impulse response augmentation technique was applied to obtain the total impulse response of two targets with edges. The modifications required on the augmentation technique in order to make it applicable to targets with edges was minimal. It was necessary to only change the parts of the augmentation function and the high frequency estimate which are used to account for surface discontinuities. Results were obtained for a flat-end sphere-cap cylinder at both directions of axial incidence and for a right circular cylinder at axial incidence. The results obtained using this technique continue to be encouraging and should be extended to off-axis incidence of these targets and to more complicated targets.

Direct time domain smoothed impulse response measurements were made on seven open thin surface geometries at a total of 47 target aspect angles. The processing of the measurements was improved in this work to give lower noise and to cast them into a form more suitable for direct comparison with computations. The results obtained were used for verifying the present numerical computations and could be used to verify future computations. In addition, these measured results provide insight into the scattering mechanism and once again prove their value.

The space-time integral equation approach was extended in this effort to the solution of the open thin surface scattering problem. The E-field boundary condition was used to develop a space-time integrodifferential equation for this scattering problem which had many similarities to the solution of the thin wire problem. Numerical techniques were developed for solving this integrodifferential equation for flat surfaces with rectangular contours and for flat surfaces with circular contours. In addition, numerical techniques were developed for treating concave rectangular surfaces. The technique was demonstrated on a flat square plate, a flat circular plate, and a parabolic cylinder section and the results were in good agreement with direct time domain scattering range measurements. These results are particularly encouraging and should be extended to additional target geometries.

A new approach to the inverse scattering problem was developed and demonstrated in this study. This approach starts with a space-time integral equation that represents the inversion process. An iterative technique was developed for the solution of the inversion equation and applied for four target geometry cases. Results were obtained for a sphere, a sphere-cap cylinder, and a flat-end sphere-cap cylinder, all with axial incidence. The iterative solution technique yielded convergence in most cases and provided results in the form of contour plots that agree closely with the actual target geometries used. Three-dimensional plots of the target surfaces were also displayed at various steps of the iteration process. The results of this work provide a sound foundation on which a viable time domain approach to the inverse scattering problem can be built. The results obtained in this initial effort should merit further effort.

SECTION 7

REFERENCES

1. C. L. Bennett, W. L. Weeks, "A Technique for Computing Approximate Electromagnetic Impulse Response of Conducting Bodies," Interaction Note 222, June 1968.

2. A. W. Maue, "Zur Formulierung Lines Allgemeinen Beugungs: Problems Durch Line Integralgleichung," Zeitschrift fur Physik, Bd 126, S.601-618 (1949).

3. C. L. Bennett, A. M. Auckenthaler, R. S. Smith, J. D. DeLorenzo, "Space-Time Integral Equation Approach to the Large Body Scattering Problem," Sperry Research Center, Sudbury, Mass., Final Report on Contract No. F30602-71-C-0162, January 1973, RADC-TR-73-70, AD763 794.

4. C. L. Bennett, J. D. DeLorenzo and A. M. Auckenthaler, "Integral Equation Approach to Wideband Inverse Scattering," Sperry Rand Research Center, Sudbury, Mass., Final Report on Contract No. F30602-69-C-0332, June 1970, RADC-70-177, I - AD876 849 II - AD876 627

5. A. M. Nicolson et al, "Applications of Time Domain Metrology to the Automation of Broadband Microwave Measurements," IEEE Trans. Microwave Theory and Techniques MTT-20, 3-9 (January 1972).

6. Armen H. Zenanian, Distribution Theory and Transform Analysis (McGraw-Hill, New York, 1965).

7. R. S. Smith, J. D. DeLorenzo and C. L. Bennett, "Wideband Surface Current Analysis," Sperry Rand Research Center, Sudbury, Mass., Final Report on Contract No. F30602-69-C-0357, July 1970, RADC-TR-70-188, AD512 772.

8. D. S. Jones, The Theory of Electromagnetism (Pergamon Press, McMillan Co., 1964).

9. R. W. P. King, Fundamental Electromagnetic Theory (Dover Publications, Inc., 1963), pp. 167-8.

10. E. M. Kennaugh and R. L. Cosgriff, "The Use of Impulse Response in Electromagnetic Scattering Problems," 1958 IRE National Convention Record, Part 1, pp. 72-77.

11. N. N. Bojarski, "Three-Dimensional Electromagnetic Short Pulse Inverse Scattering," Syracuse University Res. Corp., Syracuse, New York, February 1967.

12. R. M. Lewis, "Physical Optics Inverse Diffraction," IEEE Trans. Antennas and Propagation AP-17, No. 3, May 1969.

SECTION 8

APPENDICES

8.1 DERIVATION OF THE PROPORTIONALITY CONSTANT BETWEEN $\vec{J}$ AND $\vec{A}'$

Starting with $\vec{A}'(r, t)$ as defined in Eq. (43):

$$\vec{A}'(\vec{r}, t) = \frac{1}{4\pi} \int_{S'_{\vec{r}}} \frac{\vec{J}\left(\vec{r}, t - \frac{|\vec{r} - \vec{r}'|}{c}\right)}{|\vec{r} - \vec{r}'|} dS'$$

$$= \frac{\vec{J}(\vec{r}, t)}{4\pi} \int_{S'_{\vec{r}}} \frac{1}{|\vec{r} - \vec{r}'|} dS'$$

provided that $\vec{J}$ can be assumed constant over patch area $S'_{\vec{r}}$ and equal to the value of $\vec{J}$ at the center $\vec{r}' = \vec{r}$ of the patch. Placing coordinates at the patch center, as in Fig. 67, so that $\vec{r} \Leftrightarrow (0, 0)$ and $\vec{r}' \Leftrightarrow (x, y)$ and integrating over the 2γ by 2δ rectangle gives

$$\vec{A}'(\vec{r}, t) = \frac{\vec{J}(\vec{r}, t)}{4\pi} \int_{-\gamma}^{+\gamma} \int_{-\delta}^{+\delta} \frac{1}{\sqrt{x^2 + y^2}} dy\, dx \quad .$$

The double integral alone is equivalent to

$$I(\gamma, \delta) = 4 \int_0^{\gamma} \int_0^{\gamma} \frac{1}{\sqrt{x^2 + y^2}} dy\, dx = 4 \int_0^{\gamma} \left[\ell n \left(\frac{\delta}{x} + \sqrt{1 + \left(\frac{\delta}{x}\right)^2} \right) \right] dx$$

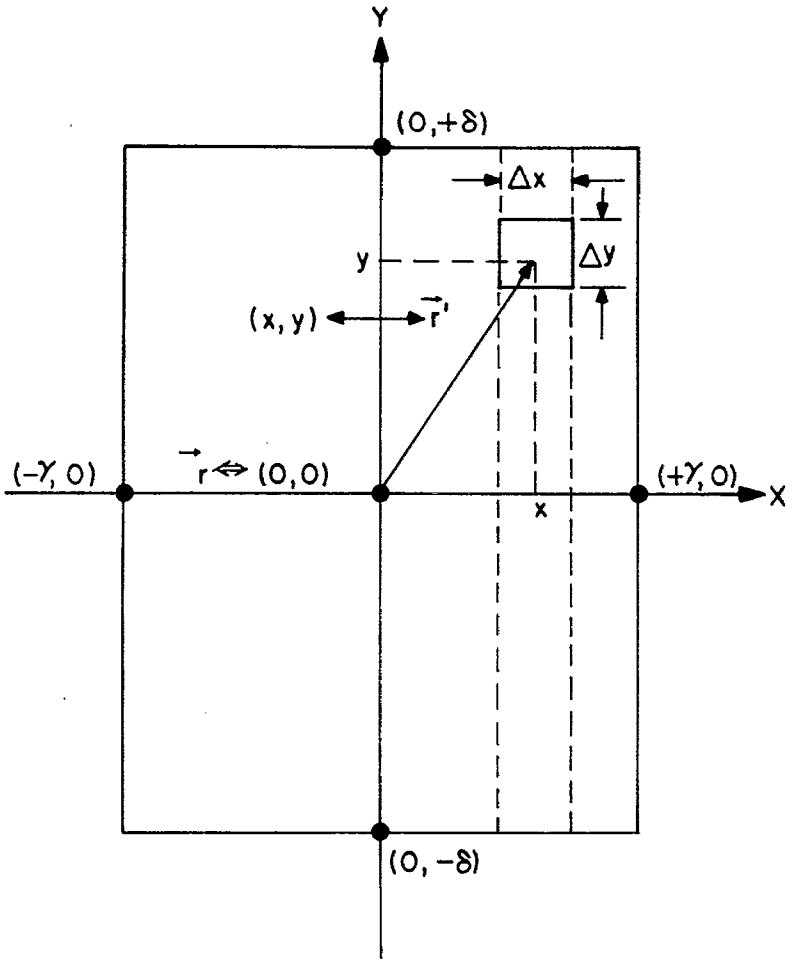

FIG. 67 A rectangular patch with sides 2γ and 2δ for which local coordinates, originating at the patch center, have been constructed.

and under the area-preserving transformation $x \to \frac{\delta}{\xi}$, $dx \to -\frac{\delta}{\xi^2}\, d\xi$:

$$I(\gamma, \delta) = 4\left\{\gamma \ell n\left[\frac{\delta}{\gamma} + \sqrt{1+\left(\frac{\delta}{\gamma}\right)^2}\right] + \delta \ell n\left[\frac{\gamma}{\delta} + \sqrt{1+\left(\frac{\gamma}{\delta}\right)^2}\right]\right\}.$$

In particular, $I\left(\frac{\Delta s}{2}, \frac{\Delta s}{2}\right) = 4\Delta s \cdot \ell n(1+\sqrt{2})$, so that for a square patch Δs on a side, $\vec{A}'(\vec{r}, t) = \frac{\vec{J}(\vec{r}, t)}{4\pi} \cdot 4\Delta s\, \ell n(1+\sqrt{2})$ from which immediately:

$$\vec{J}(\vec{r}, t) = \frac{\pi}{\Delta s \cdot \ell n(1+\sqrt{2})}\, \vec{A}'(\vec{r}, t) .$$

8.2 ITERATIVE NUMERICAL PROCEDURE FOR COMPUTING $y = h^*(u)$ WHEN g DEFINES A PARABOLA

Given a parabola consisting of points $(y, z) = (y, Gy^2)$, where $G > 0$ is given and fixed, for a specific point (Y, GY^2) on the parabola. Y can be computed given only the arc-length U along the parabola $(0, 0)$ to (Y, GY^2) . The reverse problem of finding U from Y is not in fact a problem because $U = h(Y)$ can be computed explicitly from the formula in Eq. (59) for h ; this formula is repeated below under Step 2.

For the parabolic case under consideration, the number $Y = h^*(U)$ can be approximated to any required accuracy by repeated applications of the three-step algorithm below. Here, again, h^* is the inverse of function h ; that is, $h\left(h^*(u)\right) = u$ for all real u . Thus the algorithm approximates $h^*(U)$ with $h^*_\epsilon(U)$ where ϵ is the specified relative error in $0 \le \frac{h\left(h^*_\epsilon(U)\right) - U}{U} < \epsilon$.

Only a slight modification in the algorithm to be described and proven is required in order to compute $h^*(u)$ for all negative u as well. In the steps below, $i = 1, 2, 3, \ldots$ refers to the number of the iteration.

Step 1: For the first iteration $(i = 1)$, take $y_i = U$.

Step 2: With a value for y_i in hand, compute

$$h(y_i) = \frac{y_i}{2}\sqrt{1 + (2Gy_i)^2} + \frac{1}{4G}\ell n\left(2Gy_i + \sqrt{1 + (2Gy_i)^2}\right)$$

Step 3(a): If $\dfrac{h(y_i) - U}{U} \geq \epsilon$

then take $$y_{i+1} = y_i - \frac{h(y_i) - U}{\sqrt{1 + (2Gy_i)^2}}$$

and return to Step 2, using the value of y_{i+1} in place of y_i.

Step 3(b): If $\dfrac{h(y_i) - U}{U} < \epsilon$

then the present value of y_i is acceptably close to Y and

$$Y = h^*(U) \approx h^*_\epsilon(U) = y_i .$$

What follows is a proof that the numbers $y_1, y_2, y_3, y_4 \cdots$ with $y_1 = U$ and the others generated in accordance with Step 3(a) above are all positive and comprise a monotonically decreasing sequence whose greatest lower bound is $Y = h^*(U)$.

To begin, observe that h and therefore also h^* are *monotonically* increasing functions. Indeed, for h the derivative function h' given by

$$h'(y) = \sqrt{1 + (2Gy)^2} \quad \text{for all } y$$

is also a monotonically increasing function over the range $0 \leq y < \infty$, which is also the range of concern in this proof. A convenient way to express this

"strong" monotonicity of h is: If α and β are any two numbers satisfying $0 \le \alpha < \beta$, then

$$h'(\alpha) < \frac{h(\beta) - h(\alpha)}{\beta - \alpha} < h'(\beta) \quad .$$

Here, $\frac{h(\beta) - h(\alpha)}{\beta - \alpha}$ is the slope of the chord joining points $\big(\alpha, h(\alpha)\big)$ and $\big(\beta, h(\beta)\big)$. This slope can appear in the above inequality as it does because the Mean Value Theorem assures the existence of a third number γ in the range $\alpha < \gamma < \beta$ for which $h'(\gamma) = \frac{h(\beta) - h(\alpha)}{\beta - \alpha}$. The above inequality then follows, recalling that $h'(\alpha) < h'(\gamma) < h'(\beta)$ must hold.

In addition to the "strong" monotonicity of h, the following lemma will also be useful.

Lemma: Given two numbers s_1 and s_2 satisfying $0 < s_1 < s_2 < \infty$ and any number V, consider the horizontal line consisting of points (w, V) in the wv-plane as in Fig. 68. Figure 68 also shows a second line consisting of the points $(w, v) = \big(w, V + s_1(w - W)\big)$, where the point (W, V) is their intersection. In that same figure, $W < w_1$ and the sequence of numbers w_1, w_2, w_3, ... satisfies the condition

$$w_{i+1} = \left(1 - \frac{s_1}{s_2}\right) w_i + \frac{s_1}{s_2} W$$

for every $i = 1, 2, 3 \ldots$ The claim is that $\lim_{i \to \infty} w_i = W$. This may be apparent from the figure, but a more rigorous substantiation follows.

Recursive application of the above formula gives:

$$w_2 = \left(1 - \frac{s_1}{s_2}\right) w_1 + \frac{s_1}{s_2} W$$

$$w_3 = \left(1 - \frac{s_1}{s_2}\right)^2 w_1 + \left[\left(1 - \frac{s_1}{s_2}\right) + 1\right] \left(\frac{s_1}{s_2}\right) W$$

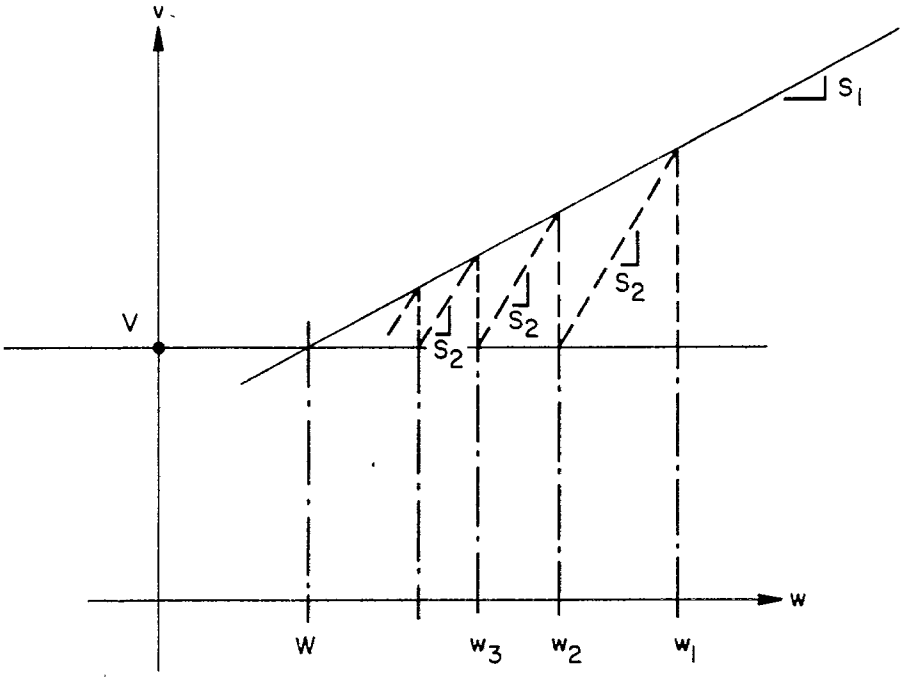

FIG. 68 Geometrical figure for the Lemma.

$$w_4 = \left(1 - \frac{s_1}{s_2}\right)^3 w_1 + \left[\left(1 - \frac{s_1}{s_2}\right)^2 + \left(1 - \frac{s_1}{s_2}\right) + 1\right] \left(\frac{s_1}{s_2}\right) W$$

$$\vdots$$

$$w_n = \left(1 - \frac{s_1}{s_2}\right)^{n-1} w_1 + \left[1 - \left(1 - \frac{s_1}{s_2}\right)^{n-2}\right] W$$

The initial assumptions concerning slopes s_1 and s_2 imply $0 < 1 - \frac{s_1}{s_2} < 1$, so that together with this last line

$$\lim_{n \to \infty} w_n = 0 \cdot w_1 + [1 - 0] W = W$$

and the lemma is proven.

Parameters in the above lemma can be identified with those in the algorithm. Observe first that $Y < U$, since after setting $\alpha = 0$ in the statement of "strong" monotonicity for h, the first half of the inequality reduces to $1 < \frac{h(\beta)}{\beta}$ for all $\beta > 0$. This, together with the ordinary monotonicity of h^*, implies $h^*(\beta) < h^*\big(h(\beta)\big) = \beta$, so that in particular $h^*(U) < U$, and finally $h^*(U) = Y < U$. It follows that $h'(Y) < h'(U)$ so that the identifications $s_1 = h'(Y)$ and $s_2 = h'(U)$ are legitimate. Letting $W = Y$, the lemma then specializes to

$$\lim_{i \to \infty} w_i = Y ,$$

provided that $w_1 = U$ and

$$w_{i+1} = \left(1 - \frac{h'(Y)}{h'(U)}\right) w_i + \frac{h'(Y)}{h'(U)} W .$$

It remains only to prove that for all $i \geq 2$ it is true that $Y < y_i < w_i$. As the basis of an inductive argument that this is indeed so, let $\alpha = Y$ and $\beta = U$ in the "strong" monotonicity statement. The second inequality there

now specializes to $\frac{h(U) - h(Y)}{U - Y} < h'(U)$, so that

$$y_2 = y_1 - \frac{h(y_1) - U}{h'(y_1)} = u - \frac{h(U) - U}{h'(U)} > U - \frac{h(U) - h(Y)}{\left(\frac{h(U) - h(Y)}{U - Y}\right)} = Y \quad .$$

Moreover, the first inequality specializes to $h'(Y) < \frac{h(U) - h(Y)}{U - Y}$; that is, $h(U) - h(Y) > h'(Y) \cdot (U - Y)$. Hence $y_2 = U - \frac{h(U) - U}{h'(U)} < U - \frac{h'(Y)(U-Y)}{h'(U)} = w_2$. Thus the basis $Y < y_2 < w_2$ is established.

For the inductive step, $Y < y_{i+1} < w_{i+1}$ is proven to follow from the assumption that $Y < y_i < w_i$. Step 3(a) is equivalent to $h'(y_i) = \frac{h(y_i)-h(Y)}{y_i - y_{i+1}}$, which with $\alpha = Y$ and $\beta = y_i$ in the second inequality of the "strong" monotonicity statement becomes

$$\frac{h(y_i) - h(Y)}{y_i - Y} < h'(y_i) = \frac{h(y_i) - Y}{y_i - y_{i+1}} \quad .$$

From the first and third terms here, $1/(y_i - Y) < 1/(y_i - y_{i+1})$ and $Y < y_{i+1}$ is established.

Finally, using $\alpha = Y$ and $\beta = y_i$, $h'(Y) < \frac{h(y_i) - h(Y)}{y_i - Y}$, then $h(y_i) - U > h'(Y)(y_i - Y)$. And since $w_i > y_i$, it follows immediately that $h(w_i) - U > h'(Y)\ (y_i - Y)$. Thus, starting with Step 3(a) and concluding with the recursive formula for w_{i+1} ,

$$y_{i+1} = y_i - \frac{h(y_i) - U}{h'(y_i)} < y_i - \frac{h'(Y)(y_i - Y)}{h'(y_i)} < w_i - \frac{h'(Y)(w_i - Y)}{h'(U)} = w_{i+1} \quad .$$

With the inductive step thus completed, it follows immediately that $Y \leq \lim_{i \to \infty} y_i \leq \lim_{i \to \infty} w_i = Y$. This then completes the proof that for any

$$U > 0 \quad \lim_{\epsilon \to 0} h^*_\epsilon(U) = h^*(U) = Y \quad .$$

8.3 THE VANISHING OF $\frac{\partial A_p}{\partial p}$ EVERYWHERE ON SCATTERING SURFACE S'

The boundary condition $\vec{A}_1 = \vec{A}_2$ everywhere at the interface between media 1 and 2 can be imposed because it is not inconsistent with Eq. (30).[9] The thin-surface scattering problem presents a three-media situation where free-space media 1 and 3 sandwich a conducting medium 2. Thus, $\vec{A}_1 = \vec{A}_2$ everywhere at one interface and $\vec{A}_2 = \vec{A}_3$ everywhere at the other. For a point $\big(x, y, g(y)\big)$ on the surface S' of medium 2 together with two points (x', y', z') and (x'', y'', z'') in media 1 and 3 respectively, each a distance ϵ from and on the normal line to S' passing through the point $\big(x, y, g(y)\big)$, one obtains

$$\vec{A}(x', y', z') \approx \vec{A}\big(x, y, g(y)\big)$$

and

$$A(x'', y'', z'') \approx \vec{A}\big(x, y, g(y)\big) \quad .$$

The error of these approximations approaches zero as $\epsilon \to 0$. Thus

$$A_p(x', y', z') \approx A_p(x'', y'', z'')$$

and since the two-sided space derivative at $\big(x, y, g(y)\big)$ can be approximated by

$$\frac{\partial A_p}{\partial p}(x, y, z) \approx \frac{A_p(x', y', z') - A_p(x'', y'', z'')}{2\epsilon}$$

the imposition of $\frac{\partial A_p'}{\partial p} + \frac{\partial A_p''}{\partial p} = 0$ everywhere on S' and for all time is not inconsistent with Eq. (30).

8.4 PSEUDOFUNCTIONS

$-\frac{1}{2}t^{-3/2}\,U(t)$ is a pseudofunction which is defined as the derivative (in the distributional sense) of the distribution $t^{-\frac{1}{2}}U(t)$. As long as derivatives are taken in the distributional sense, the effect of this distribution can be found. For example, consider its convolution with $e(t)$:

$$r(t) = e(t) * \left[-\tfrac{1}{2}t^{-3/2}\,U(t) \right] .$$

We know from distribution theory that this convolution can also be written in the form

$$r(t) = e'(t) * \left(t^{-\frac{1}{2}}U(t) \right)$$

where $e'(t)$ is the derivative of $e(t)$. This particular form can now be written as an integral provided $e'(t)$ is bounded and absolutely integrable,

$$r(t) = \int_{\epsilon}^{\infty} e'(t-\tau)\,\tau^{-\frac{1}{2}}\,d\tau .$$

This equation may be written as the following limit:

$$r(t) = \lim_{\epsilon \to 0} \int_{\epsilon}^{\infty} e'(t-\tau)\,\tau^{-\frac{1}{2}}\,d\tau .$$

Performing an integration by parts, the result is

$$r(t) = \lim_{\epsilon \to 0} \left[e(t-\epsilon)\epsilon^{-\frac{1}{2}} - \int_{\epsilon}^{\infty} \tfrac{1}{2}\tau^{-3/2} e(t-\tau) \right] d\tau .$$

Re-writing the equation yields

$$r(t) = \lim_{\epsilon \to 0} \int_{\epsilon}^{\infty} -\tfrac{1}{2}\, \tau^{-3/2}\left[e(t-\tau) - e(t-\epsilon)\right] dt \quad .$$

The limit can now be taken as

$$r(t) = \int_{0}^{\infty} -\tfrac{1}{2}\, (t-\tau)^{-3/2}\left[e(t-\tau) - e(t)\right] d\tau \quad .$$

This is the correct result provided $e'(t)$ is bounded and absolutely integrable. This technique may be applied to other pseudofunctions in the form $t^{\alpha} U_{-1}(t)$, provided α is not an integer. The technique may require taking more than one derivative.

The convolution can also be written in the equivalent form

$$r(t) = \int_{0}^{\infty} -\tfrac{1}{2}\, (t-\tau)^{-3/2}\left[e(\tau) - e(t)\right] d\tau \quad .$$

8.5 CONVOLUTION OF DISTRIBUTIONS

In general, the convolution of two distributions, $f * g$, does not exist. Under certain restrictions the convolution can be defined. The most common conditions are as follows:

(1) Either f or g has bounded support

(2) Both f and g have supports bounded on the left [i.e., there exists some constant T_1 such that $f(t) = g(t) = 0$ for $t < T_1$].

(3) Both f and g have supports bounded on the right [i.e., there exists some constant T_2 such that $f(t) = g(t) = 0$ for $t > T_2$]

(4) f is a temporal distribution and g is an infinitely smooth function of rapid descent.